Topology optimization for metal additive manufacturing considering manufacturability

Takao Miki

2023

Acknowledgements

I would like to express my deepest gratitude to all those who have supported me throughout the completion of my doctoral degree. Their contributions have been invaluable, and I am truly grateful for their assistance and guidance.

First and foremost, I would like to extend my heartfelt appreciation to my supervisors, Professor Shinji Nishiwaki, Professor Kazuhiro Izui, and Professor Takayuki Yamada. Their expertise, dedication, and unwavering support have been instrumental in shaping this research. I am deeply grateful for their mentorship and insightful feedback that have greatly enriched the quality of my work.

I am also deeply grateful to Professor Atsushi Matsubara in the Department of Micro Engineering at Kyoto University, and Professor Tomoko Hirayama in the Department of Mechanical Engineering and Science, also at Kyoto University, for their thoughtful advice and for serving on my dissertation committee.

My sincere appreciation extends to all the individuals at Osaka Research Institute of Industrial Science and Technology for their warm support in carrying out this research. Especially, I would like to thank Dr. Hisashi Minami for giving me the opportunity to enter the doctoral program. I would also like to express my gratitude to the members in th research division of Machining & Molding who encouraged me throughout my research activities. Their kindness and encouragement allowed me to undertake challenging research in an important academic field.

I would also like to thank Dr. Kozo Furuta for his help and advice on a variety of matters, both public and private. I am indebted also to Mr. Steve Wever for his invaluable help in editing my papers in English.

Last but not least, I want to express my heartfelt gratitude to my family. Their unwavering belief in me, constant encouragement, and understanding have been a source of strength throughout this journey. I am truly fortunate to have their love and support.

Takao Miki

Table of contents

Chapter 1

General introduction

In the design of mechanical structures, shape is an important factor that influences its performance. Structural optimization is a method for obtaining an optimum configuration based on mathematical grounds. The structural optimization methods are categorized into three types, size, shape, and topology optimization, depending on the degree of design flexibility. In particular, topology optimization [11, 10] is the most flexible structural optimization method that allows the topological changes in addition to shape changes, and provides the higher performance structures than those obtained by other methods. Because the structures obtained by topology optimization are complicated shapes, additive manufacturing (AM) is attracting attention as a manufacturing technique to realize these shapes. AM is a free-form manufacturing technique that creates a three-dimensional (3D) object by stacking material layer-by-layer based on sliced two-dimensional (2D) data from a CAD file [29].

In metal AM, laser powder bed fusion (LPBF) is utilized to a wide range of industrial fields, especially the aviation industry, and its effectiveness has already been seen by optimized design in terms of performance and cost[19]. LPBF is a process that uses a laser as a heat source to selectively melt and solidify a metal powder bed. Although this process can create complex geometric parts, it is associated with manufacturing problems, such as residual stress, distortion, overheating, and overhang limitation.

The residual stress and distortion, which are physical problems, are caused by inelastic strains that occur during the melting and solidification process of the powder material. The residual stress and distortion are dependent on the part shape, and large residual stress and distortion can lead to manufacturing failure and deterioration of strength and dimensional accuracy. Furthermore, shapes that block heat flow during laser irradiation cause porosity defects and degrade surface quality, a phenomenon that is known as overheating. In contrast,

the overhang limitation is a geometrical problem that limits the overhang angle, which is the angle between the downward facing surface and the base plate. In overhanging region, the shape may collapse under its own weight during solidification because there is no support in the underlying layer. These problems can be avoided by adding support structures to the part or by redesigning the part shape. However, because the support structure must be removed after manufacturing, the manufacturing cost increases as the amount of support structure volume increases. Furthermore, redesigning the part shapes also increases manufacturing cost. Therefore, the manufacturability of AM must be considered in the design phase.

This thesis focuses on constructing topology optimization methods that take into account the above major manufacturing challenges of LPBF: distortion, heat dissipation and overhang limitation. For the distortion, we present a computationally inexpensive analytical model that predicts distortion in the LPBF building process, which is suitable for incorporation into topology optimizations that require iterative calculations. Then, we construct a topology optimization method that reduces the distortion. For the heat dissipation, we present an analytical model that represents the temperature field in the LPBF building process by transient heat transfer conduction phenomenon with volume heat flux. Then, we construct a topology optimization of the support structure that maximizes the heat dissipation in the LPBF building process. For the overhang limitation, a self-support topology optimization is constructed by introducing a partial differential equation (PDE) that extract geometric information. Furthermore, we incorporate multiple manufacturability factors such as distortion into this topology optimization.

The thesis consists of five chapters. In the remainder of this chapter, the basic concept and formulation of topology optimization techniques are briefly described. Chapter 2 describes the topology optimization considering distortion. Chapter 3 describes the topology optimization method for the support structure that maximizes heat dissipation. Chapter 4 describes the self-support topology optimization considering distortion. Lastly, Chapter 5 concludes the study.

1.1 Concept of topology optimization

Structural optimization is the problem of determining the shape Ω of a structure that the objective function F minimizes (maximizes). Because the objective function is often a physical property such as high rigidity or high thermal conductivity, it is necessary to sat-

isfy the governing equation representing the target physical phenomenon. Therefore, the optimization problem is basically formulated by the following equation with the governing equation as a constraint.

$$\begin{aligned} \inf_{\Omega \in \mathcal{U}_{ad}} \quad & F(u,\Omega) = \int_{\Omega} f(u) \mathrm{d}\Omega \\ \text{subject to:} \quad & \text{governing equation system}, \end{aligned} \tag{1.1}$$

where u is a state variable given by solving the governing equation, $f(u)$ is the integrands of the objective function, and $\mathcal{U}_{ad}$ is the admissible set in Ω. Next, the above idea of structural optimization problem is applied to topology optimization. The basic idea of topology optimization is to replace the structural optimization problem with a material distribution problem by introducing the fixed design domain $D \subset \mathbb{R}^N$ and the characteristic function χ. Where N is the number of spatial dimensions. The fixed design domain is composed of the material domain Ω and the void domain $D \backslash \Omega$, then the characteristic function that identifies the material or void is defined by the following equation.

$$\chi(\boldsymbol{x}) = \begin{cases} 1 & \text{for } \boldsymbol{x} \in \Omega, \\ 0 & \text{for } \boldsymbol{x} \in D \backslash \Omega, \end{cases} \tag{1.2}$$

where $\boldsymbol{x}$ represents a position in D. Then, the topology optimization problem is formulated by the characteristic function as follows:

$$\begin{aligned} \inf_{\chi \in \chi_{ad}} \quad & F(u,\chi) = \int_{D} f(u) \chi \mathrm{d}\Omega \\ \text{subject to:} \quad & \text{governing equation system}, \end{aligned} \tag{1.3}$$

where χ_{ad} is a subspace of the Lebesgue space $L^{\infty}(D;\{0,1\})$ and represents the admissible space formed by the characteristic function defined in D. Note that the state variable u implicitly depends on the characteristic function χ. The above characteristic function makes it possible to represent a configuration with an arbitrary topology.

1.2 Relaxation and regularization techniques of topology optimization problem

It is known that discontinuities in the characteristic function make topology optimizations problem ill-posed [2]. Therefore, the design domain must incorporate relaxation or regularization techniques to make the problem well-posed. The homogenization method [11] and density method [12] are a representative approach for relaxing the design domain. Furthermore, level-set-based shape and topology optimization methods [6, 70] that regularize the design space have been proposed. In the following subsection, we briefly explain the widely used density method and the level set method.

1.2.1 Density method

In the density method, the characteristic function $\chi(\boldsymbol{x}) \in \{0,1\}$ is replaced by a continuous function $\theta(\boldsymbol{x}) \in [0,1]$ to avoid discontinuities. This replacement gives the admissible set of shape and topology in D by $\Theta_{ad} = \{\theta \in L^{\infty}(D;[0,1])\}$. Then, the material property A that allows the intermediate state between the material and the void is represented using the density function $f(\theta)$ as follows:

$$A(\theta) = f(\theta)A_1, \tag{1.4}$$

where A_1 is the material property in the material domain Ω. In The Solid Isotropic Material with Penalization method (SIMP), which is known as one of the most popular density methods, the density function is defined as follows:

$$f(\theta) = \theta^p, \tag{1.5}$$

where p is a penalty parameter, typically 3 to 5. Then, the topology optimization problem is formulated by the density function as follows:

$$\begin{aligned} \inf_{\theta \in \Theta_{ad}} \quad & F(u,\theta) = \int_D f(u,\theta)\mathrm{d}\Omega \\ \text{subject to:} \quad & \text{governing equation system .} \end{aligned} \tag{1.6}$$

In the above optimization problem, mathematical programming method such as Sequential Linear Programming (SLP), Sequential Quadratic Programming (SQP), Optimality Criteria (OC) method, a Convex Linearization (CONLIN) method, or the Method of Moving

Asymptotes (MMA) is used to derive the distribution of the density function that represents the optimal configuration.

Because the density method is a simple formulation, it is implemented in many commercial software. However, since the above formulation allows an intermediate state called the grayscale area, there is a problem that it is difficult to interpret the intermediate material property and boundary conditions cannot be explicitly handled within the design domain.

1.2.2 Level-set-based method

In the level-set-based method, the structural boundaries $\partial\Omega$ are expressed by the iso-surface of the scalar function called the level set function. Furthermore, the two domains: the material domain and the void domain are distinguished by the sign of the level set function, as follows:

$$\begin{cases} \phi(\boldsymbol{x}) > 0 & \text{for } \boldsymbol{x} \in \Omega, \\ \phi(\boldsymbol{x}) = 0 & \text{for } \boldsymbol{x} \in \partial\Omega, \\ \phi(\boldsymbol{x}) < 0 & \text{for } \boldsymbol{x} \in D\backslash\Omega. \end{cases} \tag{1.7}$$

The profile of the level set function allows for the extraction of geometric features such as a normal vector at structural boundary $\partial\Omega$. and easy handling of the body forces. The characteristic function χ_ϕ is expressed using the level set function as follows:

$$\chi_\phi = \begin{cases} 1 & \text{for } \phi(x) \geq 0, \\ 0 & \text{for } \phi(x) < 0. \end{cases} \tag{1.8}$$

Then, the topology optimization problem is formulated by replacing the characteristic function χ as follows:

$$\begin{aligned} &\inf_{\chi_\phi \in \chi_{ad}} \quad F\left(u, \chi_\phi\right) = \int_D f(u)\chi_\phi \mathrm{d}\Omega \\ &\text{subject to:} \quad \text{governing equation system .} \end{aligned} \tag{1.9}$$

In a standard level-set-based structural optimization method [6], level set function is defined as the signed-distance function, as follows:

$$\begin{cases} \phi(\boldsymbol{x}) = d(\boldsymbol{x}, \partial\Omega) & \text{for } \boldsymbol{x} \in \Omega, \\ \phi(\boldsymbol{x}) = 0 & \text{for } \boldsymbol{x} \in \partial\Omega, \\ \phi(\boldsymbol{x}) = -d(\boldsymbol{x}, \partial\Omega) & \text{for } \boldsymbol{x} \in D\backslash\Omega, \end{cases} \tag{1.10}$$

where $d(\boldsymbol{x}, \partial\Omega)$ is the Euclidean distance function to $\partial\Omega$. Furthermore, the material property A_1 in Ω is replaced by extended material property $\tilde{A}$ using the ersatz material approach, as follows:

$$\tilde{A}(\phi) = h(\phi)A_1, \tag{1.11}$$

where $h(\phi)$ is the Heaviside function given by,

$$h(\phi) = \begin{cases} 0 & \text{for } \phi < 0, \\ 1 & \text{for } \phi \geq 0. \end{cases} \tag{1.12}$$

Most of the conventional level-set-based approaches uses interpolation treatments, in which the Heaviside function $h(\phi)$ is replaced by a continuous smoothed function $\tilde{h}(\phi)$, as follows:

$$\tilde{h}(\phi) = \begin{cases} 0 & \text{for } \phi < -\delta, \\ \frac{1}{2}\left(1 + \frac{\phi}{\delta} + \frac{1}{\pi}\sin\left(\frac{\pi\phi}{\delta}\right)\right) & \text{for } -\delta \leq \phi \leq \delta, \\ 1 & \text{for } \phi > \delta, \end{cases} \tag{1.13}$$

where $\delta > 0$ is a small parameter to control the transition width of the smoothed Heaviside function $\tilde{h}(\phi)$. To solve the above optimization problem 1.9, the problem of deriving the optimal distribution of the level set function is replaced by the problem of solving the time evolutionary equation. Specifically, by introducing a fictitious time t and assuming that the level set function depends on t implicitly, the level set function is updated using the Hamilton-Jacobi equation, as follows:

$$\frac{\partial\phi(\boldsymbol{x}, t)}{\partial t} + \boldsymbol{V} \cdot |\nabla\phi| = 0, \tag{1.14}$$

where $\boldsymbol{V}$ is a normal velocity defined as $\boldsymbol{V} = -v\boldsymbol{n}$. Note that v is a scalar function defined as the shape sensitivity analysis [6], and $\boldsymbol{n}$ is an unit normal vector given by $\boldsymbol{n} = -\nabla\phi/|\nabla\phi|$. Because this method can only handle the structural boundary $\partial\Omega$, there are no topological changes such as creating new holes during optimization procedure. Therefore, this method depends on the initial distribution of the level set function. Furthermore, the level set function needs to preserve its profile because the update scheme requires the smooth properties of the level set function. However, repeated use of the Hamilton-Jacobi equation can corrupt the profile of the level set function, so the profile must be preserved by initializing the level set function. This procedure increases the computational intensive.

On the other hand, Yamada et al. [70] proposed a level-set-based topology optimization method based on the concept of the phase field method that overcomes the above weaknesses. In this method, the profile of the level set function is defined as a piecewise constant function that takes real values between -1 and 1, as follows:

$$\begin{cases} 0 < \phi(\boldsymbol{x}) \leq 1 & \text{for } \boldsymbol{x} \in \Omega \backslash \partial\Omega, \\ \phi(\boldsymbol{x}) = 0 & \text{for } \boldsymbol{x} \in \partial\Omega, \\ -1 \leq \phi(\boldsymbol{x}) < 0 & \text{for } \boldsymbol{x} \in D \backslash \Omega. \end{cases} \tag{1.15}$$

This level set function is updated by a reaction-diffusion equation with the fictitious time t introduced, as follows:

$$\frac{\partial \phi}{\partial t} = -KF', \tag{1.16}$$

where K is a positive parameter, and F' represents the design sensitivity. Because the above level set function may be discontinuous everywhere in the fixed design domain, the level set function is regularized by adding a Laplacian term to the second term on the right side as follows:

$$\frac{\partial \phi}{\partial t} = -K(F' - \tau \nabla^2 \phi), \tag{1.17}$$

where τ is a regularization parameter that affects the degree of diffusivity when updating the level set function, i.e., as τ becomes larger, the level set function leads to a smoother distribution. Thus, by adjusting the regularization parameter τ, it is possible to qualitatively adjust the geometrical complexity of the optimal configuration. This method uses the design sensitivity determined by the topological derivative $D_{\mathrm{T}}F$ [7], which allows topology changes such as creating new holes during the optimization procedure. The topological derivative at a point $\boldsymbol{x}$ is defined as follows:

$$D_{\mathrm{T}}F(\boldsymbol{x}) = \lim_{\epsilon \to 0} \frac{F(\Omega_\epsilon) - F(\Omega)}{b(\epsilon)}, \tag{1.18}$$

where Ω_ϵ is the perturbed domain, which is the original domain Ω subtract the sphere of radius ϵ centered on point $\boldsymbol{x}$. $b(\epsilon)$ is a smooth positive function going to zero when $\epsilon \to 0$. More details of the design sensitivity F' is described in the next section.

1.3 Sensitivity analysis

In order to update the design variables, the gradient of the objective function with respect to the design variables (also called the design sensitivity) is required. This section describes two types of sensitivity analysis methods: finite difference method and adjoint method. Here, we consider an optimization problem with the equality constraints to briefly explain the sensitivity analysis methods as follows:

$$\begin{aligned} \inf_{\theta} \quad & F(u,\theta) \\ \text{subject to:} \quad & E(u,\theta) = 0, \end{aligned} \tag{1.19}$$

where E is the governing equation described by the partial differential equation. Because the relationship between the state variable u and the design variable θ cannot be expressed explicitly, it is necessary to solve the governing equation to obtain the state field. The following subsections describe the each sensitivity analysis method for obtaining design sensitivity $F' = \frac{\mathrm{d}F}{\mathrm{d}\theta}$, using the density method based topology optimization problem as an example.

1.3.1 Finite difference method

Finite difference method approximates the derivative by finite differences. First, the forward difference of the objective function when the design variable θ is perturbed in the direction ψ is given by:

$$\frac{\mathrm{d}F}{\mathrm{d}\theta} \approx \frac{F(u(\theta+\epsilon\psi),\theta+\epsilon\psi) - F(u,\theta)}{\epsilon}, \tag{1.20}$$

where $\epsilon > 0$ is positive parameter that represents the degree of the perturbation of θ. Next, the backward difference is given by:

$$\frac{\mathrm{d}F}{\mathrm{d}\theta} \approx \frac{F(u,\theta) - F(u(\theta-\epsilon\psi),\theta-\epsilon\psi)}{\epsilon}. \tag{1.21}$$

These differences have first-order accuracy. On the other hand, the central difference method with second-order accuracy is as follows:

$$\frac{\mathrm{d}F}{\mathrm{d}\theta} \approx \frac{F(u(\theta+\epsilon\psi),\theta+\epsilon\psi) - F(u(\theta-\epsilon\psi),\theta-\epsilon\psi)}{2\epsilon}. \tag{1.22}$$

The finite difference method has the advantage of being easy to implement, but it has the disadvantage of being computationally expensive because it requires the analysis of the same number of state fields as the number of design variables. The state field is generally solved using the finite element method, so the number of design variables implies the number of elements. Therefore, when the dimensions of the design space become large, such as three dimensions, the computational cost becomes enormous, which is an unrealistic method. The next subsection describes a method that does not increase the computational cost even when dealing with a large number of design variables.

1.3.2 Adjoint variable method

In the adjoint variable method, the design sensitivity can be obtained by solving the adjoint equation corresponding to the governing equation. This method uses the Lagrange multiplier method to find the extremal values of a function under constrained conditions. The Lagrangian $\mathcal{L}$ is defined, as follows:

$$\mathcal{L}(\theta, v, q) = F(v, \theta) + qE(v, \theta), \tag{1.23}$$

where q is the Lagrange multiplier. Note that v is a function independent from θ. We now consider the optimal conditions for above Lagrangian with the variables θ, v, q. First, a stationary condition where the gradient with respect to the direction q is equal to zero is given by:

$$\frac{\partial \mathcal{L}(\theta, v, q)}{\partial q} = 0 = E(v, \theta). \tag{1.24}$$

Above equation means that if the variable v is equal to the solution u of the governing equation, it gives the stationary condition for the variable q. Next, the stationary condition where the gradient with respect to the direction v is equal to zero is given by:

$$\frac{\partial \mathcal{L}(\theta, v, q)}{\partial v} = 0 = \frac{\partial F(v, \theta)}{\partial v} + \left(\frac{\partial E(v, \theta)}{\partial v}\right)^{\mathsf{T}} q. \tag{1.25}$$

Above equation means that if the variable q is equal to the solution p of the following adjoint equation, it gives the stationary condition for the variable v. The adjoint eqation is given as:

$$\left(\frac{\partial E(v, \theta)}{\partial v}\right)^{\mathsf{T}} p = -\frac{\partial F(v, \theta)}{\partial v}. \tag{1.26}$$

Finally, the gradient of the Lagrangian $\mathcal{L}$ with respect to the direction θ is given by:

$$\frac{\mathrm{d}\mathcal{L}(\theta,v,q)}{\mathrm{d}\theta} = \frac{\partial\mathcal{L}(\theta,v,q)}{\partial\theta} + \frac{\partial\mathcal{L}(\theta,v,q)}{\partial v}\cdot\frac{\partial v}{\partial\theta} + \frac{\partial\mathcal{L}(\theta,v,q)}{\partial q}\cdot\frac{\partial q}{\partial\theta}. \tag{1.27}$$

Because the above equation is $\mathcal{L} = F$ at the stationary condition($v = u, q = p$), the design sensitivity is given as:

$$\frac{\mathrm{d}F}{\mathrm{d}\theta} = \frac{\partial F(u,\theta)}{\partial u} + p\cdot\left(\frac{\partial E(u,\theta)}{\partial u}\right). \tag{1.28}$$

Therefore, the gradient of the objective function F with respect to the design variable θ can be evaluated by solving the governing and adjoint equations and obtaining the stationary conditions u and p for v and q. Because the topology optimization in this thesis is based on the finite element method and deals with a large number of design variables, the adjoint variable method is employed.

1.4 Summary

This chapter provided our research background and an overview of topology optimization. First, we explained the application of the structural optimization problem to the topology optimization problem and that the formulated optimization problem is ill-posed. Then, we introduced two typical approaches to make a topology optimization problem well-posed: the density and level-set-based method. The density method is the approach that convexizes the design space by replacing discontinuous characteristic chfunction with continuous function. This method is employed in many commercial softwares due to its simplicity of implementation, but it yields a grayscale area with no clear structural boundary. In contrast, the level set method introduces a level set function to clearly represent the structural boundary. However, the general level set method uses the shape derivative to update the design variables, so the topology does not change. On the other hand, the level-set-based topology optimization proposed by Yamada et al. overcomes this problem by introducing the topological derivative. Finally, we described two types of evaluation methods for the gradient of the objective function required to update the design variables. The finite difference method is easy to derive, but it is not suitable for topology optimization because many design variables increase the computational cost. On the other hand, the adjoint variable method is a very efficient method for topology optimization because it does not increase the computational cost even when there are many design variables.

Chapter 2

Topology optimization considering the distortion in additive manufacturing

2.1 Introduction

Residual stress and distortion must be considered during the design phase because these physical problems can hinder manufacturing success. In this chapter, we propose a topology optimization method that reduces the distortion induced by LPBF process.

In the LPBF process, materials are melted and solidified by rapid local heating and cooling. This heating and cooling cycle generates thermal, plastic, and transformation strains, which cause residual stress and distortion. These adversely affect the strength and dimensional accuracy of the manufactured parts. Therefore, predicting and avoiding residual stress and distortion are crucial issues.

Residual stress and distortion in AM have been studied extensively using experimental and numerical methods [36, 44, 64, 69, 21, 42, 13]. Existing numerical methods can be summarized into two approaches: the thermal-elastic-plastic analysis method [63] and the inherent strain method [61, 47] that was originally used in welding. The thermal-elastic-plastic analysis method is a coupled analysis that combines heat transfer analysis and elastic or elastic-plastic analysis. Heat transfer analysis uses a detailed model with a moving heat source and the micro-scale layer thickness makes it computationally expensive. In the elastic-plastic analysis, it is necessary to consider the nonlinearity of the material properties and the solid-liquid phase transition. To address this, many simplified methods have been proposed to predict the residual stress and distortion on a part-scale

[50, 33, 39, 46, 18, 17, 41]. However, it is difficult to replace the moving heat source with a simplified heat source, and the effectiveness of these analytical models has not been firmly established. In contrast, with the inherent strain method, the strain component is identified experimentally from the fabricated part and applied to an analysis domain. Then, the residual stress and distortion are obtained by linear elastic analysis. This makes it is computationally inexpensive compared to the thermal-elastic-plastic analysis method in that it does not require coupled and nonlinear analyses. The effectiveness and validity of the inherent strain method have been established previously by experimental verification [35, 58, 15, 43, 54]. Based on these numerical analysis methods, topology optimization methods have been proposed that reduce the residual stress and distortion in AM. Wildman et al. [68] proposed a multi-objective topology optimization method using a solid isotropic material with penalization scheme and defined the objective function for mean compliance and reducing the induced distortion. A thermo-elastic element-birth model is thus proposed in which the elements are sequentially activated to simulate the moving heat source. Allaire et al. [5] proposed a layer-by-layer thermo-elastic analysis model and incorporated it into a level set-based topology optimization to minimize the distortion and residual stress in each layer with an objective function. In this approach, the optimal configuration obtained from a mean compliance minimization problem is reoptimized as the initial shape. By introducing the mean compliance and a predefined stress threshold as constraints to the optimization problem, the optimization method succeeded in minimizing the mean compliance and reducing the residual stress. However, both approaches are computationally intensive, owing to the use of coupled analysis in the AM analytical model. This makes the methods inefficient for topology optimization that requires iterative procedures. In addition, the validity of the proposed analytical models have not been established.

In this chapter, we present a topology optimization method by considering the part distortion in AM, using a computationally inexpensive analytical model. Specifically, we propose an analytical model based on the inherent strain method that realizes computationally inexpensive and accurate numerical analysis to predict the residual stress and distortion. The proposed model is incorporated into a topology optimization process to obtain optimal high-performance configurations that account for the part distortion in AM.

The remainder of this chapter is organized as follows. First, we propose an analytical model based on the inherent strain method for predicting the residual stress and distortion in the AM building process. Then, we introduce an identification method of the inherent strain

component, and present an experimental validation of the proposed analytical model. Next, we formulate an optimization problem that incorporates the reduction of part distortion in the topology optimization procedure, and derive an approximate topological derivative using variational analysis and the adjoint variable method. Furthermore, we constructed an optimization algorithm for the topology optimization using the finite element method (FEM). Finally, we present 2D and 3D design examples to demonstrate the validity of the proposed optimization method.

2.2 Analytical model for AM

In this section, the layer-by-layer type building process in AM is modeled using the inherent strain method, a type of linear elastic analysis. The reason for using such a method is that optimization requires iterative calculations, therefore, computationally inexpensive models are desirable. To simplify the model, we assume that a constant strain is associated with each layer.

2.2.1 Inherent strain method

In the AM building process, inelastic strains such as thermal, plastic, and phase transformation strains are induced in the parts through the melting-solidification cycle of the material. The sum of these inelastic strains is called the inherent strain [61, 47]. The total strain $\boldsymbol{\varepsilon}(\boldsymbol{u})$ can be divided into the elastic strain $\boldsymbol{\varepsilon}^{el}$ and inherent strain $\boldsymbol{\varepsilon}^{inh}$. The inherent strain $\boldsymbol{\varepsilon}^{inh}$ and the stress tensor $\boldsymbol{\sigma}$ are defined as:

$$\boldsymbol{\varepsilon}(\boldsymbol{u}) = \boldsymbol{\varepsilon}^{el} + \boldsymbol{\varepsilon}^{inh}, \tag{2.1}$$

$$\boldsymbol{\sigma} = \mathbb{C}\boldsymbol{\varepsilon}^{el} = \mathbb{C}\boldsymbol{\varepsilon}(\boldsymbol{u}) - \mathbb{C}\boldsymbol{\varepsilon}^{inh}, \tag{2.2}$$

where $\mathbb{C}$ is the fourth-order elasticity tensor. For an isotropic elastic material, the above tensor is given by:

$$\mathbb{C}_{ijkl} = E\left(\frac{\nu}{(1+\nu)(1-2\nu)}\delta_{ij}\delta_{kl} + \frac{1}{2(1+\nu)}\left(\delta_{ik}\delta_{jl} + \delta_{il}\delta_{jk}\right)\right), \tag{2.3}$$

with Young's modulus E, the Poisson's ratio ν and the Kronecker delta δ_{ij}. The residual stress and distortion can be predicted using a linear analysis by applying the inherent strain

in a layer-by-layer manner. As shown in Fig. 2.1, we consider an analysis domain Ω,

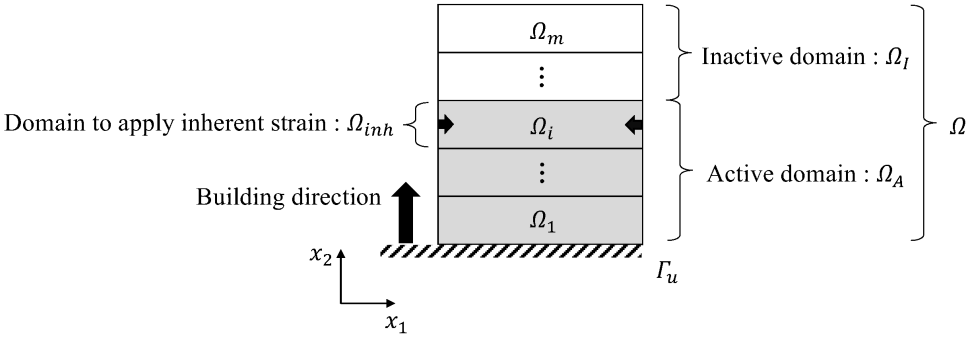

Fig. 2.1 Domains and boundary in the middle of the building process.

divided into m layers with a fixed thickness in the building direction. The analysis domain Ω is defined by each domain Ω_i for $1 \leq i \leq m$ as follows:

$$\Omega = \Omega_1 \cup \ldots \cup \Omega_i \cup \ldots \cup \Omega_m. \tag{2.4}$$

Here, we introduce three subdomains as: the active domain Ω_A, the inactive domain Ω_I, and the domain Ω_{inh} to which the inherent strain is applied. The subdomain region depends on the domain number i, and each subdomain is defined as:

$$\Omega_A = \Omega_1 \cup \ldots \cup \Omega_i, \tag{2.5}$$

$$\Omega_I = \Omega \setminus \Omega_A, \tag{2.6}$$

$$\Omega_{inh} = \Omega_i \subset \Omega_A. \tag{2.7}$$

The active domain Ω_A is filled with an elastic material, and a fixed displacement boundary condition is applied to the bottom of the domain Γ_u. The mechanical unknown of this model is the displacement field. The displacement $\boldsymbol{u}_i \in \mathcal{U}$ with the inherent strain applied to the domain Ω_{inh} is governed by the equations of linear elasticity as follows:

$$\begin{cases} -\mathrm{div}(\boldsymbol{\sigma}_i) = 0 & \text{in } \Omega_A, \\ \boldsymbol{\sigma}_i = \mathbb{C}\boldsymbol{\varepsilon}(\boldsymbol{u}_i) - \mathbb{C}\boldsymbol{\varepsilon}^{inh}, & \\ \boldsymbol{u}_i = \boldsymbol{0} & \text{on } \Gamma_u, \\ -\boldsymbol{\sigma}_i \cdot \boldsymbol{n} = \boldsymbol{0} & \text{on } \partial\Omega_A \setminus \Gamma_u, \end{cases} \tag{2.8}$$

$$\mathcal{U} := \left\{ \boldsymbol{u}_i \in H^1_{\Gamma_u}(\Omega_A)^N,\ \boldsymbol{u}_i = \boldsymbol{0} \ \text{ on } \ \Gamma_u \right\}, \tag{2.9}$$

for all indices $i = 1, 2, \ldots, m$, where N is the number of spatial dimensions. The inherent strain $\boldsymbol{\varepsilon}^{inh}$ at the domain Ω_{inh} is defined as:

$$\boldsymbol{\varepsilon}^{inh}(\boldsymbol{x}) = \begin{cases} \boldsymbol{\varepsilon}^{inh} & \text{for } \boldsymbol{x} \in \Omega_{inh}, \\ \boldsymbol{0} & \text{otherwise}, \end{cases} \tag{2.10}$$

where $\boldsymbol{x}$ represents a point located in Ω_A. The method for identifying the inherent strain component of Eq. 2.10 is described in the next section.

2.2.2 AM building process model

The AM building process is represented by various activation strategies in finite element modeling [17, 58, 68, 5, 22]. In this study, we use a method in which the inactive domain is activated sequentially from the bottom domain, and the inherent strain is applied to each activated domain. To solve the analysis domain Ω using FEM, we use an ersatz material approach in which the inactive domain Ω_I is occupied by a structural material with a relatively small Young's modulus.

Our AM building process algorithm is as follows:

Step1. Inactivate all domains in the analysis domain divided into m layers.

Step2. The domains are activated in sequence from the bottom domain, i.e., the activated domain is replaced by the original Young's modulus, and the inherent strain is applied after this.

Step3. The displacement field $\boldsymbol{u}_i$ defined in Eqs. 2.8 and 2.9 is solved using FEM.

Step4. If all domains are activated, the procedure is terminated; otherwise, return to the second step.

The analysis domain is divided into fewer layers than the actual number of layers during manufacturing, owing to the computational costs. This multi-scale modeling enables the prediction of the part-scale residual stress and distortion. The final residual stress $\boldsymbol{\sigma}$ and distortion $\boldsymbol{u}$ of the part are the sums of the residual stress $\boldsymbol{\sigma}_i$ and distortion $\boldsymbol{u}_i$ solved for

each active domain Ω_A, as follows: [43]

$$\boldsymbol{\sigma} = \sum_{i=1}^{m} \boldsymbol{\sigma}_i \quad \text{for } \boldsymbol{x} \in \Omega_A, \tag{2.11}$$

$$\boldsymbol{u} = \sum_{i=1}^{m} \boldsymbol{u}_i \quad \text{for } \boldsymbol{x} \in \Omega_A. \tag{2.12}$$

2.3 Inherent strain identification method

2.3.1 Experimental procedure

The unknown inherent strain component can be identified based on the measurements of a deformation caused by releasing the elastic strain [61, 62]. The elastic strain needs to be released such that the inherent strain is unchanged, using devices such as wire electric discharge machines (WEDM). Specimens were fabricated using an LPBF machine (EOSINT M280, EOS GmbH) equipped with a 400 W fiber laser (beam diameter: approximately 0.1 mm). Figure. 2.2 shows the geometry of the specimen and its dimensions. The beam thick-

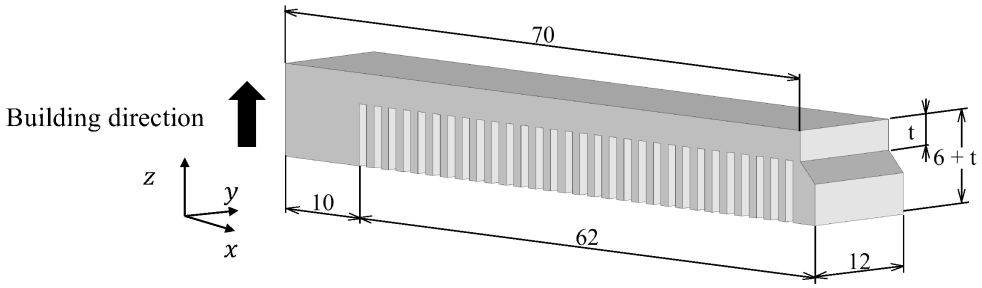

Fig. 2.2 Cantilever specimen with the dimensions in mm.

ness (3 mm) is represented by t. The specimens made of AlSi10Mg (EOS Aluminum, EOS GmbH) were fabricated on the substrate with an argon atmosphere. The laser scanning parameters used an original EOS parameter set adjusted for laser power, scan speed, and scan distance. The laser scanning pattern was rotated by 67° layer-by-layer, as shown in Fig. 2.3, and the constant material layer thickness was 0.03 mm.

After fabrication, the specimen was partially cut with WEDM at a height of 3 mm from the substrate, leaving the left column attached to the substrate, as shown in Fig. 2.4. The elastic strain is released upon cutting, leading to a large deformation of the specimens. The vertical deformation was calculated from the difference in the top surfaces before and

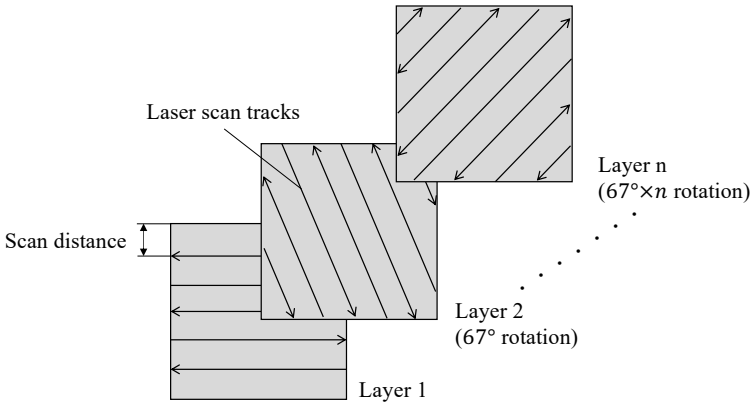

Fig. 2.3 Schematic illustration of the laser scanning pattern.

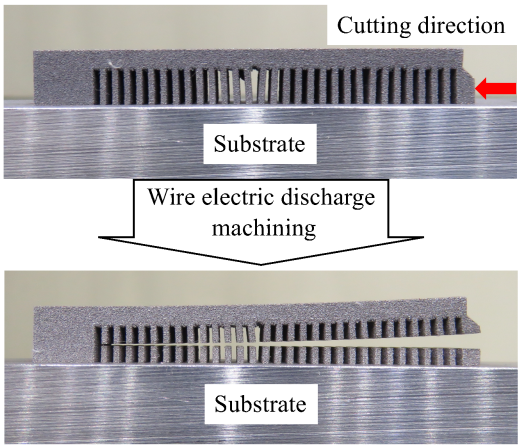

Fig. 2.4 Schematic diagram of the specimens being cut.

after cutting, which were measured using an optical three-dimensional scanner (ATOS Core, GOM GmbH). The inherent strain component was identified from the experimental and numerical results.

2.3.2 Finite element modeling

Figure 2.5 shows the mesh and analysis conditions for the AM building and cutting processes. In the AM building process, the displacements of the bottom surfaces are fixed, where the color difference represents each layer to which the inherent strain is applied sequentially. The elasticity problem is solved layer-by-layer according to the AM building process algorithm to determine the elastic strain of the specimen. In the cutting process,

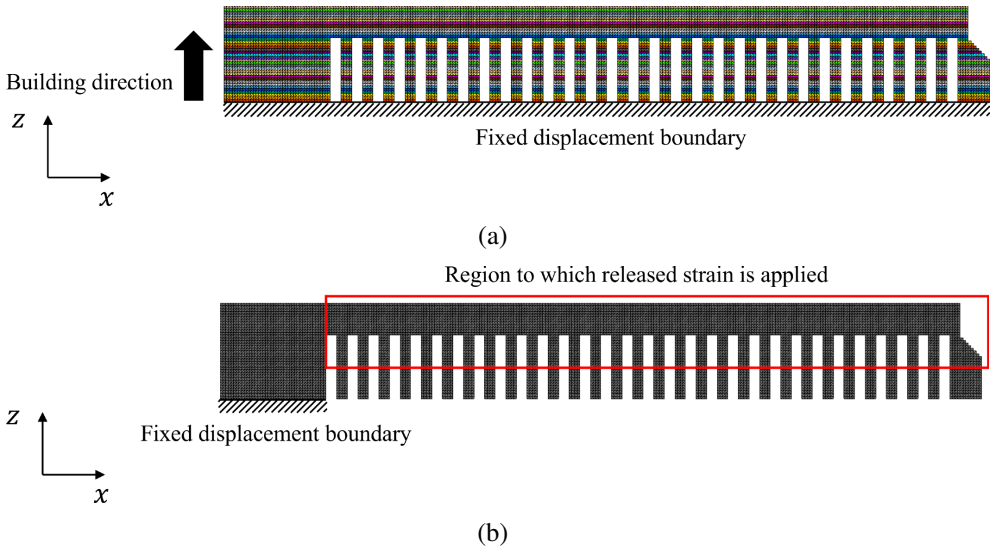

Fig. 2.5 Boundary conditions and mesh model of the cantilever beam t = 3 mm: (a) AM building process model and (b) cutting model.

only the bottom surface of the left column is fixed, and the elastic strain released by cutting is applied to the part to determine the deformation. The region of the applied elastic strain is demarcated by the red rectangular frame (3 mm height from the bottom and unfixed area). In this study, the layer thickness was discretized with an element size of 0.25 mm for the part-scale analysis, which is approximately 10 times the actual material layer thickness in the fabrication. The mesh applied to discretization consists of 2,114,496 second-order tetrahedral elements. In addition, the Young's modulus for the active and inactive domains were set to 75 GPa and 0.01 MPa, respectively and Poisson's ratio was set to 0.34.

2.3.3 Identification procedure

The inherent strain component has been identified under two assumptions. First, the fabricated parts shrink isotropically as the laser scan pattern rotates layer-by-layer. Therefore, the in-plane components are assumed to have the same value [58]. Second, because the layer thickness is extremely small compared to the part size, the building direction component is assumed to be zero [13, 58]. The in-plane inherent strain components were obtained through the minimization of the residual sum of squares of the experimental and numerical vertical deformation results. Figure 2.6 shows the comparison between the numerical and experimental result of the vertical deformation of the top surface after minimization.

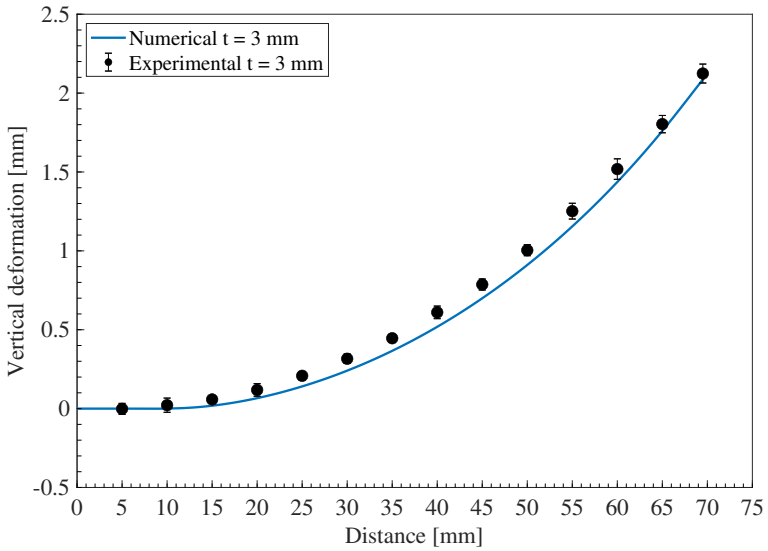

Fig. 2.6 Comparison of the experimental and numerical results of the vertical deformation after the inherent strain identification procedure.

The experimental result was plotted for the vertical deformation of the top surface at cross-sections measured every 5 mm along the x-direction. The error bars represent the minimum and maximum values in the cross-section. The inherent strain component obtained by this procedure is as follows:

$$\boldsymbol{\varepsilon}^{inh} = \left\{ \begin{array}{c} \varepsilon_x \\ \varepsilon_y \\ \varepsilon_z \end{array} \right\} = \left\{ \begin{array}{c} -0.0025 \\ -0.0025 \\ 0 \end{array} \right\}. \tag{2.13}$$

2.4 Validation of analytical model

The validity of the identified inherent strain and the proposed analytical model were verified through two types of experiments. First, to verify the validity of predicting the distortion, we prepared a cantilever specimen with the beam thickness t shown in Fig. 2.2 set to 5 mm, then presents a comparison of the experimental and numerical results of the vertical deformation after cutting the specimen. The cantilever specimen made of AlSi10Mg was fabricated under the same manufacturing conditions the beam with thickness t = 3 mm. After fabrication, the specimen was cut by WEDM, and the deformation was measured with the optical three-dimensional scanner. In the numerical analysis, we prepared two models that the element sizes per layer were discretized at 0.25 mm and 1 mm to compare the

accuracy and computational time, as shown in Fig. 2.7. The meshes of the two models consist of 2,759,616 and 43,272 second-order tetrahedral elements, respectively. The same boundary condition, material properties, and inherent strain as in the beam with thickness $t = 3$ mm were used.

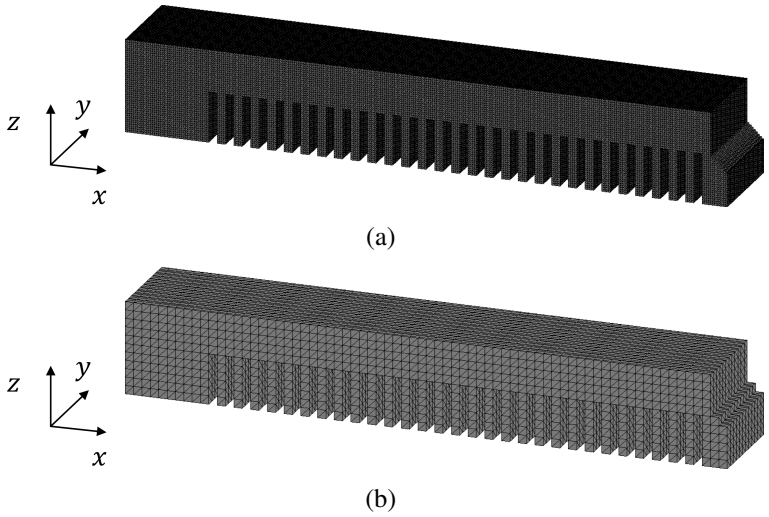

Fig. 2.7 Mesh model of the cantilever specimen $t = 5$ mm: (a) element size of 0.25 mm; (b) element size of 1.0 mm.

Figure 2.8 shows the comparison between the numerical and experimental results for the vertical deformation of the top surface. The experimental result was plotted for the vertical deformation of the top surface at cross-sections measured every 5 mm along the x-direction. The error bars represent the minimum and maximum values in the cross-section. The numerical results for the two different element sizes are consistent with the experimental measurements. This verification demonstrates that the part-scale distortion induced in the AM building process can be accurately predicted for both element sizes. Table 2.1 shows the computational times for both cases using 10 Intel Xeon E5-2687W cores. The computational time for the 1.0 mm model is approximately $1/180^{\text{th}}$ that of the 0.25 mm model.

Next, to verify the validity of predicting the residual stress, we compared the experimental and numerical results of the residual stress distribution. A cubic specimen (10mm $\times$ 10mm $\times$ 10mm) made of AlSi10Mg was fabricated under the same manufacturing conditions as for the cantilever specimen. To measure the residual stress distribution in the building direction, the specimen was successively removed from the top surface by elec-

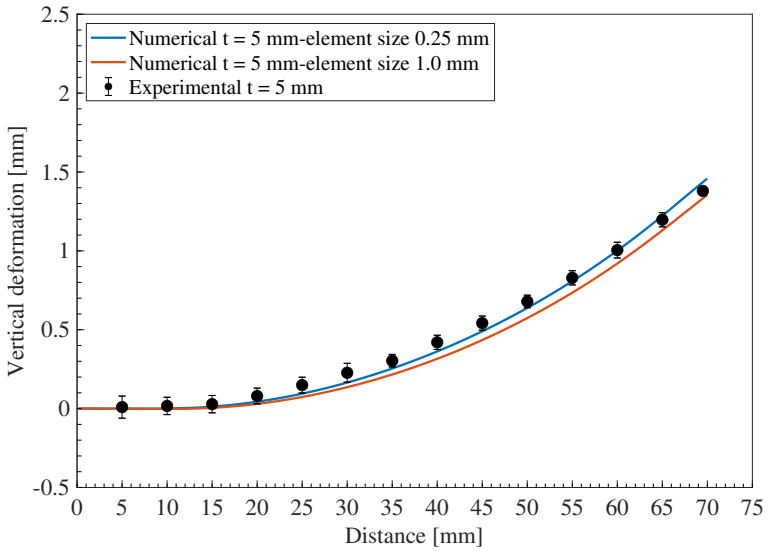

Fig. 2.8 Comparison of the experimental and numerical results of the vertical deformation after cutting with WEDM.

Table 2.1 Computational time for the analysis of the cantilever model with different element sizes.

Element size of layer thickness (mm)	0.25	1.0
Computational time (min)	314.2	1.75

trolytic polishing, and the stress was measured by X-ray diffraction (μ -X360, PULSTEC INDUSTRIAL CO., LTD.). The measurement conditions are shown in Table 2.2. The X-rays were applied to the center of the surface; the specimen was removed from the top surface to a depth of 2 mm. Similar to the verification of the validity of predicting the

Table 2.2 Measurement conditions.

X-ray tube	Cr-Kα
Tube voltage / current	30 kV / 1mA
Diffraction plane	Al {2 2 2}
Incident angle	35 deg
Irradiation area	2 mm

distortion, we prepared two models with element sizes of 0.25 mm and 1.0 mm, as shown in Fig.2.9. The meshes of the two models consist of 384,000 and 6,000 second-order tetra-

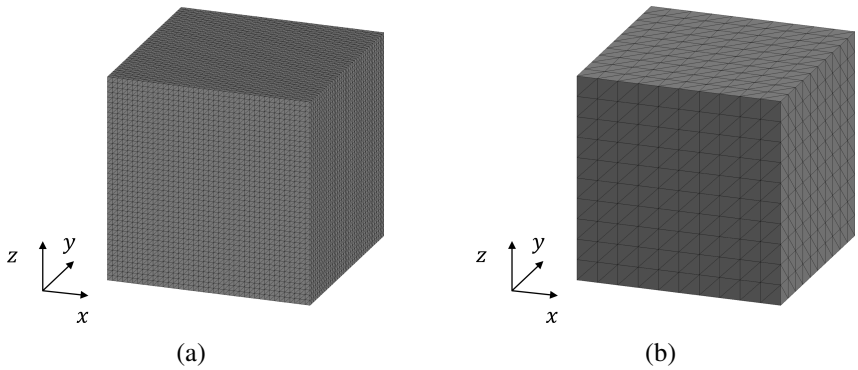

Fig. 2.9 Mesh model of the cubic specimen: (a) element size of 0.25 mm; (b) element size of 1.0 mm.

hedral elements, respectively. We then evaluated the accuracy and computational time. The material properties and the inherent strain were set to the same values as in the analysis of the cantilever specimen.

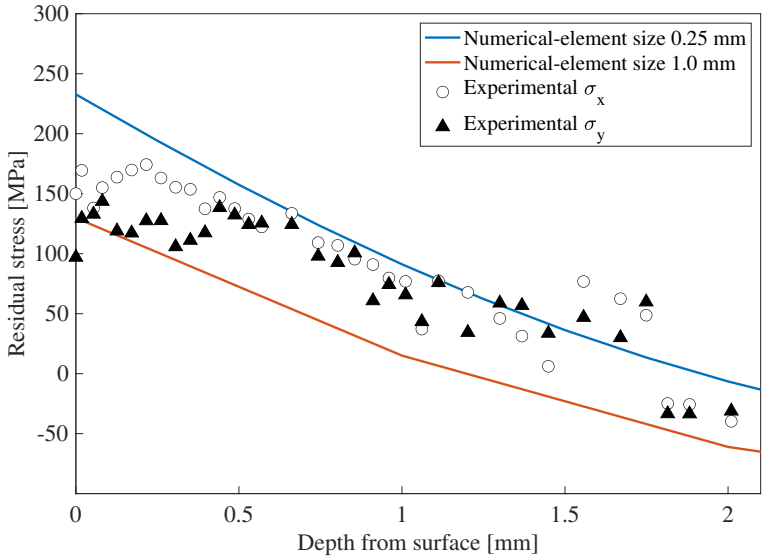

Fig. 2.10 Comparison of the experimental and numerical results of the residual stress distribution depth profile.

Figure 2.10 shows the comparison between the numerical and experimental results in terms of the residual stress depth profile. In both results, the maximum tensile stress was generated on the top surface that decreased gradually toward the bottom surface, where it changed to compressive stress. This is because when the new layer solidifies and shrinks,

Table 2.3 Computational time for the analysis of the cube model with different element sizes.

Element size of layer thickness (mm)	0.25	1.0
Computational time (min)	41.2	0.26

it is restrained by the previously solidified layer, inducing a tensile force on the top surface and a compressive force on the previous layer [44, 42]. This verification demonstrated that the residual stress could be predicted accurately for both element sizes. Table 2.3 shows the computational time for both cases using 10 Intel Xeon E5-2687W cores. The computational time for the 1.0 mm model is approximately $1/160^{\text{th}}$ that of the 0.25 mm element size model. Considering the incorporation into topology optimization with iterative calculations, the element size per layer should be approximately 30 times that of the actual material layer thickness in manufacturing, i.e., the element size per layer should be 1.0 mm to reduce the computational costs in our method. From the above, we confirmed the validity of the analytical model, and estimated the element size suitable for topology optimization.

2.5 Topology optimization considering part distortion in AM

2.5.1 Formulation of optimization problem

We incorporate the proposed AM analytical model into the optimization framework described in the previous section. The objective function for reducing the part distortion can be represented by minimizing the following equation:

$$F_{AM} = \left(\int_{\Omega} |\boldsymbol{u}|^{\beta} \, d\Omega \right)^{1/\beta}, \tag{2.14}$$

where $\beta \geq 2$ is a fixed weighting parameter. Increasing β leads to the minimization of the maximum distortion and decreasing β leads to the minimization of the average distortion. Furthermore, $\boldsymbol{u}$ is the sum of the distortion $\boldsymbol{u}_i (i = 1, 2, \ldots, m)$ in each active domain Ω_A, expressed by:

$$\boldsymbol{u} = \sum_{i=1}^{m} \boldsymbol{u}_i \quad \text{for } \boldsymbol{x} \in \Omega_A. \tag{2.15}$$

In this study, we formulate the minimum mean compliance problem considering the part distortion in AM using the above objective function. Consider the material domain Ω fixed at the boundary Γ_v , with a traction $\boldsymbol{t}$ applied at Γ_t. The displacement field is denoted as $\boldsymbol{v} \in \mathcal{V}$ in the static equilibrium state. The objective function of this problem is represented by minimizing the following equation

$$F_{MC} = \int_{\Gamma_t} \boldsymbol{t} \cdot \boldsymbol{v} d\Gamma. \tag{2.16}$$

Thus, the optimization problem to determine an optimal configuration of the material domain Ω that has the minimum mean compliance and reduces the part distortion under a volume constraint can be formulated as follows:

$$\begin{aligned}
\inf_{\tilde{\chi}} \quad & F = (1-\alpha)F_{MC} + \alpha F_{AM}, \\
\text{subject to}: \ & G = \int_D \tilde{\chi}\, d\Omega - V_{\max} \leq 0, \\
& -\operatorname{div}(\mathbb{C}\boldsymbol{\varepsilon}(\boldsymbol{v})) = 0 && \text{in } \Omega, \\
& \boldsymbol{v} = \boldsymbol{0} && \text{on } \Gamma_v, \\
& -(\mathbb{C}\boldsymbol{\varepsilon}(\boldsymbol{v})) \cdot \boldsymbol{n} = \boldsymbol{0} && \text{on } \partial\Omega \setminus \Gamma_t \cup \Gamma_v, \\
& -(\mathbb{C}\boldsymbol{\varepsilon}(\boldsymbol{v})) \cdot \boldsymbol{n} = \boldsymbol{t} && \text{on } \Gamma_t, \\
& -\operatorname{div}(\mathbb{C}\boldsymbol{\varepsilon}(\boldsymbol{u}_i) - \mathbb{C}\boldsymbol{\varepsilon}^{inh}) = 0 && \text{in } \Omega_A, \\
& \boldsymbol{u}_i = \boldsymbol{0} && \text{on } \Gamma_u, \\
& -(\mathbb{C}\boldsymbol{\varepsilon}(\boldsymbol{u}_i) - \mathbb{C}\boldsymbol{\varepsilon}^{inh}) \cdot \boldsymbol{n} = \boldsymbol{0} && \text{on } \partial\Omega_A \setminus \Gamma_u,
\end{aligned} \tag{2.17}$$

$$\begin{aligned}
\mathcal{V} &:= \left\{ \boldsymbol{v} \in H^1_{\Gamma_u}(\Omega)^N,\ \boldsymbol{v} = \boldsymbol{0} \ \text{ on } \ \Gamma_v \right\}, \\
\mathcal{U} &:= \left\{ \boldsymbol{u}_i \in H^1_{\Gamma_v}(\Omega_A)^N,\ \boldsymbol{u}_i = \boldsymbol{0} \ \text{ on } \ \Gamma_u \right\},
\end{aligned} \tag{2.18}$$

for all indices $i = 1, 2, \ldots, m$, where $0 \leq \alpha \leq 1$ is a weighting coefficient, and N is the number of spatial dimensions. In the above formulation, G represents the volume constraint and V_{max} is the upper limit of the material volume in D.

2.5.2 Sensitivity analysis

To derive the topological derivative of the above optimization problem, we use the adjoint variable method. The minimum mean compliance problem is known to be a self-adjoint problem. Therefore, the adjoint variable corresponds to the displacement field $\boldsymbol{v}$, and the topological derivative of Eq. 2.16 is given by [26, 20]

$$F'_{MC} = -\boldsymbol{\varepsilon}(\boldsymbol{v}) : \mathbb{A} : \boldsymbol{\varepsilon}(\boldsymbol{v}). \tag{2.19}$$

For a plane stress problem, the constant fourth-order tensor $\mathbb{A}$ is given by:

$$\mathbb{A}_{ijkl} = \frac{1}{(1+\nu)^2}\left\{\frac{-\left(1-6\nu+\nu^2\right)E}{(1-\nu)^2}\delta_{ij}\delta_{kl} + 2E\left(\delta_{ik}\delta_{jl}+\delta_{il}\delta_{jk}\right)\right\}. \tag{2.20}$$

Next, we consider an adjoint state $\tilde{\boldsymbol{u}}_i \in \mathcal{U}$ for the displacement field $\boldsymbol{u}_i$ of the part distortion in AM. We introduce the following adjoint system associated with the objective function Eq. 2.14:

$$\begin{cases} -\mathrm{div}(\mathbb{C}\boldsymbol{\varepsilon}(\tilde{\boldsymbol{u}}_i)) = -\left(\int_\Omega |\boldsymbol{u}|^\beta \, d\Omega\right)^{1/\beta-1} |\boldsymbol{u}|^{\beta-2}\boldsymbol{u} & \text{in } \Omega_A, \\ \tilde{\boldsymbol{u}}_i = \boldsymbol{0} & \text{on } \Gamma_u, \\ -(\mathbb{C}\boldsymbol{\varepsilon}(\tilde{\boldsymbol{u}}_i))\cdot\boldsymbol{n} = \boldsymbol{0} & \text{on } \partial\Omega_A \setminus \Gamma_u, \end{cases} \tag{2.21}$$

for all indices $i = 1, 2, \ldots, m$, and the topological derivative of Eq. 2.14 is defined as follows [31]:

$$F'_{AM} = \sum_{i=1}^{m}\left(-\boldsymbol{\varepsilon}(\boldsymbol{u}_i) : \mathbb{A} : \boldsymbol{\varepsilon}(\tilde{\boldsymbol{u}}_i) + \boldsymbol{\varepsilon}^{inh} : \mathbb{A} : \boldsymbol{\varepsilon}(\tilde{\boldsymbol{u}}_i)\right). \tag{2.22}$$

2.6 Numerical implementation

2.6.1 Optimization algorithm

The optimization algorithm is as follows.

Step1. The initial level set function is set.

Step2. The displacement fields $\boldsymbol{v}$ and $\boldsymbol{u}_i$ defined in Eqs. 2.17 and 2.18 are solved using FEM.

Step3. The objective function F formulated using Eqs. 2.14 and 2.16 is calculated.

Step4. If the objective function converges, the optimization procedure is terminated; otherwise, the adjoint field $\tilde{\boldsymbol{u}}_i$ defined in Eq. 2.21 is solved using FEM, and the topological derivatives with respect to the objective function are calculated using Eqs. 2.19 and 2.22.

Step5. The level set function is updated using the time evolution equation given by Eq. 1.17, and then, the optimization procedure returns to the second step.

2.6.2 Numerical scheme for the governing equation

The finite elements are generated during the iterative optimization procedure. From the perspective of computational cost, we use the ersatz material approach [6]. We assume that the void domain is a structural material with a relatively small Young's modulus. In addition, we assume that the boundary between the material and void domains has a smoothly distributed material property; i.e., we use the extended elastic tensor $\tilde{\mathbb{C}}$ to solve the governing equations Eqs. 2.17 and 2.18 in the fixed design domain D as follows:

$$\tilde{\mathbb{C}}(\phi; w) = \{(1-d)H(\phi; w) + d\}\,\mathbb{C}, \tag{2.23}$$

where $H(\phi; w)$ is defined as:

$$H(\phi; w) := \begin{cases} 1 & \text{for } \phi > w, \\ \frac{1}{2} + \frac{\phi}{w}\left(\frac{15}{16} - \frac{\phi^2}{w^2}\left(\frac{5}{8} - \frac{3}{16}\frac{\phi^2}{w^2}\right)\right) & \text{for } -w \le \phi \le w, \\ 0 & \text{for } \phi < -w, \end{cases} \tag{2.24}$$

with w representing the width of the transition, and d the ratio of the Young's modulus for the structural and void materials.

2.6.3 Normalization for topological derivative scaling

The scale of the topological derivative F'_{MC} and F'_{AM} is significantly affected by the fixed design domain scale and boundary condition settings, therefore, we used a normalized topo-

logical derivative $\tilde{F}'$ defined by:

$$\tilde{F}' = (1-\alpha)\frac{F'_{MC}\int_D d\Omega}{\int_D |F'_{MC}| d\Omega} + \alpha\frac{F'_{AM}\int_D d\Omega}{\int_D |F'_{AM}| d\Omega}. \tag{2.25}$$

2.7 Numerical examples

In this section, numerical examples are presented to demonstrate the effectiveness and validity of the proposed optimization method for 2D and 3D minimum compliance problems that consider the part distortion in AM.

2.7.1 2D design examples

First, we examined the dependency of the optimal configurations with respect to the different settings of the regularization parameter τ and weighting coefficient α through 2D design problems. The fixed design domain and boundary conditions of the two models are shown in Figs. 2.11 and 2.12, respectively. The fixed design domain in Figs. 2.11(b) and 2.12(b) are divided into $m = 50$ layers with a layer thickness of 1 in the building direction. The elastic material has a Young's modulus of 75 GPa, and Poisson's ratio of 0.34. The applied traction $\boldsymbol{t}$ was set to 10 and the inherent strain component was set to the value in Eq. 2.13. The upper limit of the allowable volume was set to 50% of the volume of the fixed design domain. The parameter K in Eq. 1.17 was set to 0.8; the weighting parameter β in Eq. 2.17 was set to 5. The parameters w and d in Eq. 2.24 were set to 0.5 and 1×10^{-3}, respectively.

Figures 2.13-2.16 show the evaluated optimal configurations for each model. Figure 2.17 shows a plot of each objective function corresponding to the varying weighting coefficient. Furthermore, $\alpha = 0$ denotes that the objective function is only a compliance minimization problem. Additionally, the geometrical complexity of the optimal configuration changes depending on the value of the regularization parameter τ. As shown in Fig. 2.17, when the weighting coefficient α is large, the objective function that represents the part distortion in AM decreases, and the compliance increases. It can be seen that both numerical examples exhibit the same tendency, regardless of the regularization parameter, therefore, the designers can control the geometric complexity by adjusting τ first, followed by γ to control the compliance and part distortion. In other words, the part with the desired performance can be manufactured with high dimensional accuracy using AM. If the target

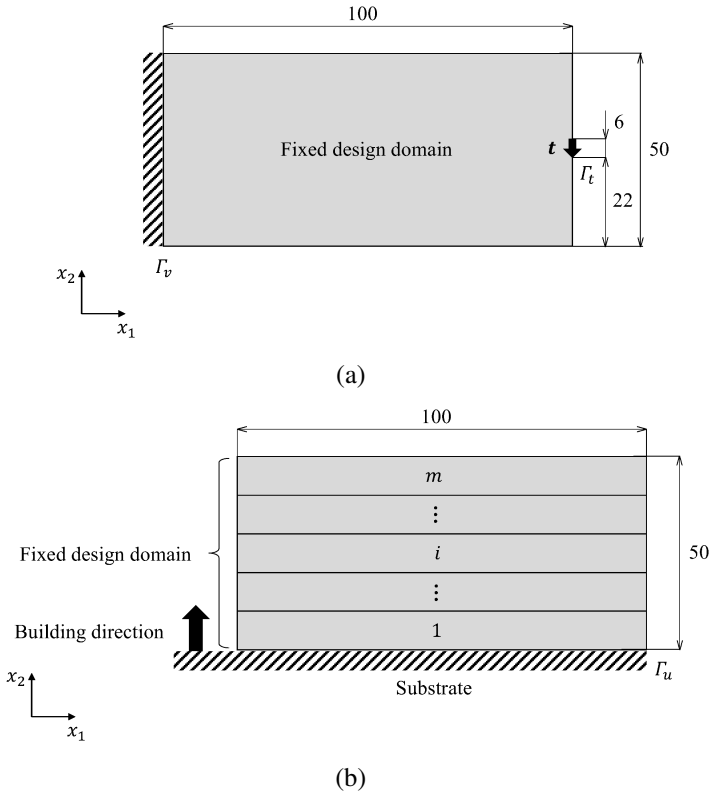

Fig. 2.11 Fixed design domain and boundary conditions for the cantilever model: (a) minimum mean compliance problem and (b) mechanics problem of AM.

distortion $\boldsymbol{u}_0$ is replaced with $\boldsymbol{u} = \boldsymbol{u} - \boldsymbol{u}_0$ in Eq. 2.14, then the part can be manufactured with arbitrary dimensional accuracy. Figure 2.18 shows the convergence history of the objective function and volume constraint for $\tau = 1 \times 10^{-4}$ and $\alpha = 0.1$ for each model. As the number of iterations increases, the objective function for the part distortion in AM decreases and compliance is maintained while satisfying the volume constraint. Figures 2.19 and 2.20 show the numerical results of the part distortion induced by AM for the final shape. The cantilever model has a protruding part outside the substrate where the distortion is large. As α increases, a structure appears in which the protrusions are fixed to the substrate to reduce the maximum displacement, and the displacement distribution becomes uniform. In addition, since the MBB beam model has a structure fixed to the substrate, the distortion is smaller than that of the cantilever model. Increasing α changes the optimal configuration to reduce the maximum displacement.

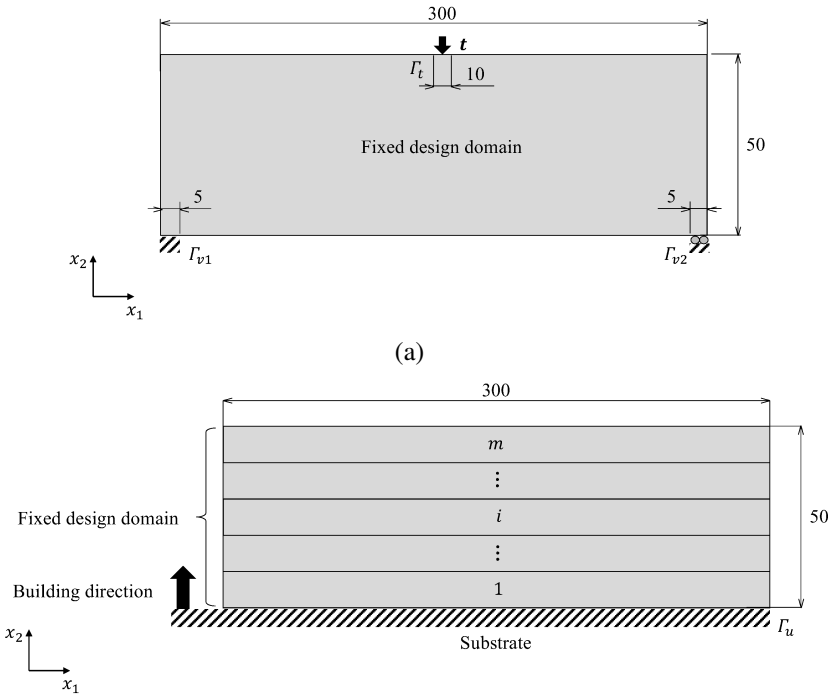

Fig. 2.12 Fixed design domain and boundary conditions for the Messerschmitt-Bolkow-Blohm (MBB) beam model: (a) minimum mean compliance problem and (b) mechanics problem of AM.

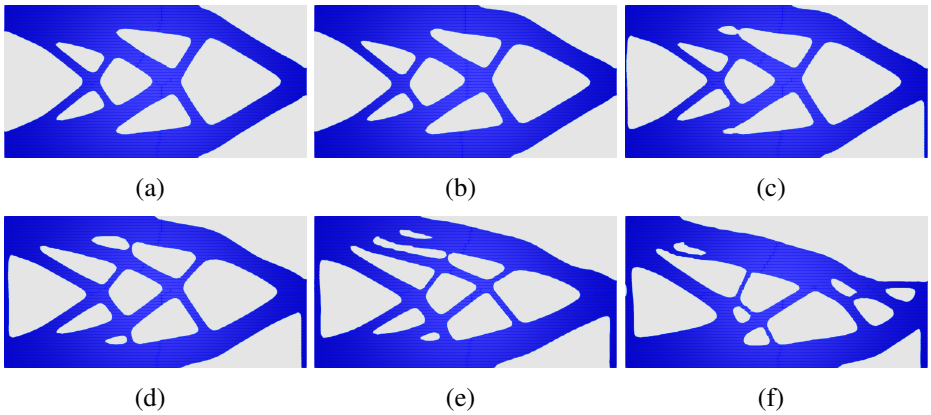

Fig. 2.13 Optimal configurations for the cantilever model $\tau = 1\times10^{-4}$: (a)$\alpha = 0$; (b)$\alpha = 0.03$; (c)$\alpha = 0.05$; (d)$\alpha = 0.10$; (e)$\alpha = 0.15$; (f)$\alpha = 0.20$.

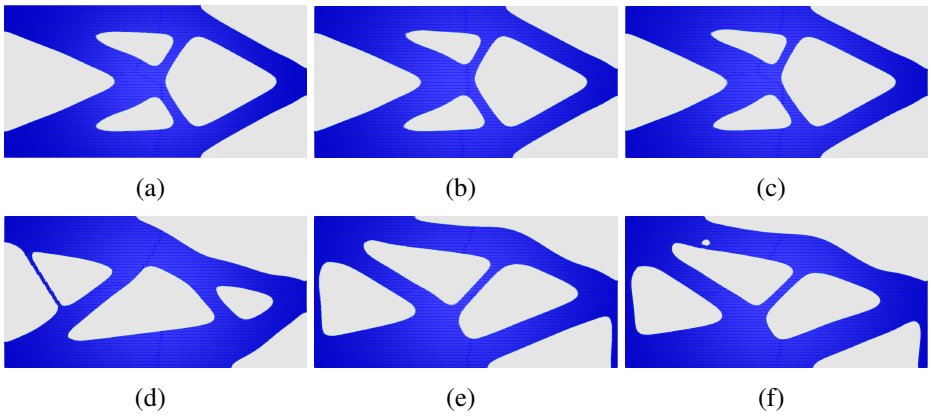

Fig. 2.14 Optimal configurations for the cantilever model $\tau = 1\times10^{-3}$: (a)$\alpha = 0$; (b)$\alpha = 0.03$; (c)$\alpha = 0.05$; (d)$\alpha = 0.10$; (e)$\alpha = 0.15$; (f)$\alpha = 0.20$.

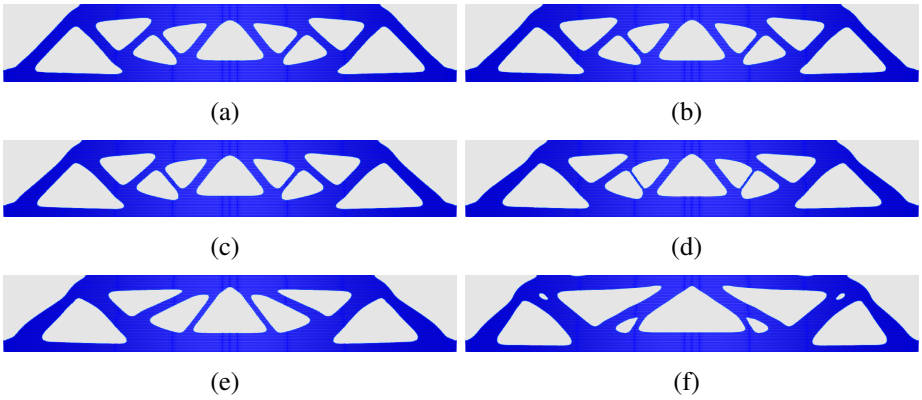

Fig. 2.15 Optimal configurations for the MBB beam model $\tau = 1\times10^{-4}$: (a)$\alpha = 0$; (b)$\alpha = 0.03$; (c)$\alpha = 0.05$; (d)$\alpha = 0.10$; (e)$\alpha = 0.15$; (f)$\alpha = 0.20$.

2.7.2 3D design examples

Next, based on the results obtained in the 2D design problems, we verify that it is also effective in the 3D design problem. The fixed design domain and boundary condition for minimum mean compliance problem is shown in Fig. 2.21. For the mechanics problem of AM, the z-direction was set as the building direction, and the fixed design domain is divided into $m = 100$ layers with a layer thickness of 1. Furthermore, the bottom of xy-plane was fixed. The upper limit of the allowable volume was set to 20% of the volume of the fixed design domain. The regularization parameter τ was set to 5×10^{-5}. The parameter α is set to 0 and 0.05 i.e., without and with considering part distortion, respectively. Figures

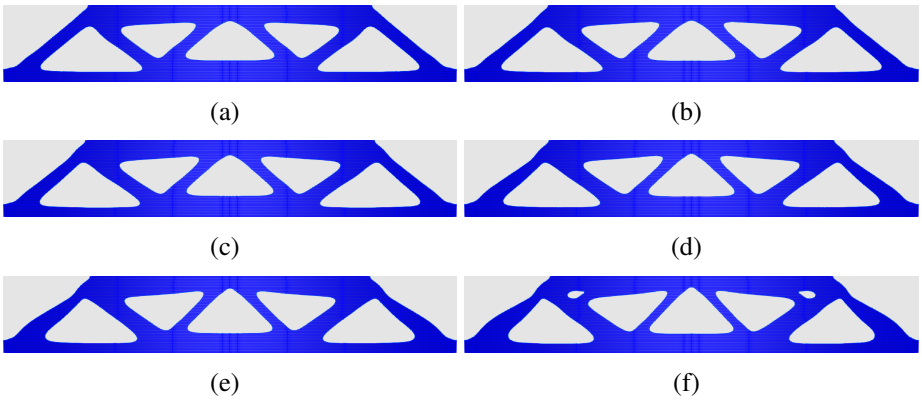

Fig. 2.16 Optimal configurations for the MBB beam model $\tau = 1 \times 10^{-3}$: (a)$\alpha = 0$; (b)$\alpha = 0.03$; (c)$\alpha = 0.05$; (d)$\alpha = 0.10$; (e)$\alpha = 0.15$; (f)$\alpha = 0.20$.

2.22 and 2.23 show the results of the optimal configuration and part distortion:(a) without considering part distortion, (b) with considering part distortion. Optimal configuration (a) has a large distortion in the overhanging region. Compared to that, the overhanging region in the optimal configuration (b) is fixed to the substrate, resulting in reduced distortion. This implies a reduced risk of manufacturing errors. The above 2D and 3D numerical examples prove that the proposed methodology is efficient in considering the part distortion in AM.

2.8 Summary

In this chapter, we proposed a topology optimization method that considers the part distortion in AM, using a computationally inexpensive analytical model. We achieved the following:

1. To predict the part-scale residual stress and distortion induced in the building process, the AM analytical model based on the inherent strain method and the identification method of the inherent strain component was proposed. The experimentally identified in-plane inherent strain components and building process algorithm in the analytical model have been demonstrated to effectively predict the part-scale residual stress and distortion, without using coupled or nonlinear analysis. The effect of the element size per layer in the analytical model on the accuracy and computational time was investigated, and the element size suitable for incorporation into topology optimization was proposed.

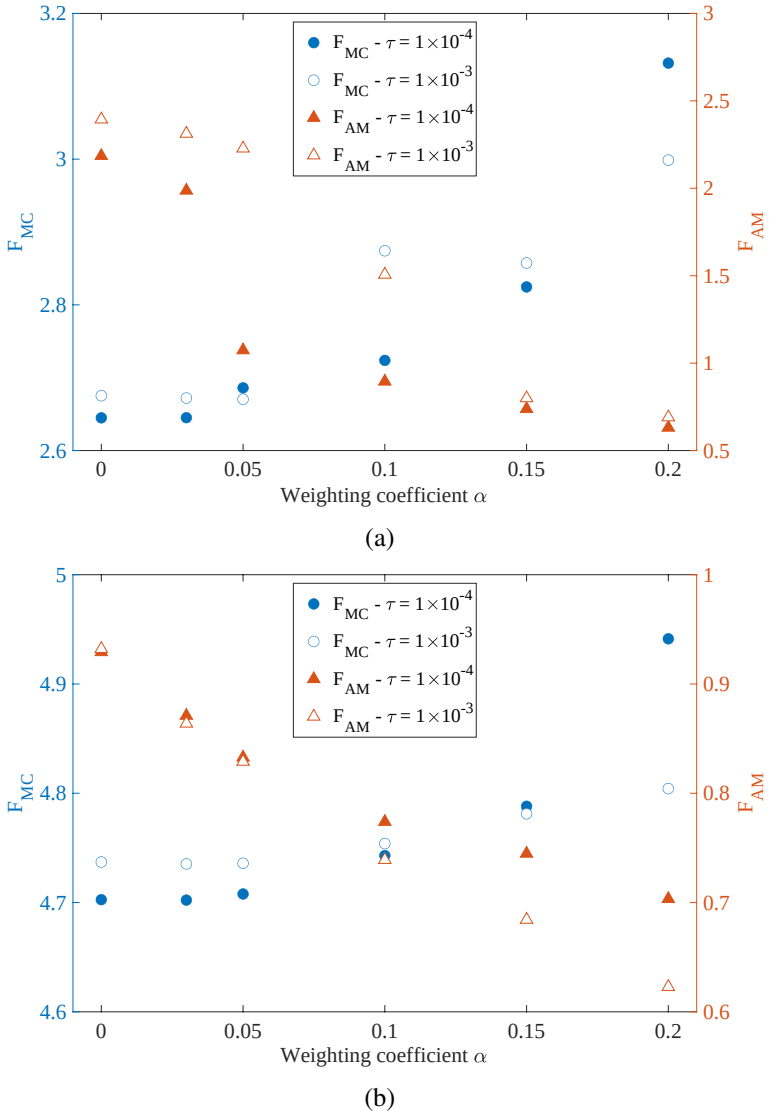

Fig. 2.17 Objective function with different weighting coefficient α: (a)cantilever model; (b)MBB beam model.

2. An objective function for reducing the part distortion in AM was proposed and a minimum mean compliance problem considering the part distortion was formulated. In the numerical implementation, an optimization algorithm was constructed and the non-dimensional sensitivity was used to enable simple adjustment of the weighting coefficient α.

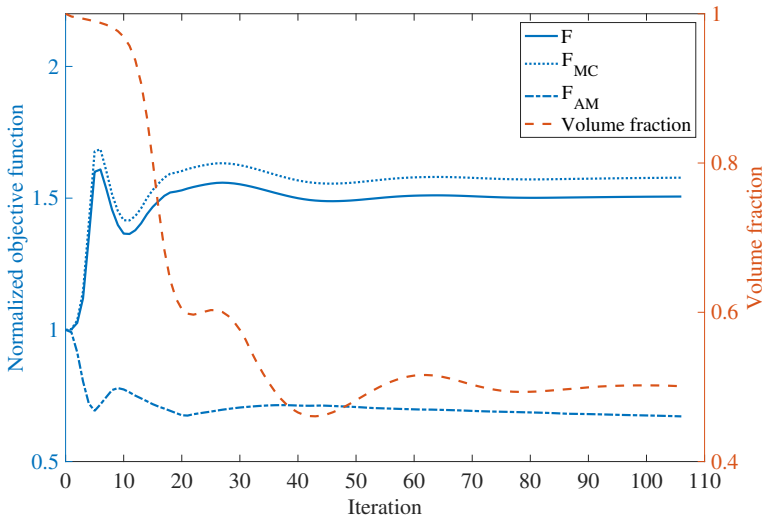

(a)

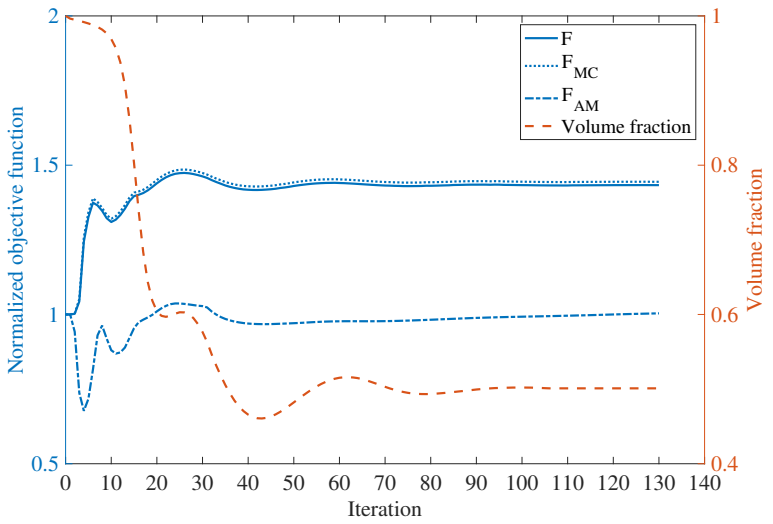

(b)

Fig. 2.18 Convergence history of the objective function and volume constraint for the case of $\alpha = 0.1$: (a)cantilever model; (b)MBB beam model.

3. In the minimum mean compliance problem, the proposed method provided an optimal configuration in which the compliance and part distortion in AM can be controlled by adjusting α appropriately.

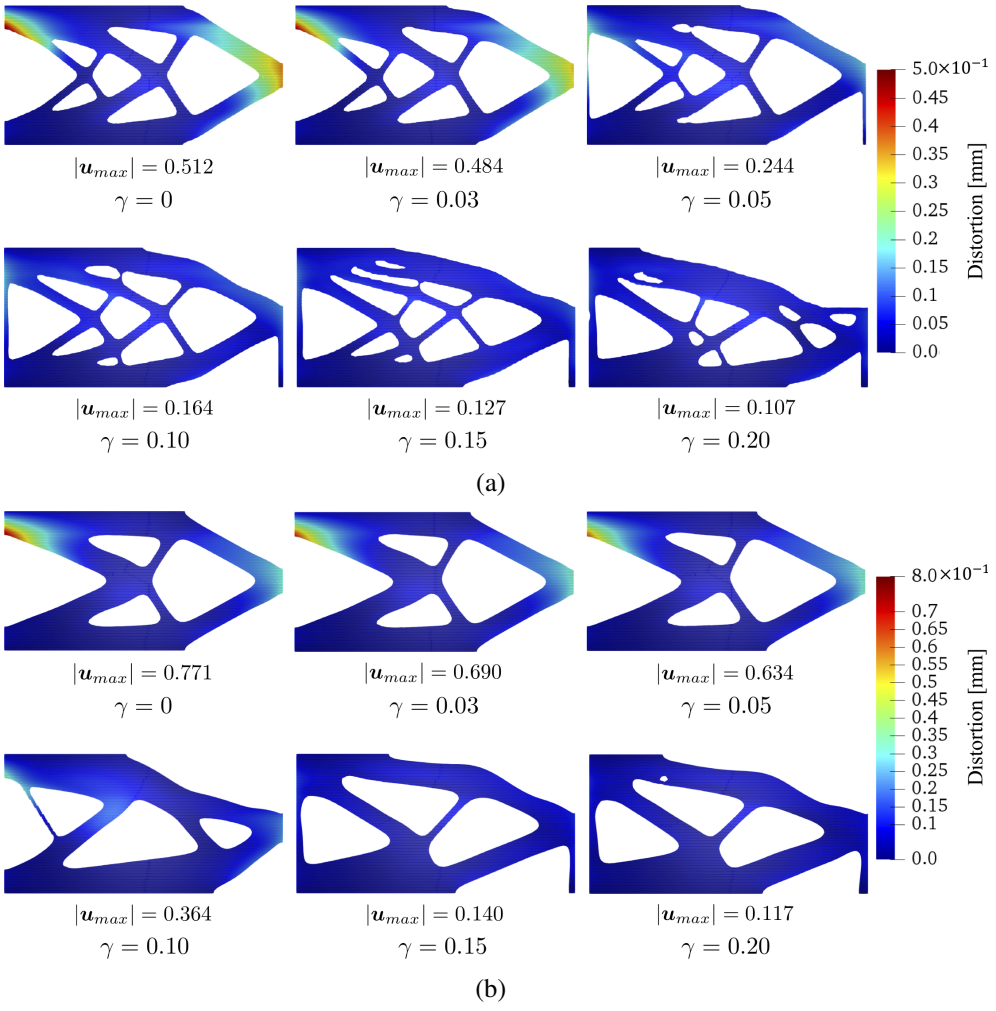

Fig. 2.19 Part distortion induced by the AM process for the cantilever model: (a)$\tau = 1\times10^{-4}$; (b)$\tau = 1\times10^{-3}$.

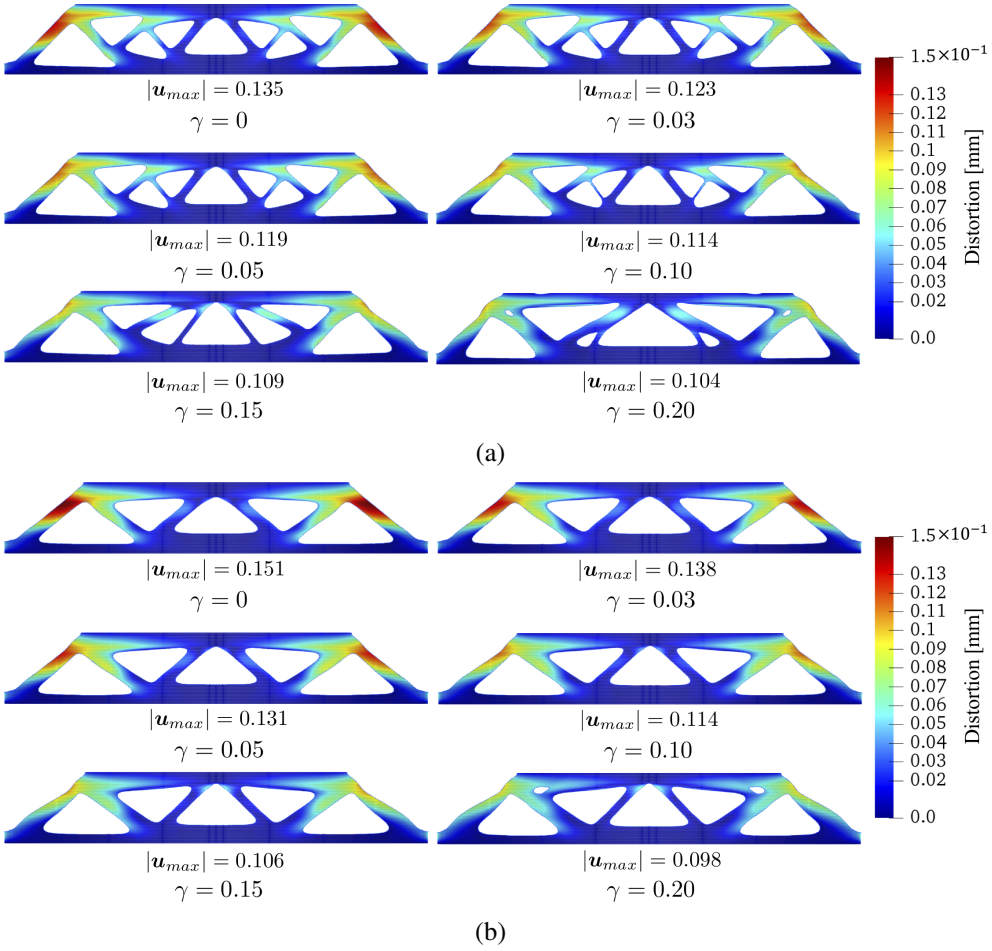

Fig. 2.20 Part distortion induced by the AM process for the MBB beam model: (a)$\tau = 1 \times 10^{-4}$; (b)$\tau = 1 \times 10^{-3}$.

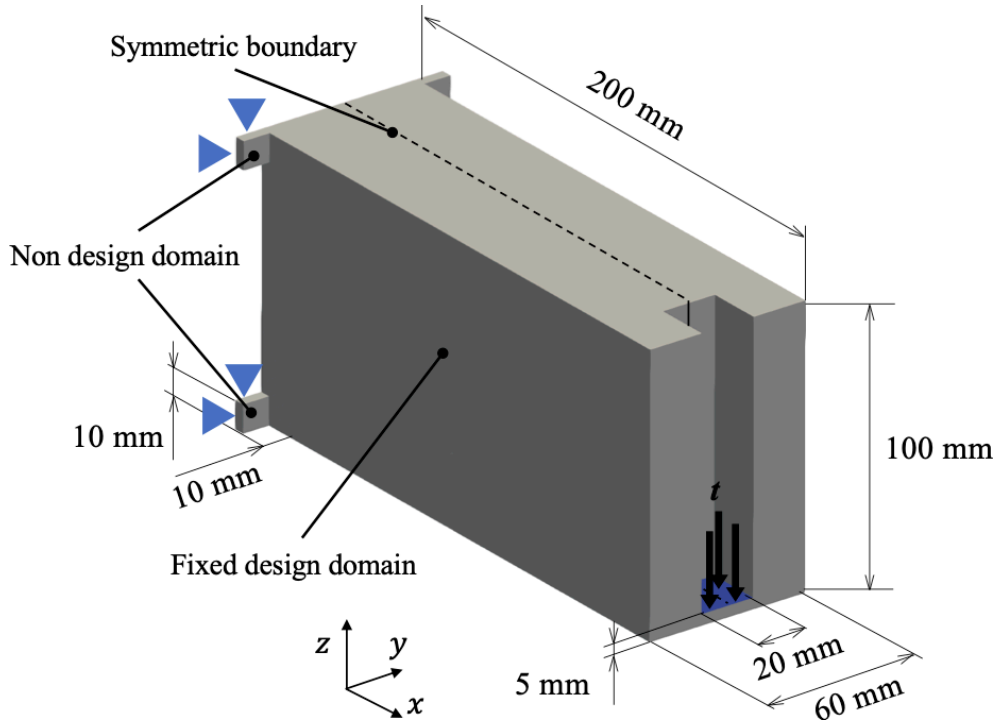

Fig. 2.21 Fixed design domain and boundary condition for the 3D model.

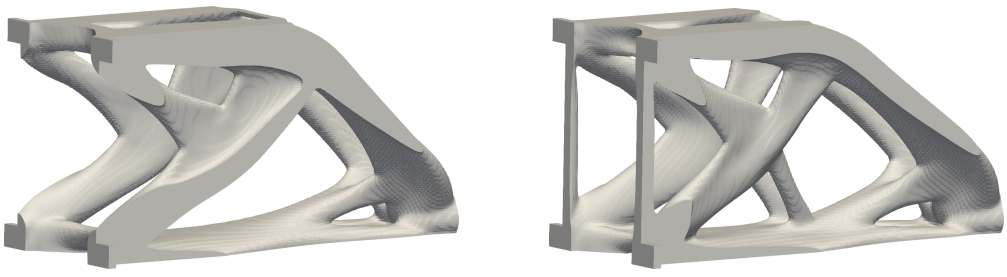

(a) (b)

Fig. 2.22 Optimal configurations for the 3D cantilever model: (a) without considering part distortion, (b) with considering part distortion.

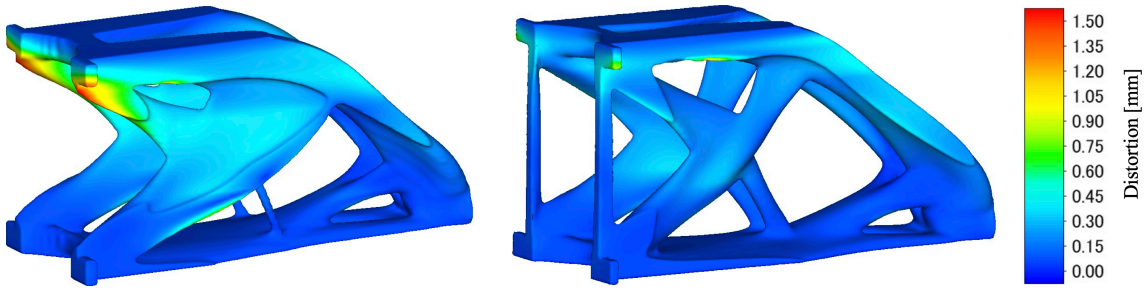

(a) without considering part distortion (b) with considering part distortion

Fig. 2.23 Part distortion induced by the AM process for the 3D cantilever model: (a) without considering part distortion, (b) with considering part distortion.

Chapter 3

Topology optimization of the support structure for heat dissipation in additive manufacturing

3.1 Introduction

The topology optimization considering distortion cannot handle overheating because it is formulated based on the inherent strain method, which has no thermal information. This chapter presents a thermal model for the LPBF process and proposes a topology optimization of the support structure that maximizes heat dissipation. Overheating is caused by excessive heat accumulation from the laser, leading to porosity defects and degrade surface quality [8, 16, 23]. To mitigate this thermal problem, it is necessary to improve the heat dissipation performance such that the heat effect of each layer is reduced by appropriately redesigning the parts or adding support structure. Furthermore, the support structure needs to be added to the part to avoid increasing the manufacturing time and cost because it will be removed after manufacturing.

Recently, several optimization methods with focus on improving heat dissipation have been proposed. Allaire et al.[3] proposed a stationary heat conduction analysis model in which a constant heat flux was applied to the shape boundary and constructed a level-set-based topology optimization that maximizes heat dissipation. Wang et al.[66] proposed a stationary heat conduction analysis model that provides heat flux only to overhanging surfaces and developed an optimization method that maximized heat dissipation on those

surfaces. The use of these analytical models is computationally inexpensive and suitable for combination with topology optimization. However, the validity of the analytical models was not rigorously confirmed because the heat source from the laser was applied to each layer in the actual building process, and the temperature distribution for each layer was not considered. Zhou et al.[74] proposed a transient heat conduction analysis model using a moving heat source representing a laser and constructed an optimization method that minimizes the temperature at selected points. Although this method can estimate the temperature distribution of each layer, the computational cost is high, and the point to minimize the temperature must be determined in advance.

In recent years, various modelling methods have been developed to predict part-scale residual stress and distortion in LPBF. These modelling methods can be summarized in three approaches [32, 9]: inherent strain, agglomerated laser, and flash heating. Computational cost and accuracy vary greatly depending on the these methods. The inherent strain [35, 58, 15, 43, 54] is a linear mechanical analysis in which the strain field is obtained through a calibration experiment or a part-scale thermo-mechanical analysis. Then, the strain field is applied to each build layer. This method is computationally inexpensive because it does not require nonlinear or coupled analyses. However, heat flow cannot be considered because there is no thermal information in the mechanical analysis. In contrast, the agglomerated laser and flash heating, which are based on thermo-mechanical analysis, have a temperature history. The agglomerated laser [33, 34, 17, 24, 32] is highly accurate because it takes into account the detailed build process parameters: powder layer thickness, laser spot size, laser power, laser scan speed, and total layer time. However, because typical runs employ more than 32 CPUs, the computational cost is high, and the model size that can be simulated is relatively small. The last category, flash heating [72, 49, 53, 41, 40, 71, 73, 9], is a simple modelling method that applies an equivalent volume heat flux to each scaled-up powder layer. Although scan strategies cannot be considered, residual stress and distortion can be predicted, including the temperature history. Furthermore, the effectiveness of this method has been experimentally verified.

In this chapter, we construct a support structure optimization method to maximize the heat dissipation for each build layer based on flash heating. Specifically, we focus on the thermal analysis part of flash heating and incorporate a process model that can predict the temperature field in the topology optimization. The remainder of this chapter is organized as follows. First, we propose a simple analytical model based on the transient heat conduction

problem to represent the temperature distribution in the AM building process. Next, we incorporate the proposed analytical model into a level-set-based topology optimization to formulate an optimization problem that maximizes the heat dissipation in each layer. We then construct an optimization algorithm for topology optimization using the finite element method (FEM). Lastly, we present 2D and 3D design examples to demonstrate the validity and effectiveness of the proposed optimization method.

3.2 Analytical model for LPBF process

3.2.1 Transient heat conduction under volume heat flux

The LPBF process repeats the heating and cooling cycles to melt and solidify the laminated powder material. Furthermore, because this material layer thickness is tens of micrometers, a part-scale analysis is computationally expensive. To address this, flash heating has been developed to simulate temperature transition by introducing meta-layers scaled up from the actual material layer and applying to each meta-layer a volume heat flux equivalent to laser irradiation [72, 49, 53, 41, 40, 71, 73, 9]. The meta-layer is usually 0.5-1.0 mm. In other words, scaling up to more than 10 times the actual layer improves computational efficiency with small changes in the computational output of thermal distortion and residual stress [72, 73, 9]. Based on the above method, we consider a build chamber Ω comprising the part Ω_c, the support structure Ω_s, powder Ω_p, and a build plate Ω_b, which represents the completed build state as shown in Fig.3.1. Here, to represent the intermediate state of the

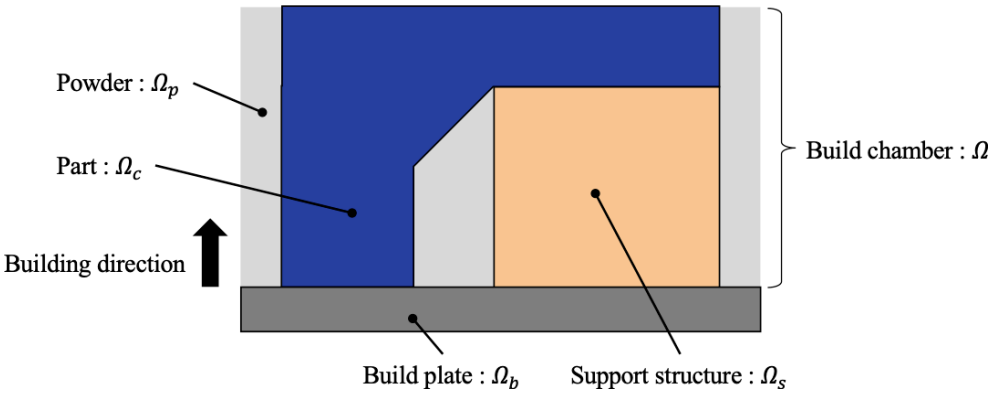

Fig. 3.1 Components of the build chamber in LPBF.

building process, the build chamber is divided into m layers with a fixed thickness in the

building direction, as shown in Fig. 3.2. The build chamber Ω is defined by each domain

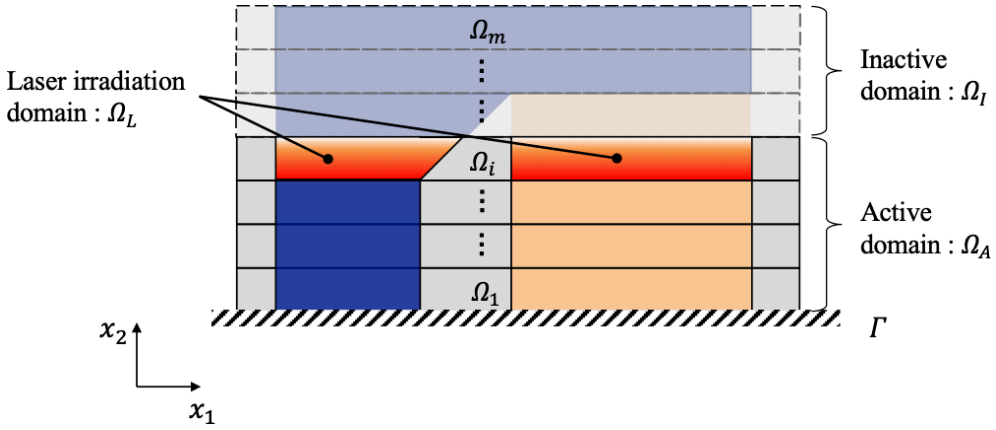

Fig. 3.2 Domains and boundary in the intermediate state of the building process.

Ω_i for $1 \leq i \leq m$ as follows:

$$\Omega = \Omega_1 \cup \ldots \cup \Omega_i \cup \ldots \cup \Omega_m. \tag{3.1}$$

Furthermore, we introduce three subdomains: the active domain Ω_A, inactive domain Ω_I, and laser irradiation domain Ω_L. The subdomain region depends on the domain number i, and each subdomain is defined as:

$$\Omega_A = \Omega_1 \cup \ldots \cup \Omega_i, \tag{3.2}$$

$$\Omega_I = \Omega \setminus \Omega_A, \tag{3.3}$$

$$\Omega_L = \Omega_i \setminus \Omega_p. \tag{3.4}$$

The subdomain is used to activate layers sequentially from the bottom and apply the volume heat flux to the activated layer, that is, the laser irradiation domain Ω_L. This allowed us to simulate the laser irradiation of each layer during the building process.

Because we focused on the heat flow of the parts after laser irradiation, the analysis model was simplified based on the following assumptions: First, the part Ω_c and the support structure Ω_s contained in the active domain Ω_A are filled with temperature-independent isotropic bulk materials. Second, because the thermal conductivity of the powder is significantly smaller than those of the part and the support structure, the powder region Ω_p is negligible [72, 35]. Furthermore, thermal energy loss owing to radiation and convec-

tion has also been neglected [57, 39, 59]. Therefore, heat energy is transferred to the build plate by heat conduction via part Ω_c and the support structure Ω_s within the active domain Ω_A. Third, the phase change from powder to solid and latent heat are ignored. In other words, the laser irradiation domain Ω_L uses the solid material properties during both heating and cooling processes. Fourth, the boundary Γ representing the build plate, which functions as a heat sink, is fixed at a constant temperature T_{amb} [52, 51, 74]. Based on the above assumptions, the transient heat conduction problem that predicts the temperature field $T_i(t, \boldsymbol{x}) : [0, t_h] \times \Omega_A \to \mathbb{R}$ in the heating process is governed by the following equation:

$$\begin{cases} \rho c \dfrac{\partial T_i(t, \boldsymbol{x})}{\partial t} - \operatorname{div}(k \nabla T_i(t, \boldsymbol{x})) = q(\boldsymbol{x}) & \text{in } (0, t_h) \times \Omega_A, \\ (k \nabla T_i(t, \boldsymbol{x})) \cdot n = 0 & \text{on } (0, t_h) \times \partial\Omega_A \setminus \Gamma, \\ T_i(t, \boldsymbol{x}) = T_{\text{amb}} & \text{on } (0, t_h) \times \Gamma, \\ T_i(0, \boldsymbol{x}) = T_{\text{amb}} & \text{in } \Omega_A, \end{cases} \tag{3.5}$$

for all indices $i = 1, 2, \ldots, m$, where $\boldsymbol{x}$ represents a point located in the active domain Ω_A, ρ is the density, c is the heat capacity, and k is the thermal conductivity. The volume heat flux $q(\boldsymbol{x})$ of the laser irradiation domain Ω_L is defined as follows:

$$q(\boldsymbol{x}) = \begin{cases} q & \text{for } \boldsymbol{x} \in \Omega_L, \\ 0 & \text{otherwise .} \end{cases} \tag{3.6}$$

Next, the transient heat conduction problem that predicts the temperature field $T_i(t, \boldsymbol{x}) : [0, t_c] \times \Omega_A \to \mathbb{R}$ in the cooling process is governed by the following equation:

$$\begin{cases} \rho c \dfrac{\partial T_i(t, \boldsymbol{x})}{\partial t} - \operatorname{div}(k \nabla T_i(t, \boldsymbol{x})) = 0 & \text{in } (0, t_c) \times \Omega_A, \\ (k \nabla T_i(t, \boldsymbol{x})) \cdot n = 0 & \text{on } (0, t_c) \times \partial\Omega_A \setminus \Gamma, \\ T_i(t, \boldsymbol{x}) = T_{\text{amb}} & \text{on } (0, t_c) \times \Gamma, \\ T_i(0, \boldsymbol{x}) = T_i(t_h, \boldsymbol{x}) & \text{in } \Omega_A, \end{cases} \tag{3.7}$$

for all indices $i = 1, 2, \ldots, m$. The next subsection describes an algorithm for predicting the temperature transition of the LPBF building process using the above governing equations.

3.2.2 LPBF building process model

There are two main strategies for activating the layers that represent the building process: the element birth method and the ersatz material approach. In this study, we apply the ersatz material approach that represents the inactive state by material properties that are 10^{-3} smaller than the part and support structure, and then represents the activated state by replacing the ersatz material with the original material properties.

Our LPBF building process algorithm is as follows:

Step1. Inactivate all layers in the chamber domain Ω divided into m layers.

Step2. The domains are activated in sequence from the bottom layer, and the volume heat flux is applied to the activated layer, that is, the laser irradiation domain Ω_L.

Step3. The temperature field $T_i(t, \boldsymbol{x})$, defined in Eq. 3.5 and 3.7 is solved using FEM.

Step4. If all layers are activated, the procedure is terminated; otherwise, it returns to the second step.

3.2.3 Numerical scheme for the governing equation

To solve the governing equation using the FEM, Eq. 3.5 discretized in space and time is given as follows:

$$\mathbf{C}\frac{\mathbf{T}_i^j - \mathbf{T}_i^{j-1}}{\Delta t^j} + \mathbf{K}\mathbf{T}_i^j = \mathbf{Q}^j, \tag{3.8}$$

where Δt^j is each time step ($j = 1 : n$), and $\mathbf{T}_i^j$ is the temperature vector. $\mathbf{C}$, $\mathbf{K}$, and $\mathbf{Q}^j$ are the heat capacity, conductivity matrices, and volume heat flux vector, respectively. These are defined using the shape function $\mathbf{N}$ and B-matrix $\mathbf{B}$ as follows:

$$\mathbf{C} = \int_\Omega \mathbf{N}^\mathsf{T} \rho_e c \mathbf{N} d\Omega, \tag{3.9}$$

$$\mathbf{K} = \int_\Omega \mathbf{B}^\mathsf{T} k_e \mathbf{B} d\Omega, \tag{3.10}$$

$$\mathbf{Q}^j = \int_{\Omega_L} q^j \mathbf{N} d\Omega. \tag{3.11}$$

ρ_e and k_e are the values that depend on the domain to which the discretized element e belongs and is defined as follows:

$$\rho_e = \begin{cases} \rho & \text{for } e \in \Omega_A, \\ 10^{-3}\rho & \text{for } e \in \Omega_I, \end{cases} \tag{3.12}$$

$$k_e = \begin{cases} k & \text{for } e \in \Omega_A, \\ 10^{-3}k & \text{for } e \in \Omega_I. \end{cases} \tag{3.13}$$

Furthermore, the cooling processes defined in Eq. 3.7 remove the volume heat flux vector $\mathbf{Q}^j$ from the above equation.

3.2.4 Numerical example for the analytical model

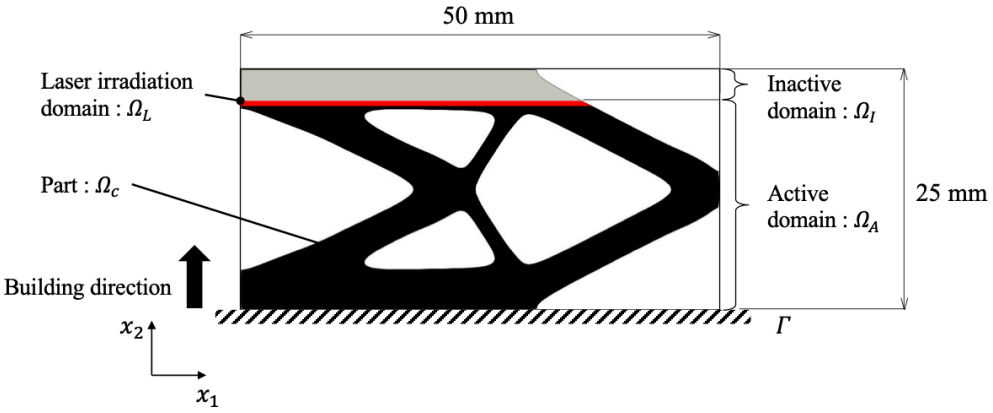

Fig. 3.3 Cantilever model and boundary conditions in the intermediate state of the LPBF building process.

This example uses the topology-optimized cantilever model [70], as shown in Fig. 3.3 to evaluate temperature transitions when building an overhanging region. The material properties and process parameters are listed in Tables 3.1 and 3.2. In this study, we do not focus on the temperature transition in the heating process, so that process is completed in one step. Then the cooling process begins. The time step of the cooling process was set to 1 s. This time step is employed to avoid increasing the computational cost when combined with topology optimization, which requires iterations. The model is divided in the building direction at 0.5 mm per layer. This is approximately 10 times the actual material layer. The effects of layer scaling were investigated by Zhang et al [73]. The model is discretized into a mesh of 19,834 second-order triangular elements.

Table 3.1 Material properties of AlSi10Mg[1]

Density ρ (kg/mm^3)	2.67×10^{-6}
Heat capacity c (J/kg K)	910
Thermal conductivity k (W/mm K)	119×10^{-3}

Table 3.2 Process parameters[41]

Volume heat flux q (W/mm^3)	2×10^{4}
Heating time per layer t_h (s)	0.5×10^{-3}
Cooling time per layer t_c (s)	10
Build plate temperature T_{amb}(°C)	20

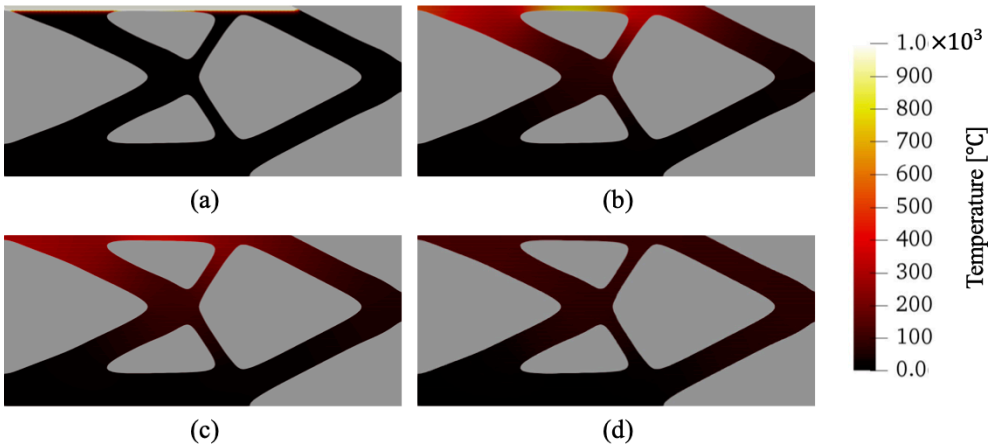

Fig. 3.4 Temperature transition of LPBF process: (a) end of the heating process t_h =0.5×10^{-3}; (b, c) intermediate time step of the cooling process t_c =1 s and 2 s; (d) end of the cooling process t_c =10 s.

Figure 3.4 shows the temperature fields at four different time steps in the active domain Ω_A. During the heating process, only the added layer is heated, and almost no heat flows to the lower layer. In the cooling process, heat energy flows to the lower layer, but if there is a region that blocks the heat flow, such as an overhang, it results in a non-uniform temperature distribution. The temperature histories of the overhang and non-overhang regions are compared in Fig. 3.5. This result shows that a poor heat dissipation leads to a non-uniform temperature distribution in the cooling process. Furthermore, after t_c =4 s of the cooling process, the cooling rate suddenly decreases and the temperature distribution becomes uniform. Therefore, it is necessary to dissipate heat so that the temperature distribution in the added layer becomes uniform within t_c =3 s of the cooling process. Next, Figure 3.6 shows the result of summing the temperature fields of each laser irradiation domain Ω_L in

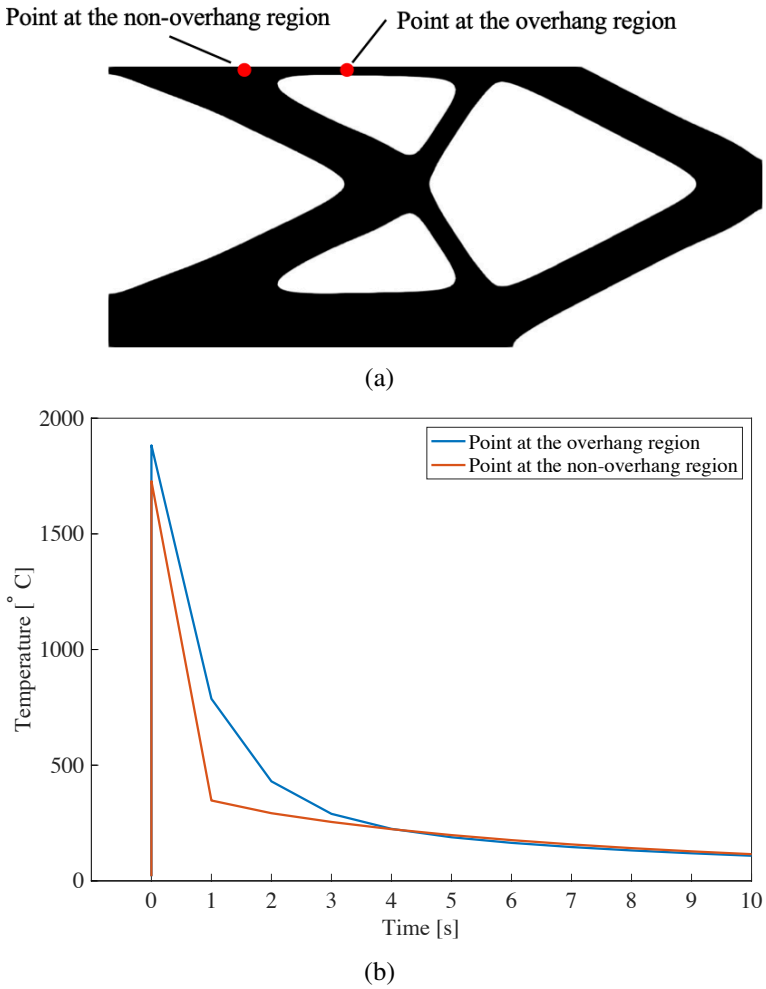

Fig. 3.5 Comparison of temperature histories in the overhang region and the non-overhang region: (a) Point locations for plotting temperature history (b)Temperature history at each point.

the cooling process t_c =1 s. This result also shows that the overhang region has the most non-uniform temperature distribution. Therefore, the support structure must be added at the appropriate location in the void region (the powder Ω_p), excluding the parts Ω_c to improve heat dissipation at each layer. In the following sections, we formulate the support structure optimization problem that maximizes the heat dissipation.

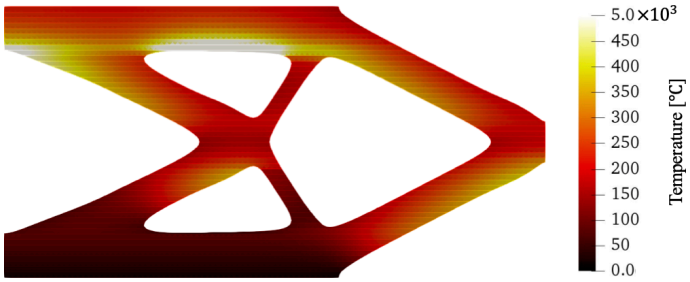

Fig. 3.6 Temperature field of each laser irradiation domain Ω_L in the cooling process t_c =1 s.

3.3 Topology optimization for heat dissipation in LPBF

3.3.1 Formulation of optimization problem

In this study, the objective function F minimizes the squared error between the temperature of the part Ω_c contained in each laser irradiation domain Ω_L and the build plate temperature $\mathbf{T}_{amb}$, which corresponds to maximizing heat dissipation, which corresponds to maximizing heat dissipation during the cooling process.

$$F = \sum_{i=1}^{m}\sum_{j=1}^{n}\left(\mathbf{T}_i^j - \mathbf{T}_{amb}\right)^2 \Delta t^j \quad \text{for } e \in \Omega_c \cap \Omega_L, \tag{3.14}$$

Thus, the optimization problem for determining the optimal configuration of the support structure Ω_s to maximize the heat dissipation of part Ω_c under volume constraints can be formulated as follows:

$$\begin{aligned} &\inf_{\boldsymbol{\Phi}} && F, \\ &\text{subject to :} && G = \int_{\Omega\setminus\Omega_c} \chi \, d\Omega - V_{\max} \leq 0, \\ & && \mathbf{R}_i^j = \mathbf{C}\frac{\mathbf{T}_i^j - \mathbf{T}_i^{j-1}}{\Delta t^j} + \mathbf{K}\mathbf{T}_i^j = \mathbf{0}, \end{aligned} \tag{3.15}$$

for all indices $j = 1, 2, \ldots, n$, and $i = 1, 2, \ldots, m$. Here, G represents the volume constraint, and V_{max} is the upper limit of the material volume in the chamber, excluding the part $\Omega \setminus \Omega_c$. $\mathbf{R}_i^j$ represents the governing equation in the cooling process.

3.3.2 Sensitivity analysis

The sensitivity of the objective function F in Eq. 3.14 is derived using the adjoint variable method. First, by introducing an adjoint variable $\boldsymbol{\lambda}_i^j$ into the governing equation, the extended objective function $\tilde{F}$ can be written as

$$\tilde{F} = F + \sum_{i=1}^{m}\sum_{j=1}^{n} \boldsymbol{\lambda}_i^{j\mathsf{T}} \mathbf{R}_i^j. \tag{3.16}$$

Next, the above extended objective function is differentiated by the design variable $\boldsymbol{\Phi}$.

$$\begin{aligned}\frac{\partial \tilde{F}}{\partial \boldsymbol{\Phi}} =& \frac{\partial F}{\partial \boldsymbol{\Phi}} + \sum_{i=1}^{m}\sum_{j=1}^{n} \frac{\partial F}{\partial \mathbf{T}_i^j}\frac{\partial \mathbf{T}_i^j}{\partial \boldsymbol{\Phi}} \\ &+ \sum_{i=1}^{m}\sum_{j=1}^{n} \boldsymbol{\lambda}_i^{j\mathsf{T}} \left(\frac{\partial \mathbf{R}_i^j}{\partial \boldsymbol{\Phi}} + \frac{\partial \mathbf{R}_i^j}{\partial \mathbf{T}_i^j}\frac{\partial \mathbf{T}_i^j}{\partial \boldsymbol{\Phi}} + \frac{\partial \mathbf{R}_i^j}{\partial \mathbf{T}_i^{j-1}}\frac{\partial \mathbf{T}_i^{j-1}}{\partial \boldsymbol{\Phi}} \right).\end{aligned} \tag{3.17}$$

The above equation can be rearranged as follows:

$$\begin{aligned}\frac{\partial \tilde{F}}{\partial \boldsymbol{\Phi}} =& \frac{\partial F}{\partial \boldsymbol{\Phi}} + \sum_{i=1}^{m}\sum_{j=1}^{n} \boldsymbol{\lambda}_i^{j\mathsf{T}} \frac{\partial \mathbf{R}_i^j}{\partial \boldsymbol{\Phi}} + \sum_{i=1}^{m} \left(\frac{\partial F}{\partial \mathbf{T}_i^n} + \boldsymbol{\lambda}_i^{n\mathsf{T}} \frac{\partial \mathbf{R}_i^n}{\partial \mathbf{T}_i^n} \right) \frac{\partial \mathbf{T}_i^n}{\partial \boldsymbol{\Phi}} \\ &+ \sum_{i=1}^{m}\sum_{j=1}^{n-1} \left(\frac{\partial F}{\partial \mathbf{T}_i^j} + \boldsymbol{\lambda}_i^{j\mathsf{T}} \frac{\partial \mathbf{R}_i^j}{\partial \mathbf{T}_i^j} + \boldsymbol{\lambda}_i^{j+1\mathsf{T}} \frac{\partial \mathbf{R}_i^{j+1}}{\partial \mathbf{T}_i^j} \right) \frac{\partial \mathbf{T}_i^j}{\partial \boldsymbol{\Phi}}.\end{aligned} \tag{3.18}$$

From the above, the adjoint equation in the time step n is described as

$$\frac{\partial F}{\partial \mathbf{T}_i^n} + \boldsymbol{\lambda}_i^{n\mathsf{T}} \frac{\partial \mathbf{R}_i^n}{\partial \mathbf{T}_i^n} = \mathbf{0}. \tag{3.19}$$

The adjoint variable $\boldsymbol{\lambda}_i^n$ can be obtained from the transient heat equation in Eq. 3.7 at the time step n. Furthermore, the adjoint equation of the time step $1 \leq j \leq n-1$ is described as follows:

$$\frac{\partial F}{\partial \mathbf{T}_i^j} + \boldsymbol{\lambda}_i^{j\mathsf{T}} \frac{\partial \mathbf{R}_i^j}{\partial \mathbf{T}_i^j} + \boldsymbol{\lambda}_i^{j+1\mathsf{T}} \frac{\partial \mathbf{R}_i^{j+1}}{\partial \mathbf{T}_i^j} = \mathbf{0}, \tag{3.20}$$

where $\frac{\partial F}{\partial \mathbf{T}_i^j}$, $\frac{\partial \mathbf{R}_i^j}{\partial \mathbf{T}_i^j}$ and $\frac{\partial \mathbf{R}_i^{j+1}}{\partial \mathbf{T}_i^j}$ are calculated as follows:

$$\frac{\partial F}{\partial \mathbf{T}_i^j} = 2\left(\mathbf{T}_i^j - \mathbf{T}_{amb}\right)\Delta t^j \tag{3.21}$$

$$\frac{\partial \mathbf{R}_i^j}{\partial \mathbf{T}_i^j} = \frac{1}{\Delta t^j}\mathbf{C} + \mathbf{K}, \tag{3.22}$$

$$\frac{\partial \mathbf{R}_i^{j+1}}{\partial \mathbf{T}_i^j} = -\frac{1}{\Delta t^j}\mathbf{C}. \tag{3.23}$$

The adjoint variable of time step $1 \leq j \leq n-1$ can be obtained by solving the above equation in the backward direction with $\boldsymbol{\lambda}_i^n$ as the initial condition. By substituting the adjoint variables obtained from Eqs. 3.19 and 3.20, the sensitivity of the objective function can be described as follows:

$$\frac{\partial \tilde{F}}{\partial \boldsymbol{\Phi}} = \frac{\partial F}{\partial \boldsymbol{\Phi}} + \sum_{i=1}^{m}\sum_{j=1}^{n} \boldsymbol{\lambda}_i^{j\mathsf{T}} \frac{\partial \mathbf{R}_i^j}{\partial \boldsymbol{\Phi}}, \tag{3.24}$$

where $\frac{\partial \mathbf{R}_i^j}{\partial \boldsymbol{\Phi}}$ is calculated as:

$$\frac{\partial \mathbf{R}_i^j}{\partial \boldsymbol{\Phi}} = \left(\frac{1}{\Delta t^j}\frac{\partial \mathbf{C}}{\partial \boldsymbol{\Phi}} + \frac{\partial \mathbf{K}}{\partial \boldsymbol{\Phi}}\right)\mathbf{T}_i^j - \left(\frac{1}{\Delta t^j}\frac{\partial \mathbf{C}}{\partial \boldsymbol{\Phi}}\right)\mathbf{T}_i^{j-1}. \tag{3.25}$$

Furthermore, because the objective function does not depend on the design variable, it becomes:

$$\frac{\partial F}{\partial \boldsymbol{\Phi}} = \mathbf{0}. \tag{3.26}$$

Because the volume heat flux is applied to the support structure contained in the laser irradiation domain Ω_L, it does not contribute to heat dissipation. Therefore, the laser irradiation domain Ω_L is not included in the design sensitivity.

3.4 Numerical implementation

3.4.1 Optimization algorithm

The optimization algorithm is as follows.

Step1. The initial value of the level-set function was set.

Step2. The temperature field $\mathbf{T}_i^j$ defined in Eqs. 3.5 and 3.7 is solved according to the LPBF building process algorithm.

Step3. The objective function F, defined in Eq. 3.14 is evaluated using the solution of the transient heat conduction problem.

Step4. If the change ratio of the objective function is less than 0.01% in 5 consecutive iterations and the volume constraint is satisfied, it is assumed that convergence is established and the optimization procedure is terminated; otherwise, the adjoint variables $\boldsymbol{\lambda}_i^j$ defined in Eqs. 3.19 and 3.20 are solved using FEM, and the sensitivity of the objective function F is calculated using Eq. 3.24.

Step5. The level-set function is updated using Eq. 1.17 based on sensitivity; then the procedure returns to the second step.

3.4.2 Regularization of the boundary between the two domains

In the FEM analysis, generating a mesh along the boundary between the material and void domains for each optimization iteration increases the computational cost. In this study, the boundary is expressed by approximating the characteristic function [6] without generating a mesh. We assume that the void domain has smaller material properties than the material domain, and the material properties at the boundary change smoothly. Each material property ρ and k in the active domain Ω_A uses the extended material properties expressed by the following equations:

$$\tilde{\rho}(\phi; w) = \{(1-d)H(\phi; w) + d\}\,\rho, \tag{3.27}$$

$$\tilde{k}(\phi; w) = \{(1-d)H(\phi; w) + d\}\,k, \tag{3.28}$$

where $H(\phi; w)$ is defined as:

$$H(\phi; w) := \begin{cases} 1 & \text{for } \phi > w, \\ \frac{1}{2} + \frac{\phi}{w}\left(\frac{15}{16} - \frac{\phi^2}{w^2}\left(\frac{5}{8} - \frac{3}{16}\frac{\phi^2}{w^2}\right)\right) & \text{for } -w \le \phi \le w, \\ 0 & \text{for } \phi < -w, \end{cases} \tag{3.29}$$

where w represents the width of the transition and d is the coefficient of the material properties for the void domains.

3.5 Numerical examples for the support optimization

This section demonstrates the effectiveness and validity of the proposed optimization method for the support structure to maximize heat dissipation through 2D and 3D numerical examples.

3.5.1 Benchmark design examples

We consider the optimal support structure using the optimized 2D cantilever, MBB beam, and 3D L-bracket models, as shown in Fig. 3.7 as the part Ωc. Black and gray represent the non-design and fixed design domains, respectively. Both build chambers are divided into $m = 50$ layers with a layer thickness of 0.5 mm in the building direction. The meshes of the cantilever and MBB beam models comprised 43,584 and 64,310 second-order triangular elements, respectively. The L-bracket model was discretized into a mesh of 1,413,753 second-order tetrahedral elements. From the result of Subsection 3.2.4, the time step n was set to 3 ($j = 1 : 3$) in Eq. 3.14. The material properties of the part and support structure as well as the boundary conditions are listed in Tables 3.1 and 3.2. In order to have the volume the same as that of conventional support structure to compared to later, the upper limit of the material volume was set to 21% for the cantilever model, 17.4% for the MBB beam model, and 20% for the L-bracket model. The regularization parameter τ was set to 1×10^{-4}. The parameter D in Eq. 1.17 was set to 0.8, and the parameters w and d in Eq. 3.29 were set to 0.9 and 1×10^{-3}, respectively.

Figure 3.8 shows the optimal configurations for each model. In all the results, it can be seen that the support structure is added to the overhang region, where the heat dissipation is poor. Figure 3.9 shows the convergence history of the objective function and volume constraint for each model, Figure 3.10 shows the Initial , intermediate, and optimal configuration of the cantilever model representing each model. As the number of iterations increases, the objective function decreases while satisfying the volume constraint. The computational time until convergence was 4 h for the cantilever model, 2.5 h for the MBB beam model, and 34 h for the L-bracket model. The calculations of the 2D models were run on 14 Intel Xeon E5-2687W cores, and the 3D model was run on 28 Intel Xeon E5-2687W cores.

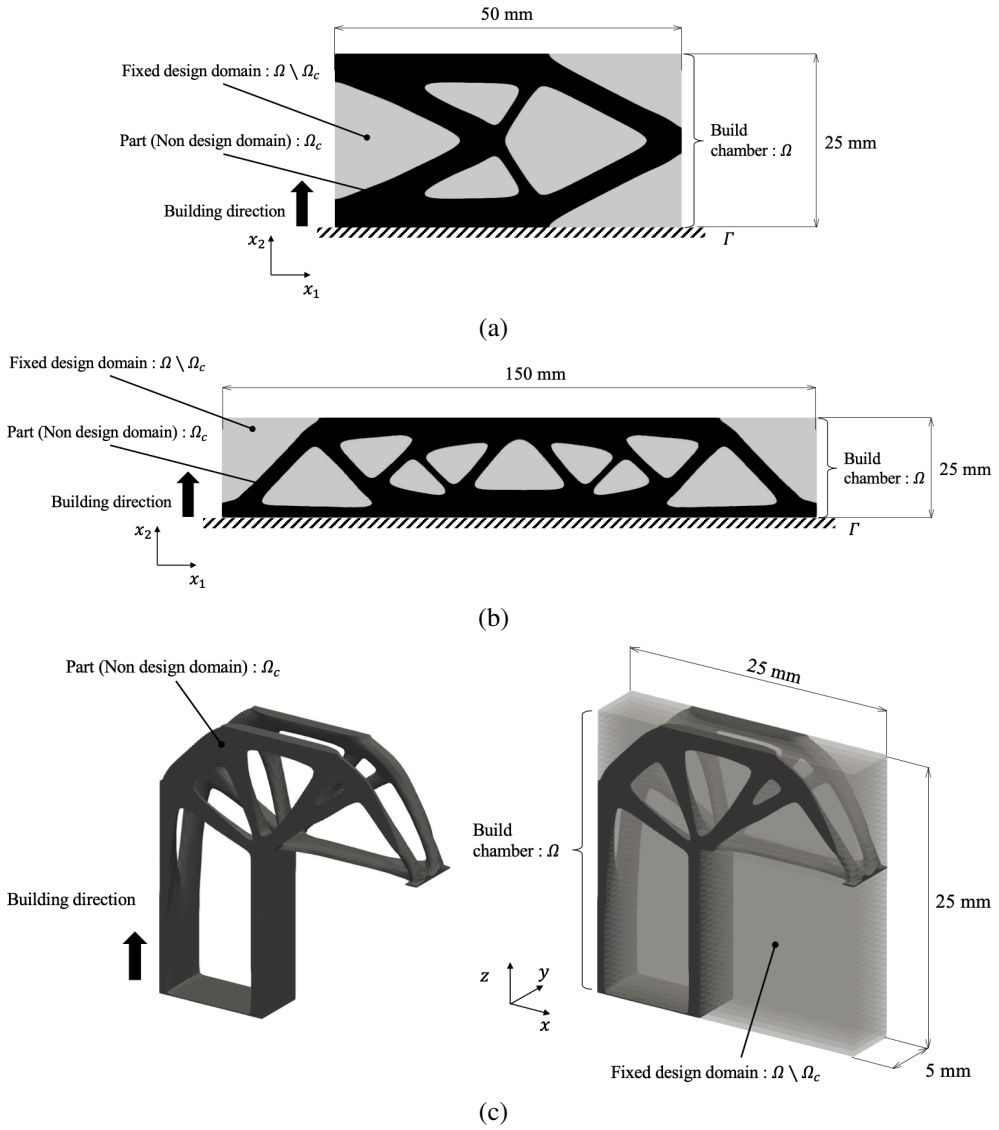

Fig. 3.7 Problem setting: (a)cantilever model; (b)MBB beam model; (c) L-bracket model.

3.5.2 Comparison with conventional support structure

This subsection examines the effectiveness and validity of the optimized support structure. Specifically, we compare the optimized support with the traditional support for three items: the temperature field when building the overhang region, the sum of the temperature fields of each laser irradiation domain Ω_L, and the objective function. Figure 3.11 shows the temperature field in the cooling process t_c =1 s when building the overhang region. Each optimized support demonstrates that the maximam temperature difference is smaller than

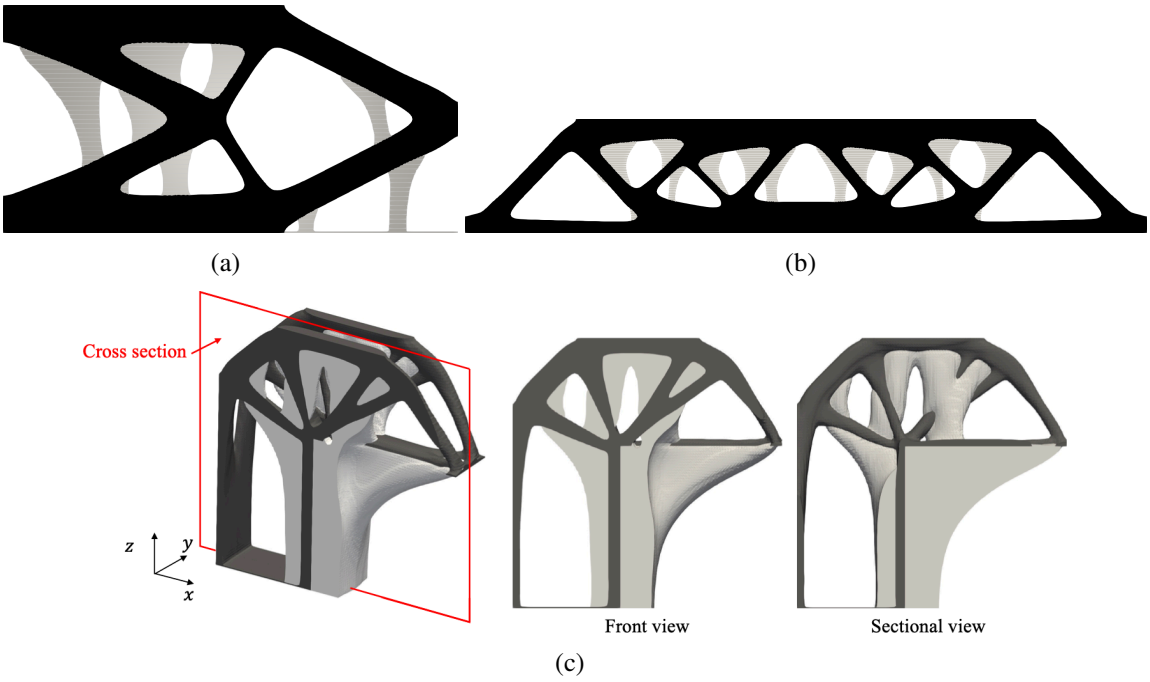

Fig. 3.8 Optimal configurations: (a)cantilever model; (b)MBB beam model; (c) L-bracket model.

in conventional ones. Furthermore, it is observed that the maximum temperature difference in the laser irradiation domain has also been reduced. Figure 3.12 displays the temperature fields of each laser irradiation domain Ω_L in the cooling process t_c =1 s and the objective function. It is observed that each optimized support has a more uniform temperature distribution in each laser irradiation domain than that of the conventional support, resulting in a smaller objective function. In other words, the proposed methodology is promising for reducing thermal distortion, avoiding microstructure inhomogeneity, and degrading surface quality compared to conventional support structures. The above results demonstrate the effectiveness of the proposed methodology for maximizing the heat dissipation in the LPBF process. However, in the L-bracket model, the support structure has a non-uniform temperature distribution because of the overhang region. In some cases, the support structure also needs to be included in the objective function to improve its own heat dissipation.

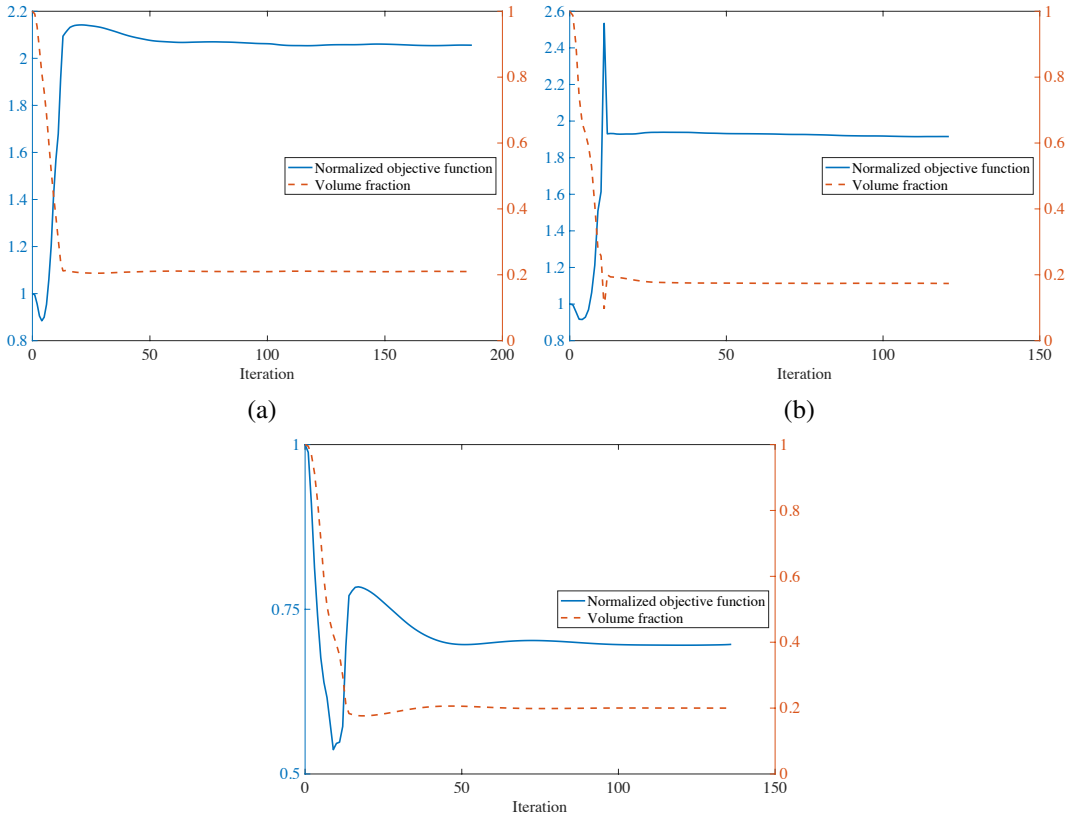

Fig. 3.9 Convergence history of the objective function and volume constraint: (a)cantilever model; (b)MBB beam model; (c)L-bracket model.

Fig. 3.10 Initial configuration, intermediate results and optimal configuration of cantilever model.

3.6 Summary

In this chapter, we proposed a topology optimization method for a support structure that maximizes the heat dissipation in the LPBF process. We achieved the following:

1. An algorithm that simulates the LPBF building process was constructed based on the transient heat conduction problem with volume heat flux. Through the numerical

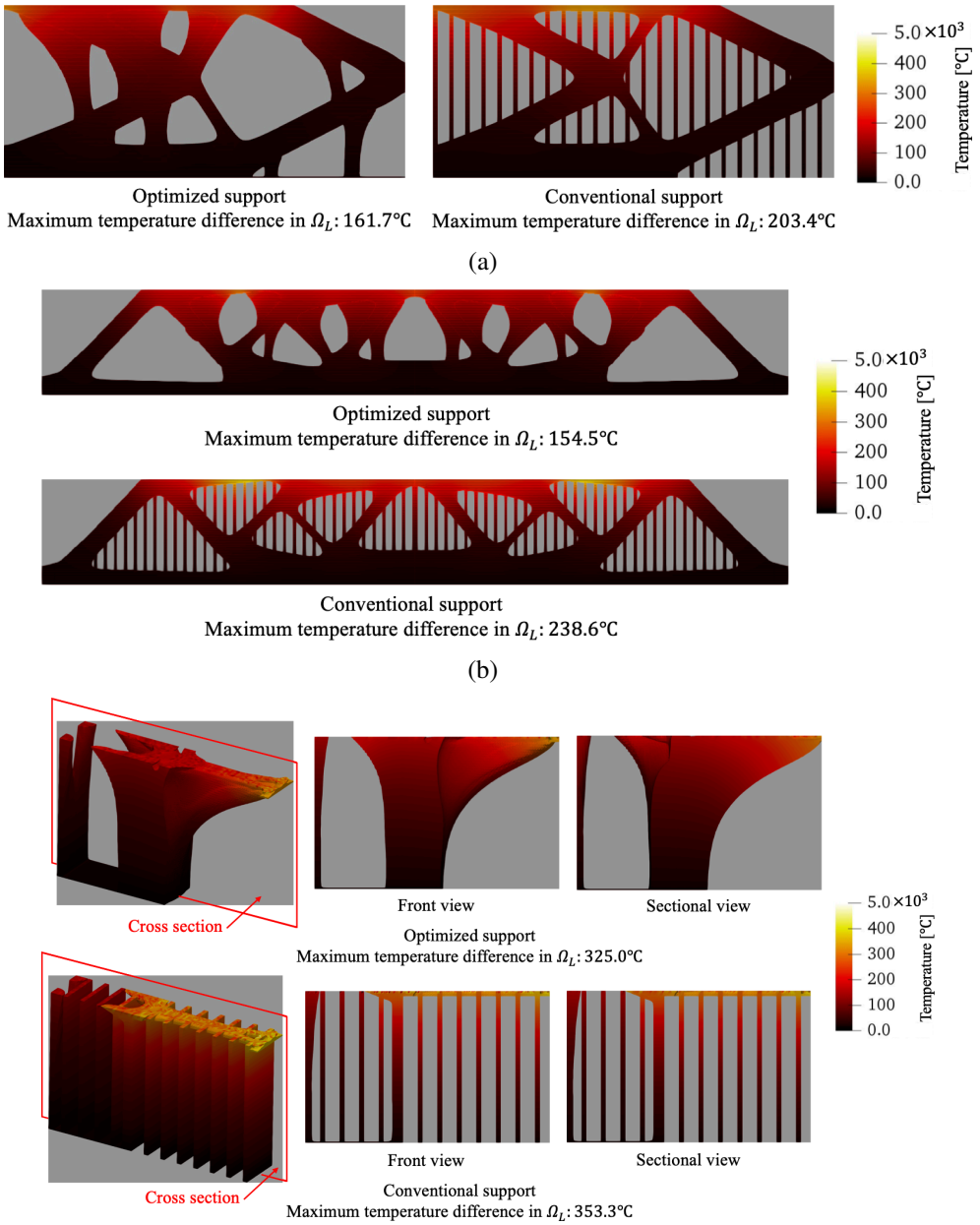

Fig. 3.11 Temperature field in the cooling process t_c =1 s when building the overhang region: (a)cantilever model; (b)MBB beam model; (c)L-bracket model.

example, it was shown that the difference in heat dissipation in the laser irradiation domain appeared during the cooling process, and the overhang region had poor heat dissipation.

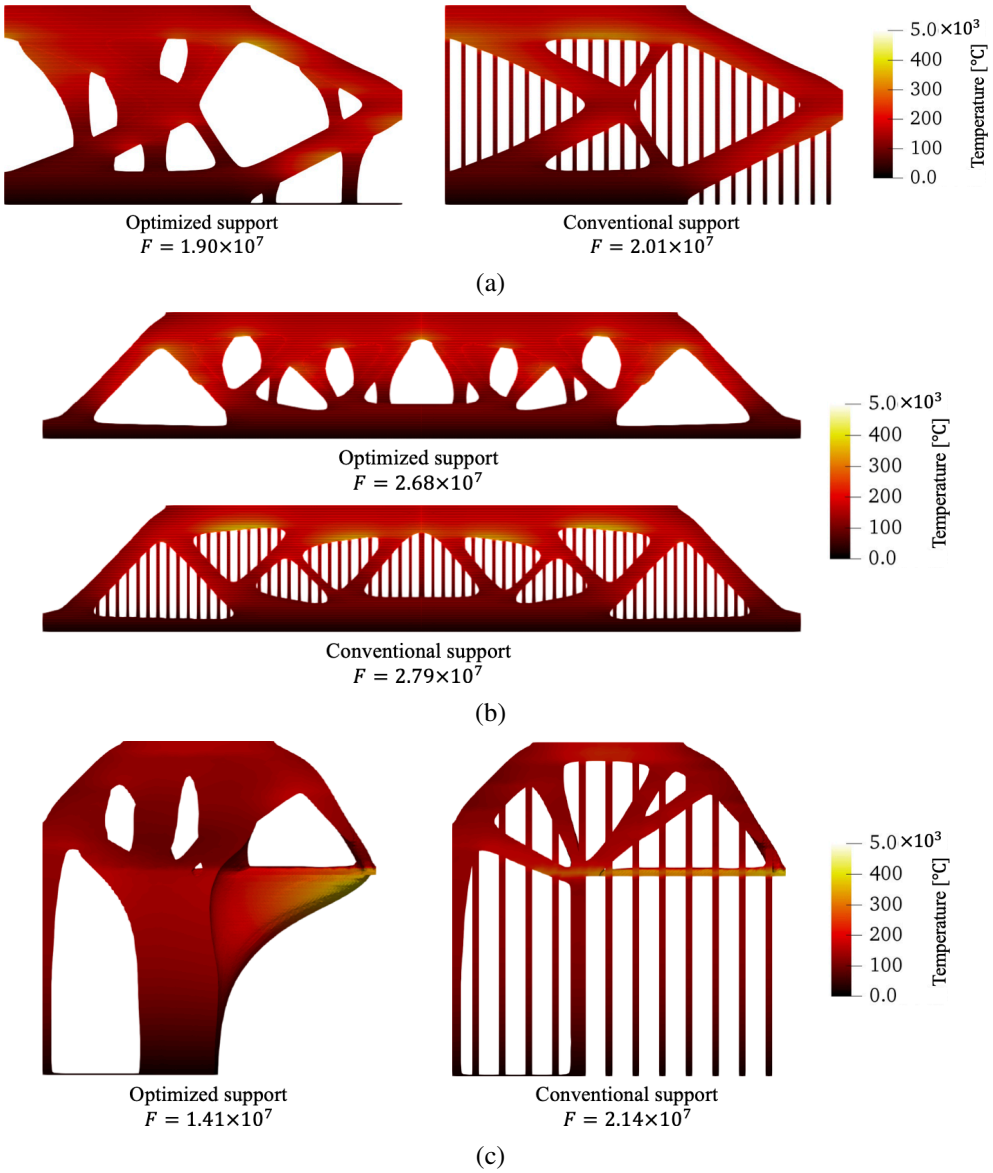

Fig. 3.12 Temperature field of each laser irradiation domain Ω_L in the cooling process t_c =1 s: (a)cantilever model; (b)MBB beam model; (c)L-bracket model.

2. An objective function for the support structure that maximizes heat dissipation of the part was proposed, then the optimization problem was formulated. The sensitivity of the objective function was derived based on the adjoint variable method and incorporated into the level-set-based topology optimization, where the level-set function was updated using the time evolutionary reaction-diffusion equation. In the numerical implementation, an optimization algorithm using FEM was constructed.

3. 2D and 3D design examples were provided. In all models, an optimal configuration was obtained in which the support structure was added to the overhang region to improve heat dissipation. The improved heat dissipation in the optimal configuration was confirmed by the LPBF analytical model, demonstrating the validity and effectiveness of the proposed method.

Chapter 4

Self-support topology optimization considering distortion for metal additive manufacturing

4.1 Introduction

The most noticeable issue in AM that limits manufacturability is the overhang limitation. This limitation means that there is a limit to the overhang angle, the angle between the downward-facing surface and the base plate. If the overhang angle exceeds a threshold angle, the overhang shape may collapse under its own weight. In this study, this overhang is termed the overhanging region. Results from Chapters 2 and 3 show that overhanging regions is one of the factors contributing to distortion and overheating. Therefore, this chapter proposes a self-supporting topology optimization method that suppresses the distortion and overheating.

Several self-support topology optimization methods have been proposed to eliminate overhanging regions. These approaches use two main approaches: a density filter and an explicit angle constraint. Density filtering is a common technique used in density-based topology optimization frameworks to ensure a self-supporting structure [27, 37, 38]. The optimal structures obtained using this approach have sharp inner corners, and several methods have been proposed to prevent their occurrence [65, 25, 60]. These methods generate rounded shapes and do not strictly satisfy the angle constraint. The explicit angle constraint is a technique that can be applied to both density- and level-set-based topology optimization

frameworks. This technique can be easily incorporated into the above frameworks using a gradient of the element density or level-set function. However, the constraint on the normal direction of the geometry is known to create downward convex shapes that cannot be manufactured. In the density-based framework, Qian [55] proposed a suppression method that added perimeter and grayness constraints but reported that the parameters of each constraint are not easy to set. Using the level-set-based framework, Wang et al. [67] facilitated the detection of the downward convex shapes by formulating the overhang angle constraint as a domain integral but did not discuss how to suppress it. Allaire et al. [4] successfully suppressed the downward convex shapes by imposing mechanical constraints to prevent the part that is to be manufactured from collapsing under its weight during the building process. However, this method does not sufficiently eliminate overhanging regions and may adversely affect structural compliance because it considers the self-weight of the entire geometry. Therefore, it is necessary to establish a method for eliminating the overhanging region and downward convex shape when the explicit angle constraint technique is applied. Furthermore, few studies have combined overhang angle constraint with other constraints such as distortion.

This chapter provides a new self-support topology optimization that considers distortion. The remainder of this chapter is organized as follows. First, we formulate an overhang angle constraint using a Helmholtz-type partial differential equation (PDE) and propose a method to suppress the downward convex shape using a thermal model. Next, we introduce the AM process model based on the inherent strain method and present a formulation of the distortion constraint. We then formulate an optimization problem considering multiple constraints. Furthermore, we construct an optimization algorithm using the finite element method (FEM). Finally, the 2D and 3D design examples are presented to demonstrate the utility of the proposed optimization method.

4.2 Self-support constraint

This section introduces an overhang angle constraint in the level-set-based framework and a method for suppressing the downward convex shape.

4.2.1 Smoothed characteristic function based on Helmholtz-type PDE

Allaire et al. [4] and Wang et al. [67] used the gradient of the level set function to directly formulate the overhang angle constraint. In this study, a Helmholtz-type partial differential equation (PDE) is introduced to limit the overhang angle using the gradient of the projected characteristic function χ_ϕ. The physical variable $\psi \in H^1(D)$ and its governing equation are defined as follows:

$$\begin{cases} -aL^2\nabla^2\psi + \psi = \chi_\phi & \text{in} \quad D \\ \boldsymbol{n} \cdot \nabla\psi = 0 & \text{on} \quad \partial\Omega, \end{cases} \tag{4.1}$$

where $a \in \mathbb{R}^+$ is the isotropic diffusion coefficient, L is the representative length, and $\boldsymbol{n}$ is the outward normal vector. The diffusion coefficient a affects the transition width ψ. In other words, the evaluation of the overhanging region can be controlled by adjusting the diffusion coefficient a. Furthermore, it can also control the downward convex shape.

4.2.2 Overhang angle constraint function and its derivative

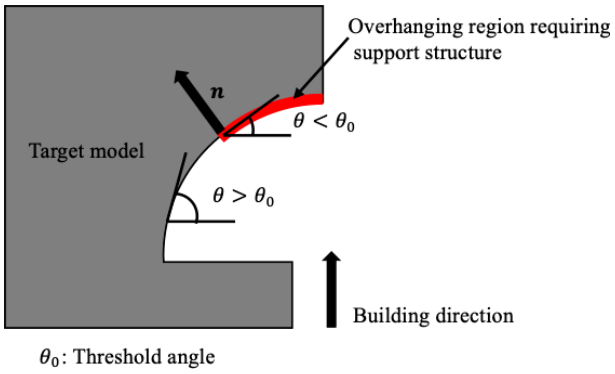

Fig. 4.1 Schematic of the overhanging region in additive manufacturing.

Fig. 4.1 shows an example of the overhanging region in additive manufacturing. A support structure is required to build an overhanging region above a certain angle to the horizontal plane. In the explicit overhang angle constraint, a common method for detecting overhanging regions is evaluating the angle between the normal vector $\boldsymbol{n}$ from the structural boundary $\partial\Omega$ and the building direction. In this study, the overhanging region is detected by directly evaluating the inner product of the normal vector $\boldsymbol{n}_\psi := \nabla\psi$ from the structural

boundary $\partial\Omega$ and threshold angle vectors $\boldsymbol{d}_1$ and $\boldsymbol{d}_2$. For the 2D problem, the threshold angle vectors $\boldsymbol{d}_1$ and $\boldsymbol{d}_2$ are given by

$$\boldsymbol{d}_1 = \begin{pmatrix} -\cos\theta_0 \\ -\sin\theta_0 \end{pmatrix}, \quad \boldsymbol{d}_2 = \begin{pmatrix} \cos\theta_0 \\ -\sin\theta_0 \end{pmatrix}. \tag{4.2}$$

An overhanging region is detected when both inner products take positive values. Therefore, the condition for constraining the overhang angle is given by

$$\int_D R(\nabla\psi \cdot \boldsymbol{d}_1) R(\nabla\psi \cdot \boldsymbol{d}_2)\, \mathrm{d}\Omega = 0, \tag{4.3}$$

where $R(s) := (s + |s|)/2$ denotes the ramp function. Furthermore, the overhang angle constraint normalizes the above equation and is defined as

$$G_o = \int_D R(\sqrt{a}L\nabla\psi \cdot \boldsymbol{d}_1) R(\sqrt{a}L\nabla\psi \cdot \boldsymbol{d}_2)\, \mathrm{d}\Omega, \tag{4.4}$$

To validate the formulated PDE and overhang angle constraint, a numerical example using the FEM is provided and is shown in Fig. 4.2. The analysis domain D consists of two domains with the target model shown in Fig. 4.1 as the material domain Ω and the other region as the void domain $D\backslash\Omega$. The domain D has dimensions of 1.0×1.2 and is discretized into a mesh of second-order triangular elements. The diffusion coefficient a is set to 1×10^{-4}, representative length L is set to 1.0, and threshold angle θ_0 is set to 45°. Fig. 4.2(a) shows the distribution of ψ that was obtained by solving Eq. 4.1. ψ smoothly transitions from the material domain to the void domain. Figs. 4.2 (b), (c), and (d) indicate that the region where both inner products assume positive values is the overhanging region. Fig. 4.2 (e) shows the overhanging region obtained from the comparison of the cosine value with the inner product of the normal vector $\boldsymbol{n}_\psi$ and the building direction $\boldsymbol{d}$. Compared with the aforementioned conventional method, the proposed constraint function is able to detect overhanging regions near the threshold angle. This implies that during the optimization process, the overhanging regions near the threshold angle are also optimized to satisfy the constraint. Fig. 4.2 (f) shows the result with the diffusion coefficient a set to 1×10^{-3}. This result indicates that the diffusion coefficient a affects the evaluation area of the overhanging region. The overhang angle constraint in the 3D problem is given by adding the threshold angle vectors of an

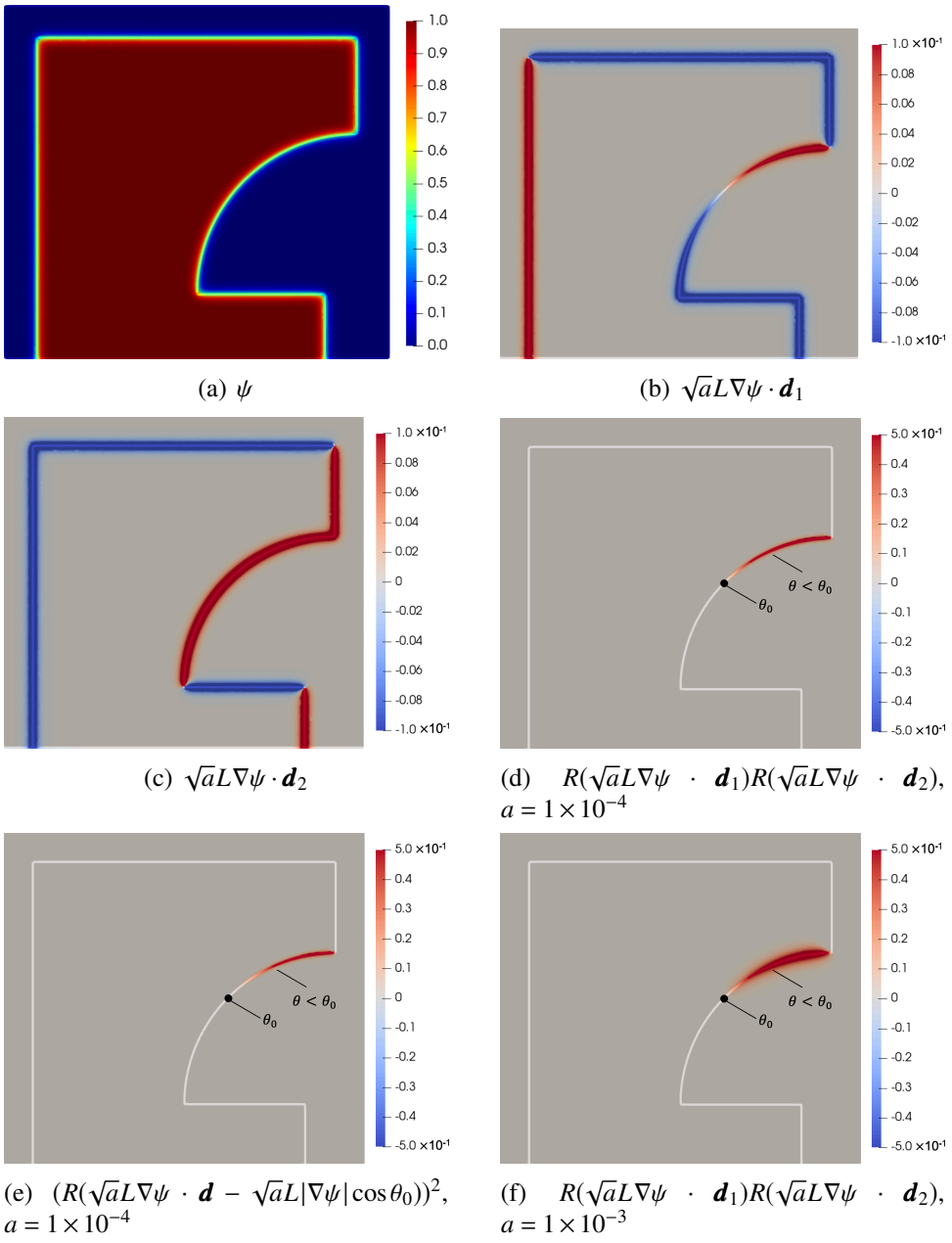

(a) ψ

(b) $\sqrt{a}L\nabla\psi \cdot \boldsymbol{d}_1$

(c) $\sqrt{a}L\nabla\psi \cdot \boldsymbol{d}_2$

(d) $R(\sqrt{a}L\nabla\psi \cdot \boldsymbol{d}_1)R(\sqrt{a}L\nabla\psi \cdot \boldsymbol{d}_2)$, $a = 1\times10^{-4}$

(e) $(R(\sqrt{a}L\nabla\psi \cdot \boldsymbol{d} - \sqrt{a}L|\nabla\psi|\cos\theta_0))^2$, $a = 1\times10^{-4}$

(f) $R(\sqrt{a}L\nabla\psi \cdot \boldsymbol{d}_1)R(\sqrt{a}L\nabla\psi \cdot \boldsymbol{d}_2)$, $a = 1\times10^{-3}$

Fig. 4.2 Numerical example of the overhang angle constraint.

orthogonal plane, as follows:

$$G_o = \int_D R(\sqrt{a}L\nabla\psi \cdot \boldsymbol{d}_1)R(\sqrt{a}L\nabla\psi \cdot \boldsymbol{d}_2) + R(\sqrt{a}L\nabla\psi \cdot \boldsymbol{d}_3)R(\sqrt{a}L\nabla\psi \cdot \boldsymbol{d}_4)\,\mathrm{d}\Omega, \tag{4.5}$$

where

$$\boldsymbol{d}_1 = \begin{pmatrix} -\cos\theta_0 \\ -\sin\theta_0 \\ 0 \end{pmatrix}, \quad \boldsymbol{d}_2 = \begin{pmatrix} \cos\theta_0 \\ -\sin\theta_0 \\ 0 \end{pmatrix},$$
$$\boldsymbol{d}_3 = \begin{pmatrix} \cos\theta_0 \\ 0 \\ -\sin\theta_0 \end{pmatrix}, \quad \boldsymbol{d}_4 = \begin{pmatrix} \cos\theta_0 \\ 0 \\ -\sin\theta_0 \end{pmatrix}. \tag{4.6}$$

Fig. 4.3 presents the results of the evaluation of the overhanging region with the 1/4 hemi-

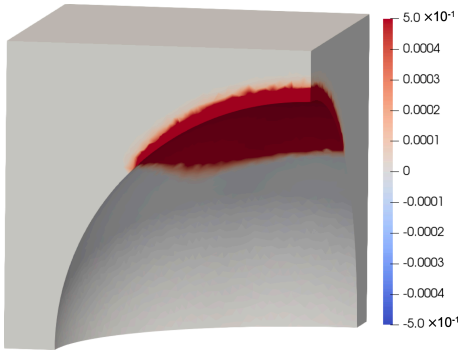

Fig. 4.3 Numerical example of 3D model.

spheric model using Eq. 4.5. The overhanging region can be detected in the 3D case as well as in the 2D case. Next, the topological derivative of the overhang angle constraint is derived using the adjoint variable method. The adjoint variable $\tilde{\psi} \in H^1(D)$ and its adjoint equation are defined as follows:

$$\begin{cases} -aL^2\nabla^2\tilde{\psi} + \tilde{\psi} = \dfrac{\partial G_o}{\partial \psi} & \text{in} \quad D \\ \boldsymbol{n}\cdot\nabla\tilde{\psi} = 0 & \text{on} \quad \partial\Omega, \end{cases} \tag{4.7}$$

where

$$\frac{\partial G_o}{\partial \psi} = \begin{cases} \nabla \cdot \left[H(\sqrt{a}L\nabla\psi \cdot \boldsymbol{d}_1) R(\sqrt{a}L\nabla\psi \cdot \boldsymbol{d}_2) \boldsymbol{d}_1 \right. & \\ \left. + R(\sqrt{a}L\nabla\psi \cdot \boldsymbol{d}_1) H(\sqrt{a}L\nabla\psi \cdot \boldsymbol{d}_2) \boldsymbol{d}_2 \right] \tilde{\psi} & \text{if } N = 2 \\ \\ \nabla \cdot \left[H(\sqrt{a}L\nabla\psi \cdot \boldsymbol{d}_1) R(\sqrt{a}L\nabla\psi \cdot \boldsymbol{d}_2) \boldsymbol{d}_1 \right. & \\ \left. + R(\sqrt{a}L\nabla\psi \cdot \boldsymbol{d}_1) H(\sqrt{a}L\nabla\psi \cdot \boldsymbol{d}_2) \boldsymbol{d}_2 \right] \tilde{\psi} & \\ + \nabla \cdot \left[H(\sqrt{a}L\nabla\psi \cdot \boldsymbol{d}_3) R(\sqrt{a}L\nabla\psi \cdot \boldsymbol{d}_4) \boldsymbol{d}_3 \right. & \\ \left. + R(\sqrt{a}L\nabla\psi \cdot \boldsymbol{d}_3) H(\sqrt{a}L\nabla\psi \cdot \boldsymbol{d}_4) \boldsymbol{d}_4 \right] \tilde{\psi} & \text{if } N = 3. \end{cases} \tag{4.8}$$

Here, $H(s) := \mathrm{d}R(s)/\mathrm{d}s$ is the Heaviside function and N is the number of spatial dimensions. As only the source term in Eq. 4.1 is affected by the characteristic function χ_ϕ, the topological derivative [14] of the overhang angle constraint G_o is derived as follows:

$$G_o' = -\tilde{\psi}. \tag{4.9}$$

4.2.3 Thermal model for the downward convex shapes

As mentioned in the introduction, the above overhang angle constraint creates downward convex shapes. In actual manufacturing, these shapes impede heat flow, causing overheating, which generates undesirable defects such as porosity and degraded surface quality. Therefore, we propose a method to suppress the downward convex shapes by considering heat dissipation in the AM building process. Several analytical models have been proposed to detect overheating during thermal processes. For the steady-state heat conduction problem, Ranjan et al.[56] proposed a model in which heat flux is applied layer-by-layer, whereas Wang et al.[66] proposed a model in which heat flux is applied only to the overhang boundaries, and not layer-by-layer. In this study, we consider a thermal model that applies heat flux to the overhang boundary at each layer, as shown in Fig. 4.4. First, to represent the building process, the domain Ω is divided into m layers with a fixed thickness in the building direction. The domain Ω is defined by each domain Ω_i for $1 \leq i \leq m$. Moreover, the domain Ω consists of three subdomains: the activated domain Ω_A, inactive domain Ω_I, and activating domain Ω_q, which is determined by the activation status of Ω_i. The activated domain Ω_A is occupied by an isotropic material with thermal conductivity k, and a fixed temperature boundary condition is applied to the base plate Γ_T. Then, the temperature field

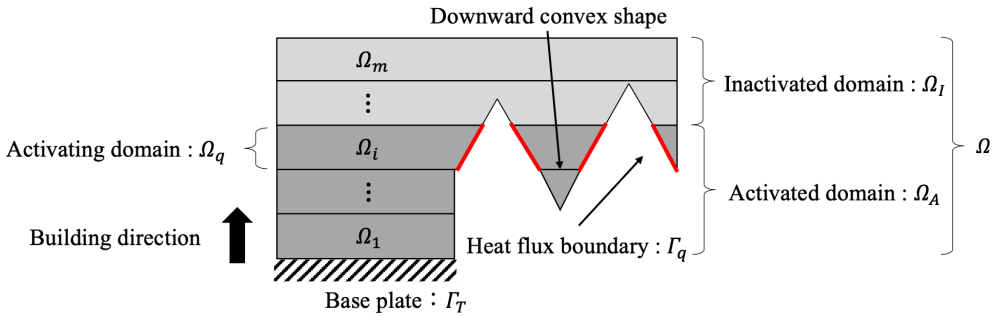

Fig. 4.4 Domains and boundaries of the thermal model in the building process.

$T_i \in H^1(\Omega_A)$ with heat flux q applied to the overhang boundary Γ_q of the added layer Ω_q is represented by the following governing equation:

$$\begin{cases} \operatorname{div}(k\nabla T_i) = 0 & \text{in } \Omega_A \\ (k\nabla T_i)\cdot \boldsymbol{n} = q & \text{on } \Gamma_q \\ T_i = T_{amb} & \text{on } \Gamma_T, \end{cases} \tag{4.10}$$

for all indices $i = 1, 2, \ldots, m$, where T_{amb} is the temperature of the base plate, which acts as a heat sink.

4.2.4 Thermal constraint function and its derivative

The thermal constraint function that improves the heat dissipation of each domain Ω_i is defined as follows:

$$G_t = \sum_{i=1}^{m} \int_{\Omega_i} (T_i - T_{amb})^2 \, \mathrm{d}\Omega. \tag{4.11}$$

Next, the topological derivative of the thermal constraint is derived using the adjoint variable method. The adjoint variable $\tilde{T} \in H^1(\Omega_A)$ and its adjoint equation are defined as follows:

$$\begin{cases} \operatorname{div}(k\nabla \tilde{T}_i) = 2(T_i - T_{amb}) & \text{in } \Omega_A, \\ (k\nabla \tilde{T}_i)\cdot \boldsymbol{n} = 0 & \text{on } \Omega_A \setminus \Gamma_T, \\ \tilde{T}_i = T_{amb} & \text{on } \Gamma_T, \end{cases} \tag{4.12}$$

Subsequently, the topological derivative of the thermal constraint G_t is derived as follows [48, 30]:

$$G_t' = \sum_{i=1}^{m} -k\nabla T_i \cdot \nabla \tilde{T}_i. \tag{4.13}$$

4.3 Distortion constraint

4.3.1 Mechanical model based on the inherent strain method

The mechanical model for predicting the part-scale residual stress and distortion uses the inherent strain method, which applies the strain for each layer, as shown in Fig. 4.5. The

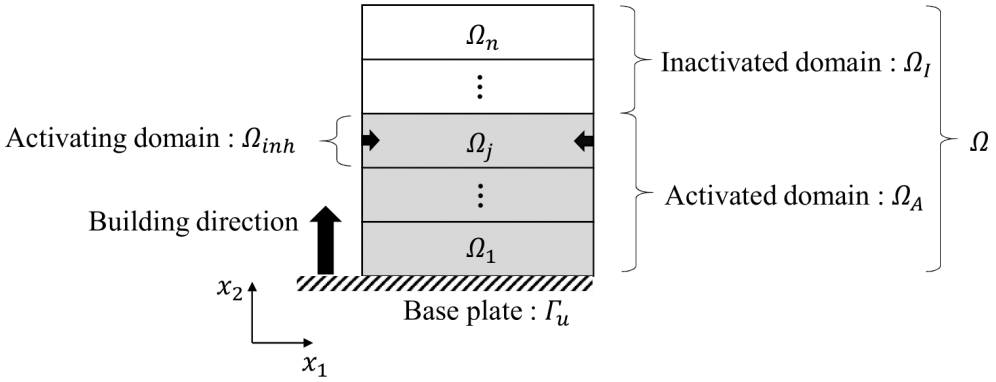

Fig. 4.5 Domains and boundaries of the mechanical model in the building process.

domain is divided into n layers with a fixed thickness, as in the thermal model, and consists of three subdomains. The domain Ω is defined by each domain Ω_j for $1 \leq j \leq n$. Note that each subdomain region is determined by the activation status of Ω_j. The activated domain Ω_A is occupied by an isotropic elastic material, and a fixed displacement boundary condition is applied to the base plate Γ_u. The displacement $\boldsymbol{u}_j \in H^1(\Omega_A)^N$ with inherent strain $\boldsymbol{\varepsilon}^{inh}$ applied to the domain Ω_{inh} is represented by the following governing equation:

$$\begin{cases} -\mathrm{div}(\boldsymbol{\sigma}_j) = 0 & \text{in } \Omega_A \\ \boldsymbol{\sigma}_j = \mathbb{C}\boldsymbol{\varepsilon}(\boldsymbol{u}_i) - \mathbb{C}\boldsymbol{\varepsilon}^{inh}, & \\ \boldsymbol{u}_j = \boldsymbol{0} & \text{on } \Gamma_u \\ -\boldsymbol{\sigma}_j \cdot \boldsymbol{n} = \boldsymbol{0} & \text{on } \partial\Omega_A \setminus \Gamma_u, \end{cases} \tag{4.14}$$

for all indices $j = 1, 2, \ldots, n$, where $\boldsymbol{\sigma}$ denotes the stress tensor, $\mathbb{C}$ denotes the elasticity tensor, and $\boldsymbol{\varepsilon}(\boldsymbol{u})$ denotes the total strain tensor. Note that the above equation represents an elastic analysis that does not consider plastic deformation. The inherent strain $\boldsymbol{\varepsilon}^{inh}$ in the domain Ω_{inh} is defined as follows:

$$\boldsymbol{\varepsilon}^{inh}(\boldsymbol{x}) = \begin{cases} \boldsymbol{\varepsilon}^{inh} & \text{for } \boldsymbol{x} \in \Omega_{inh}, \\ \mathbf{0} & \text{otherwise}, \end{cases} \tag{4.15}$$

where $\boldsymbol{x}$ denotes a point located in Ω_A. In this study, the inherent strain component is set as $\varepsilon_x^{inh} = \varepsilon_y^{inh} = -0.0025$ and $\varepsilon_z^{inh} = 0$ in the 3D case. In addition, the domain is divided in the building direction at 1 mm per layer for computational cost. For a detailed discussion of the methods for identifying the inherent strain $\boldsymbol{\varepsilon}^{inh}$, the building process algorithm using the FEM, and the number of layers n suitable for topology optimization, refer to Miki et al. [45]. The residual stress and distortion after the end of the building process are expressed as follows:

$$\boldsymbol{\sigma} = \sum_{j=1}^{n} \boldsymbol{\sigma}_j \quad \text{for } \boldsymbol{x} \in \Omega_A, \tag{4.16}$$

$$\boldsymbol{u} = \sum_{j=1}^{n} \boldsymbol{u}_j \quad \text{for } \boldsymbol{x} \in \Omega_A. \tag{4.17}$$

4.3.2 Distortion constraint function and its derivative

The distortion constraint function is defined using the P-norm function, as follows:

$$G_u = \sum_{j=1}^{n} \left(\int_{\Omega_A} \left| \boldsymbol{u}_j \right|^b \, \mathrm{d}\Omega \right)^{1/b}, \tag{4.18}$$

where $b \geq 2$ is the penalization parameter set to 5 in this study. Next, the topological derivative of the distortion constraint is derived using the adjoint variable method. The adjoint variable $\tilde{\boldsymbol{u}}_j \in H^1(\Omega_A)^N$ and its adjoint equation are defined as follows:

$$\begin{cases} -\mathrm{div}(\mathbb{C}\boldsymbol{\varepsilon}(\tilde{\boldsymbol{u}}_j)) = -\left(\int_{\Omega_A} \left| \boldsymbol{u}_j \right|^b \, \mathrm{d}\Omega \right)^{1/b-1} \left| \boldsymbol{u}_j \right|^{b-2} \boldsymbol{u}_j & \text{in } \Omega_A, \\ \tilde{\boldsymbol{u}}_j = \mathbf{0} & \text{on } \Gamma_u, \\ -(\mathbb{C}\boldsymbol{\varepsilon}(\tilde{\boldsymbol{u}}_j)) \cdot \boldsymbol{n} = \mathbf{0} & \text{on } \partial\Omega_A \setminus \Gamma_u, \end{cases} \tag{4.19}$$

for all indices $j = 1, 2, \ldots, n$ and the topological derivative of the distortion constraint G_u is derived as follows [45, 31]:

$$G'_u = \sum_{j=1}^{n} \left(-\boldsymbol{\varepsilon}(\boldsymbol{u}_j) : \mathbb{A} : \boldsymbol{\varepsilon}(\tilde{\boldsymbol{u}}_j) + \boldsymbol{\varepsilon}^{inh} : \mathbb{A} : \boldsymbol{\varepsilon}(\tilde{\boldsymbol{u}}_j) \right), \tag{4.20}$$

where the constant fourth-order tensor $\mathbb{A}$ is given by

$$\mathbb{A}_{ijkl} = \frac{3(1-\nu)}{2(1+\nu)(7-5\nu)} \left\{ \frac{-\left(1-14\nu+15\nu^2\right) E}{(1-2\nu)^2} \delta_{ij}\delta_{kl} + 5E \left(\delta_{ik}\delta_{jl} + \delta_{il}\delta_{jk} \right) \right\}, \tag{4.21}$$

where E, ν, and δ are the Young's modulus, Poisson's ratio, and Kronecker delta, respectively.

4.4 Formulation of the optimization problem

4.4.1 Minimum mean compliance problem

First, we incorporate the aforementioned constraints into the minimum mean compliance problem. In this problem, the material domain Ω is fixed at the boundary Γ_v, and traction $\boldsymbol{t}$ is applied at the boundary Γ_t. The displacement field is denoted by $\boldsymbol{v} \in H^1(\Omega)^N$ in the static equilibrium state, and the objective function is defined as

$$J_v = \int_{\Gamma_t} \boldsymbol{t} \cdot \boldsymbol{v} \mathrm{d}\Gamma. \tag{4.22}$$

The optimization problem is formulated as an unconstrained problem by including the constraint function as a penalty term in the objective function, as follows:

$$\inf_{\phi} \quad J = (1-\alpha)\frac{J_v \int_D \mathrm{d}\Omega}{\int_D |J_v|\,\mathrm{d}\Omega} + \alpha\frac{G_u \int_D \mathrm{d}\Omega}{\int_D |G_u|\,\mathrm{d}\Omega} + \beta G_o + \gamma\frac{G_t \int_D \mathrm{d}\Omega}{\int_D |G_t|\,\mathrm{d}\Omega} \tag{4.23}$$

$$\text{subject to :}\ E_v = \int_{\Gamma_t} \boldsymbol{t}\cdot\tilde{\boldsymbol{v}}\,\mathrm{d}\Gamma - \int_{\Omega} \varepsilon(\boldsymbol{v}) : \mathbb{C} : \varepsilon(\tilde{\boldsymbol{v}})\,\mathrm{d}\Omega = 0 \tag{4.24}$$

$$\text{for } \forall\tilde{\boldsymbol{v}} \in \mathcal{V}, \boldsymbol{v} \in \mathcal{V}$$

$$E_u = \int_{\Omega_{inh}} \boldsymbol{\varepsilon}^{inh} : \mathbb{C} : \varepsilon(\tilde{\boldsymbol{u}_j})\,\mathrm{d}\Omega - \int_{\Omega_A} \varepsilon(\boldsymbol{u}_j) : \mathbb{C} : \varepsilon(\tilde{\boldsymbol{u}})\,\mathrm{d}\Omega = 0 \tag{4.25}$$

$$\text{for } \forall\tilde{\boldsymbol{u}_j} \in \mathcal{U}, \boldsymbol{u}_j \in \mathcal{U}$$

$$E_\psi = -\int_D aL^2\nabla\psi\cdot\nabla\tilde{\psi}\,\mathrm{d}\Omega - \int_D \psi\tilde{\psi}\,\mathrm{d}\Omega - \int_D \chi_\phi\tilde{\psi}\,\mathrm{d}\Omega = 0 \tag{4.26}$$

$$\text{for } \forall\tilde{\psi} \in \mathcal{S}, \psi \in \mathcal{S}$$

$$E_t = \int_{\Gamma_q} q\tilde{T}_i\,\mathrm{d}\Gamma - \int_{\Omega_A} \nabla T_i\cdot\nabla\tilde{T}_i\,\mathrm{d}\Omega = 0 \tag{4.27}$$

$$\text{for } \forall\tilde{T}_i \in \mathcal{T}, T_i \in \mathcal{T}$$

$$G = \int_D \tilde{\chi}\ \mathrm{d}\Omega - V_{\max} \le 0,$$

for all indices $i = 1,2,\ldots,m$, $j = 1,2,\ldots,n$, where $0 \le \alpha \le 1$, β, and γ are the weighting parameters. In the above formulation, G represents the volume constraint, and V_{max} is the upper limit of the material volume in D. Furthermore, functional spaces $\mathcal{V}$, $\mathcal{U}$, $\mathcal{S}$, and $\mathcal{T}$ are defined as follows:

$$\mathcal{V} := \left\{\tilde{\boldsymbol{v}} \in H^1(\Omega)^N,\ \tilde{\boldsymbol{v}} = \boldsymbol{0}\ \text{ on }\ \Gamma_v\right\} \tag{4.28}$$

$$\mathcal{U} := \left\{\tilde{\boldsymbol{u}_j} \in H^1(\Omega_A)^N,\ \tilde{\boldsymbol{u}_j} = \boldsymbol{0}\ \text{ on }\ \Gamma_u\right\} \tag{4.29}$$

$$\mathcal{S} := \left\{\tilde{\psi} \in H^1(D)\right\} \tag{4.30}$$

$$\mathcal{T} := \left\{\tilde{T}_i \in H^1(\Omega_A),\ \tilde{T}_i = T_{amb}\ \text{ on }\ \Gamma_T\right\} \tag{4.31}$$

The minimum mean compliance problem is known as a self-adjoint problem. Therefore, the adjoint variable is equivalent to the displacement field $\boldsymbol{v}$, and the topological derivative

of the minimum mean compliance problem is derived as follows [26, 20]:

$$J'_v = -\boldsymbol{\varepsilon}(\boldsymbol{v}) : \mathbb{A} : \boldsymbol{\varepsilon}(\boldsymbol{v}). \tag{4.32}$$

4.4.2 Thermal diffusion problem

Next, we consider the steady-state heat conduction problem with internal heat generation. In this problem, the heat source Q is applied to the design domain D, and the temperature $p = p_{amb}$ is fixed at the boundary Γ_p. The temperature field is denoted by $p \in H^1(\Omega)$ in the static equilibrium state, and the objective function is defined as

$$J_p = \int_D Qp \, \mathrm{d}\Omega. \tag{4.33}$$

This objective function is called the thermal compliance [28]. Subsequently, by replacing the objective function in Eq. 4.23 and the governing equation in Eq. 4.24, the optimization problem is formulated as follows:

$$\begin{aligned}
\inf_{\phi} \quad & J = (1-\alpha)\frac{J_p \int_D \mathrm{d}\Omega}{\int_D |J_p| \, \mathrm{d}\Omega} + \alpha \frac{G_u \int_D \mathrm{d}\Omega}{\int_D |G_u| \, \mathrm{d}\Omega} \\
& \qquad + \beta G_o + \gamma \frac{G_t \int_D \mathrm{d}\Omega}{\int_D |G_t| \mathrm{d}\Omega} && (4.34) \\
\text{subject to :} \quad & E_p = \int_D Q\tilde{p} \, \mathrm{d}\Omega - \int_\Omega k \nabla p \cdot \nabla \tilde{p} \, \mathrm{d}\Omega = 0 && (4.35) \\
& \qquad \text{for } \forall \tilde{p} \in \mathcal{P}, p \in \mathcal{P} \\
& E_u = 0 \\
& \qquad \text{for } \forall \tilde{\boldsymbol{u}}_j \in \mathcal{U}, \boldsymbol{u}_j \in \mathcal{U} \\
& E_\psi = 0 \\
& \qquad \text{for } \forall \tilde{\psi} \in \mathcal{S}, \psi \in \mathcal{S} \\
& E_t = 0 \\
& \qquad \text{for } \forall \tilde{T}_i \in \mathcal{T}, T_i \in \mathcal{T} \\
& G \leq 0.
\end{aligned}$$

The functional space is defined as follows:

$$\mathcal{P} := \left\{ \tilde{p} \in H^1(\Omega_A),\ \tilde{p} = p_{amb} \ \text{ on } \ \Gamma_p \right\} \tag{4.36}$$

This optimization problem is also a self-adjoint problem and is similar to the minimum mean compliance problem. Therefore, the topological derivative of this optimization problem is derived as follows:

$$J'_p = -k \nabla p \cdot \nabla p. \tag{4.37}$$

4.5 Numerical implementation

4.5.1 Optimization algorithm

The optimization algorithm is as follows:

Step1. The initial value of the level set function ϕ is set to the fixed design domain D.

Step2. The governing equations for the target physics and each state variable defined in Eqs. 4.1, 4.10, and 4.14 are solved by the FEM.

Step3. The objective function J with respect to the target physics is calculated.

Step4. If the objective function converges, the optimization procedure is terminated; otherwise, each adjoint variable defined in Eq. 4.7, 4.12, and 4.19 is solved by the FEM, and the sum of the topological derivative J' is calculated.

Step5. The level set function is updated using the time-evolution equation given by Eq. 1.17; then, the optimization procedure returns to the second step.

4.5.2 Numerical scheme for the governing equation

In this study, the material and void domains are distinguished using the ersatz material approach [6] from the perspective of computational cost. Specifically, we assume that the void domain has a small material property and that the boundary between the material and void domains has a smoothly distributed material property. Subsequently, the extended elastic tensor $\tilde{\mathbb{C}}$ and thermal conductivity $\tilde{k}$ for solving the governing equations in the fixed

design domain D are defined as follows:

$$\tilde{\mathbb{C}}(\phi; w) = \left\{(1-c)H_\phi(\phi; w) + c\right\}\mathbb{C} \tag{4.38}$$

$$\tilde{k}(\phi; w) = \left\{(1-c)H_\phi(\phi; w) + c\right\}k, \tag{4.39}$$

where $H_\phi(\phi; w)$ is defined as

$$H_\phi(\phi; w) := \begin{cases} 1 & \text{for } \phi > w, \\ \frac{1}{2} + \frac{\phi}{w}\left(\frac{15}{16} - \frac{\phi^2}{w^2}\left(\frac{5}{8} - \frac{3}{16}\frac{\phi^2}{w^2}\right)\right) & \text{for } -w \le \phi \le w, \\ 0 & \text{for } \phi < -w. \end{cases} \tag{4.40}$$

Here, w represents the width of the transition, and c is the ratio of the material properties for the material and void domains. Moreover, Eqs. 4.1 and 4.7 are solved by replacing the characteristic function χ_ϕ with the following Heaviside function:

$$\chi_\phi = H_\phi(\phi; \xi). \tag{4.41}$$

In our implementation, we set $c = 1.0 \times 10^{-3}$, $w = 0.5$ and $\xi = 0.9$.

Next, an approximate solution method for the heat conduction equation defined in Eq. 4.27 is introduced. Here, we replace the boundary integral with a domain integral using the Dirac delta function $\delta(\boldsymbol{x})$, as follows:

$$\int_\Gamma \xi(\boldsymbol{x}) \mathrm{d}\Gamma \approx \int_\Omega \xi(\boldsymbol{x})\delta(\boldsymbol{x})\, \mathrm{d}\Omega, \tag{4.42}$$

The delta function $\delta(\boldsymbol{x})$ is expressed using the Heaviside function $H_\psi(\psi; w)$, as follows:

$$\delta(\boldsymbol{x}) = \nabla H_\psi(\psi; w) \cdot \boldsymbol{n}_\psi, \tag{4.43}$$

where $\boldsymbol{n}_\psi$ denotes the normal vector for $H_\psi(\psi; w)$. The above equation can be rewritten as

$$\delta(\boldsymbol{x}) = \frac{\mathrm{d}H_\psi(\psi; w)}{\mathrm{d}\psi}\nabla\psi \cdot \frac{\nabla\psi}{|\nabla\psi|} = \frac{\mathrm{d}H_\psi(\psi; w)}{\mathrm{d}\psi}|\nabla\psi|. \tag{4.44}$$

Then, only the overhang boundary is extracted using the inner product of the normal vector $\boldsymbol{n}_\psi$ and the building direction $\boldsymbol{d}$, as follows:

$$\int_{\Gamma_q} \xi(\boldsymbol{x}) \mathrm{d}\Gamma \approx \int_{\Omega_q} \xi(\boldsymbol{x}) \frac{\mathrm{d}H_\psi(\psi; w)}{\mathrm{d}\psi} |\nabla\psi| H(\boldsymbol{n}_\psi \cdot \boldsymbol{d}) \mathrm{d}\Omega. \tag{4.45}$$

Substituting the above equation into Eq. 4.27 yields

$$E_t = \int_{\Omega_q} q\tilde{T}_i \frac{\mathrm{d}H_\psi(\psi; w)}{\mathrm{d}\psi} |\nabla\psi| H(\boldsymbol{n}_\psi \cdot \boldsymbol{d}) \, \mathrm{d}\Omega - \int_{\Omega_A} \nabla T_i \cdot \nabla\tilde{T}_i \, \mathrm{d}\Omega = 0 \tag{4.46}$$

4.6 Numerical examples

4.6.1 Verification of the self-support constraint

Effect of overhang angle constraint parameters

This subsection presents optimization examples with only the imposed overhang angle constraint. The optimization example considers the minimum mean compliance problem for a symmetric 2D MBB beam, as shown in Fig. 4.6. The material adopted in this study is

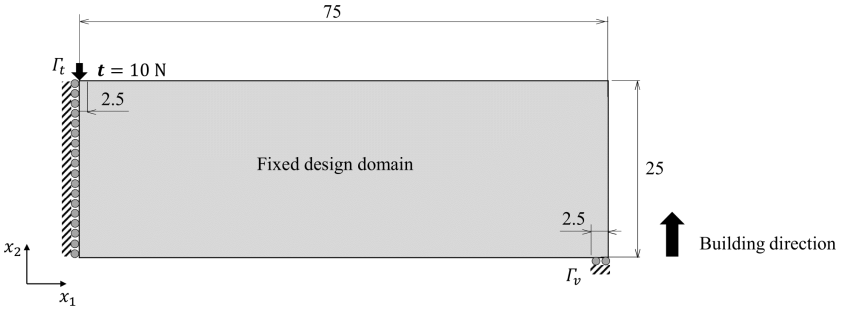

Fig. 4.6 Problem setting for the MBB beam, with the dimensions in mm.

AlSi10Mg, which has a Young's modulus of 75 GPa and Poisson's ratio of 0.34. The upper limit of the allowable volume is set to 50% of the fixed design domain. The representative length in Eq. 4.1 is set to L =25 mm. The threshold angle is set to $\theta_0 = 45°$. Here, we examine the effects of the parameters related to the overhang angle constraint β and diffusion coefficient a in Eq. 4.1. Figs. 4.7 and 4.8 show the set of optimization results obtained under different overhang angle constraints β and diffusion coefficients a. As shown in Fig. 4.7, increasing β eliminates the overhanging region, but creates many downward convex

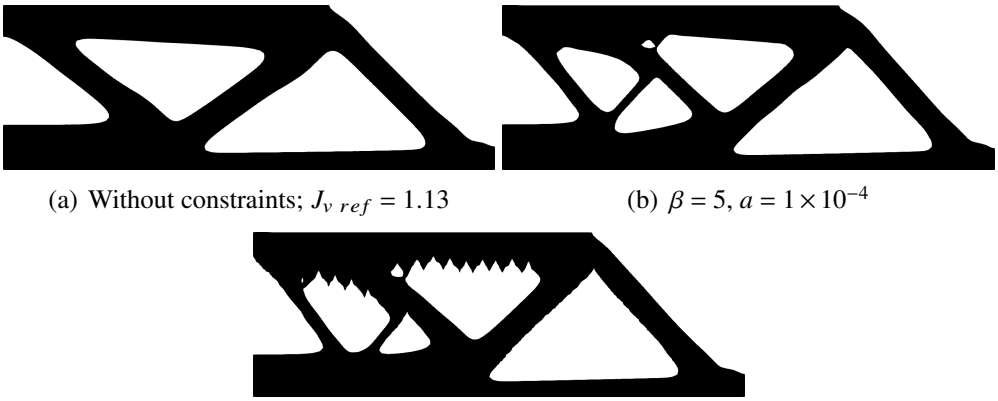

(a) Without constraints; $J_{v\ ref} = 1.13$ (b) $\beta = 5$, $a = 1 \times 10^{-4}$

(c) $\beta = 20$, $a = 1 \times 10^{-4}$

Fig. 4.7 Optimized MBB beams under different overhang angle constraint parameters β.

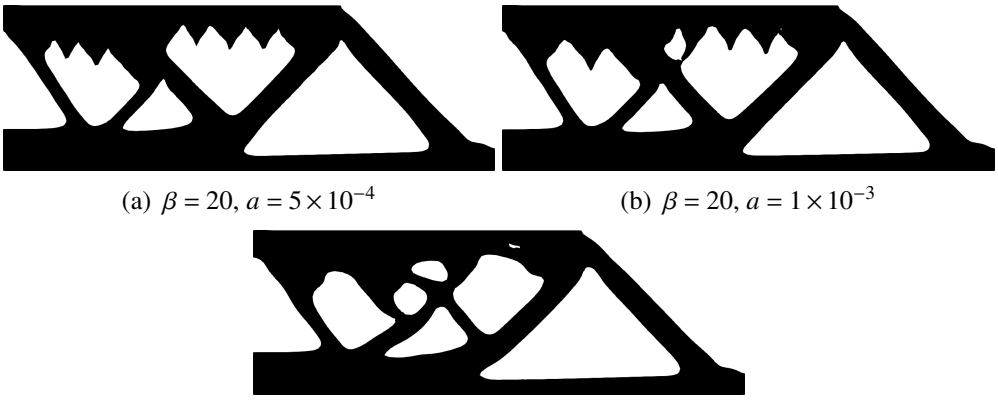

(a) $\beta = 20$, $a = 5 \times 10^{-4}$ (b) $\beta = 20$, $a = 1 \times 10^{-3}$

(c) $\beta = 20$, $a = 5 \times 10^{-3}$

Fig. 4.8 Optimized MBB beams under different diffusion coefficients a.

shapes. By contrast, increasing the diffusion coefficient a suppresses the downward convex shapes but creates an overhanging region, as shown in Fig. 4.8. This is because the diffusion coefficient affects the evaluation area of the overhanging region, as shown in Fig. 4.2. In other words, if a is set larger than 5×10^{-3}, the evaluation area is too large. Therefore, the diffusion coefficient a should be set in the range 1×10^{-4} to 1×10^{-3}. In the following optimization examples, $\beta = 20$ and $a = 5 \times 10^{-4}$ are set. This result shows that constraining only the overhang angle is insufficient. Therefore, to satisfy the self-support constraint, it is necessary to combine the angle constraint with other constraints, as in the proposed thermal constraint.

Effect of the thermal constraint parameters

This subsection presents optimization examples in which a thermal constraint is added to the overhang angle constraint to suppress the downward convex shapes. Each parameter related to Eq. 4.10 is set as follows. The thermal conductivity of the heat-conductive material is 119 W/mK. The applied heat flux q is set to 10 W, and the base plate temperature is set to $T_{amb} = 0°C$. Here, we examine the effects of the parameters related to the thermal constraint γ and the number of layers m in the fixed design domain. Fig. 4.9 shows the

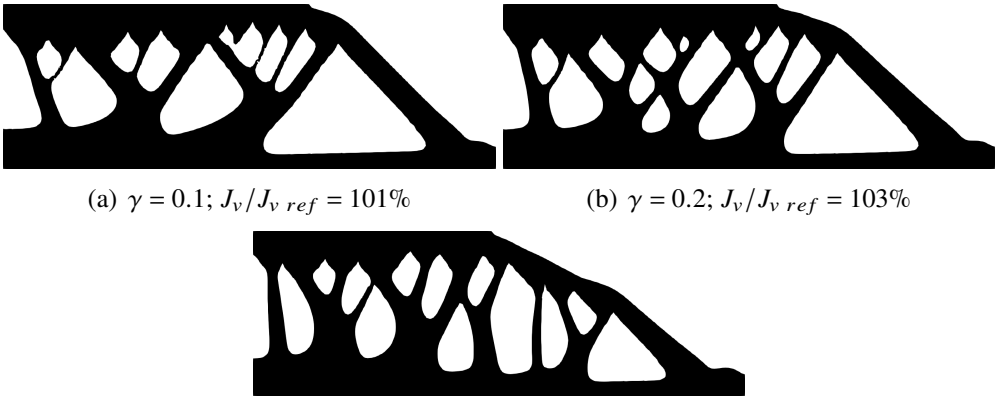

(a) $\gamma = 0.1$; $J_v/J_{v\ ref} = 101\%$ (b) $\gamma = 0.2$; $J_v/J_{v\ ref} = 103\%$

(c) $\gamma = 0.4$; $J_v/J_{v\ ref} = 112\%$

Fig. 4.9 Optimized MBB beams under different thermal constraint parameters γ.

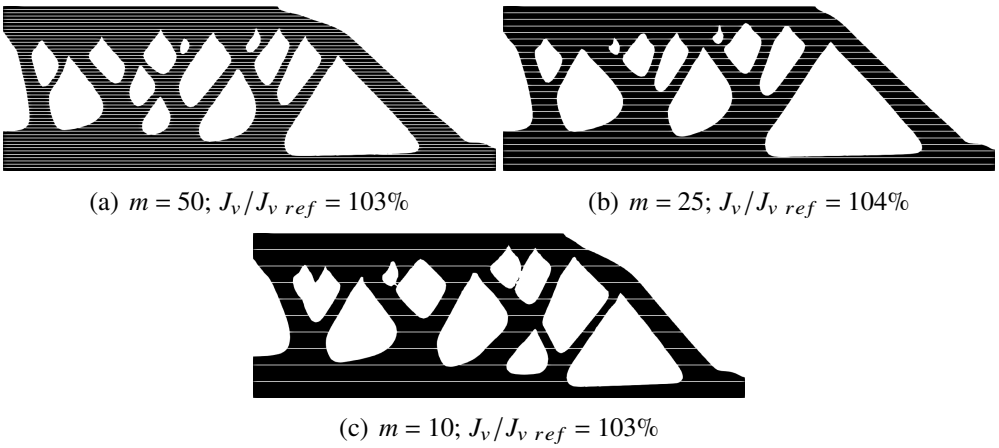

(a) $m = 50$; $J_v/J_{v\ ref} = 103\%$ (b) $m = 25$; $J_v/J_{v\ ref} = 104\%$

(c) $m = 10$; $J_v/J_{v\ ref} = 103\%$

Fig. 4.10 Optimized MBB beams under the different layer number m.

optimization results obtained under different thermal constraints γ, where the fixed design domain is divided into $m = 50$ layers. It can be observed that, by setting γ larger than

0.2, the downward convex shapes is completely suppressed. Furthermore, as γ increases, each member becomes thicker, which is expected to improve heat dissipation. However, setting γ between 0.2 and 0.4 is appropriate, as increasing γ beyond 0.4 deteriorates the compliance J_v by more than 10%. Fig. 4.10 shows the optimization results obtained under different numbers of layers m, where γ is set to 0.2. The white lines in the figure indicate layer boundaries. The downward convex shapes is no longer suppressed when the number of layers is less than $m = 10$. This result reveals that, if the number of layers is set to a size that can divide the downward convex shape, it can be suppressed by considering thermal constraints. In the optimization following examples, $\gamma = 0.2$.

Effect of building direction

Here, optimization examples for different building directions are presented to demonstrate the effectiveness of the proposed self-support constraint. As shown in Fig. 4.11, the building

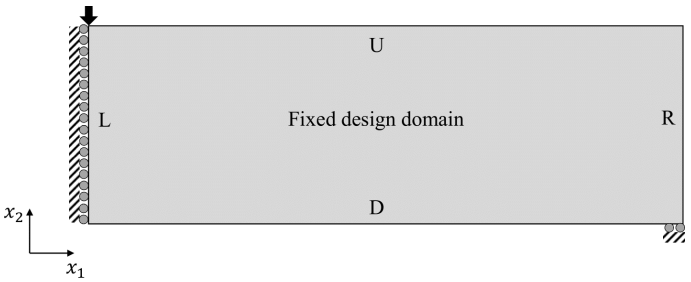

Fig. 4.11 Problem setting for the building direction of the MBB beam.

direction considers four cases in which each side U, D, L, and R of the fixed design domain is regarded as the base plate. The number of layers in the fixed design domain is set to 25 for U and D and 50 layers for L and R. Fig. 4.12 shows the optimization results obtained under different building directions. All optimal shapes suppress the downward convex shapes and satisfy the overhang angle constraint for any building direction. In particular, the shape of L achieves a compliance equivalent to that of an unconstrained shape. Thus, selecting an appropriate building direction will result in a printable design without compromising structural performance.

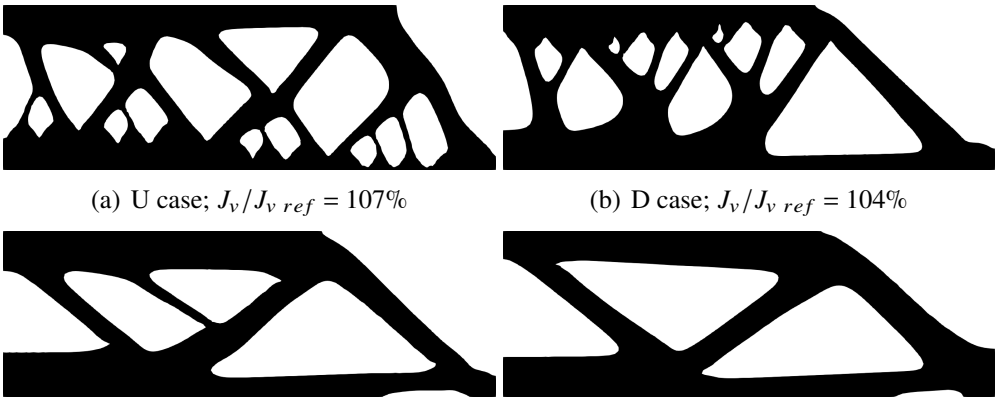

(a) U case; $J_v/J_{v\,ref}$ = 107%　(b) D case; $J_v/J_{v\,ref}$ = 104%

(c) L case; $J_v/J_{v\,ref}$ = 101%　(d) R case; $J_v/J_{v\,ref}$ = 103%

Fig. 4.12 Optimized MBB beams under different building directions.

Effect of the overhang angle

This subsection presents optimization examples for different threshold angles to further demonstrate the effectiveness of the proposed method. Therefore, the cases of threshold angles θ_0 = 30°, 45°, and 60° are considered here. Examples include the 2D MBB and cantilever beam shown in Fig. 4.13. Each parameter is set to the same value as that of the MBB beam. Figs. 4.14 and 4.15 show the optimization results obtained under different

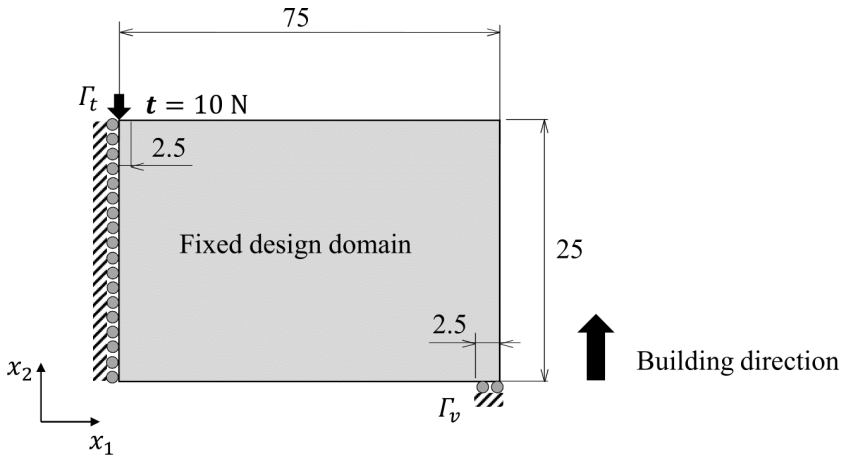

Fig. 4.13 Problem setting for the cantilever beam, with dimensions in mm.

threshold angles. In the MBB example, shapes are obtained in which no member below the specified threshold angle is created. However, in the cantilever example, some members violate the constraint in Fig. 4.15 (d). This is because the constraint function is treated

(a) $\theta_0 = 30°$; $J_v/J_{v\,ref} = 101\%$ (b) $\theta_0 = 60°$; $J_v/J_{v\,ref} = 106\%$

Fig. 4.14 Optimized MBB beams under different threshold angles.

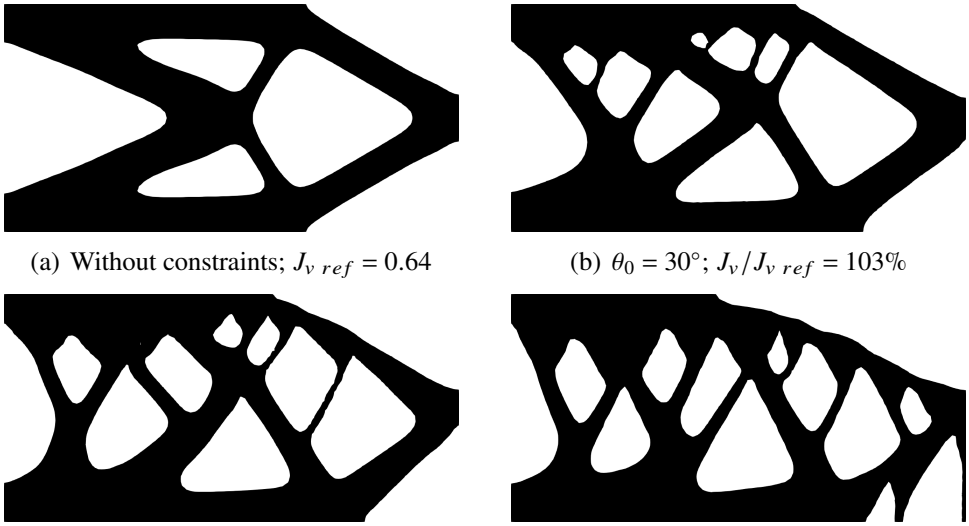

(a) Without constraints; $J_{v\,ref} = 0.64$ (b) $\theta_0 = 30°$; $J_v/J_{v\,ref} = 103\%$

(c) $\theta_0 = 45°$; $J_v/J_{v\,ref} = 108\%$ (d) $\theta_0 = 60°$; $J_v/J_{v\,ref} = 114\%$

Fig. 4.15 Optimized cantilever beams under different threshold angles.

as a penalty term, which implies that increasing the threshold angle with the same penalty parameters may not fully satisfy the constraint. Therefore, the penalty parameters should be modified. Furthermore, no significant deterioration in compliance is observed even when the threshold angle is $\theta_0 = 60°$. These results demonstrate the effectiveness of the proposed methodology for self-support constraints.

4.6.2 Combination with the distortion constraint

This subsection presents 3D optimization examples that combine a self-support constraint with a distortion constraint.

3D cantilever beam

First, we consider the minimum mean compliance problem for a 3D cantilever beam. The

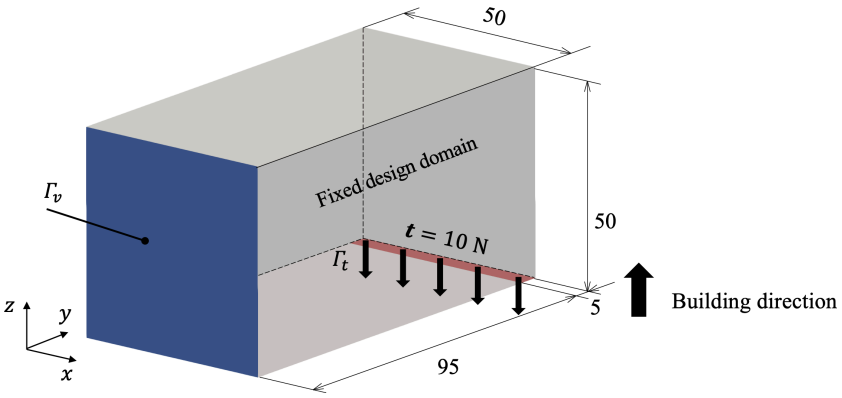

Fig. 4.16 Problem setting for the 3D cantilever beam, with dimensions in mm. The blue surface indicates the fully cramped condition, the red surface indicates the applied traction, and the building direction is the positive z-axis.

fixed design domain and boundary conditions are shown in Fig. 4.16 The upper limit of the allowable volume is set to 20% of the fixed design domain. The representative length in Eq. 4.1 is set to $L = 50$ mm. The threshold overhang angle is set to $\theta_0 = 45°$. The fixed design domain is divided in the building direction into $m = 25$ layers for the thermal constraint and $n = 50$ layers for the distortion constraint. The weighting parameter, which is related to the distortion constraint in Eq. 4.23, is set to $\alpha = 0.05$. The other parameters are those set in previous optimization examples. Figs. 4.17, 4.18 and 4.19 present the

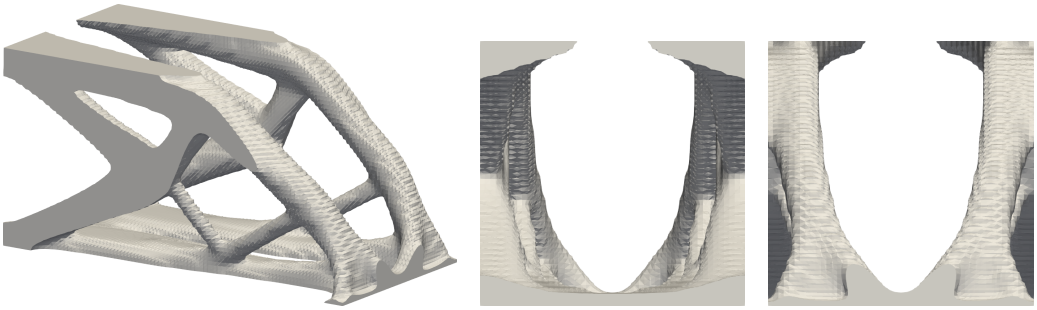

(a) Bird's-eye view (b) Rear view (c) Front view

Fig. 4.17 Optimized 3D cantilever beam without constraints; $J_{v\ ref} = 0.031$.

obtained optimization results without a constraint, with the self-support constraint, and with

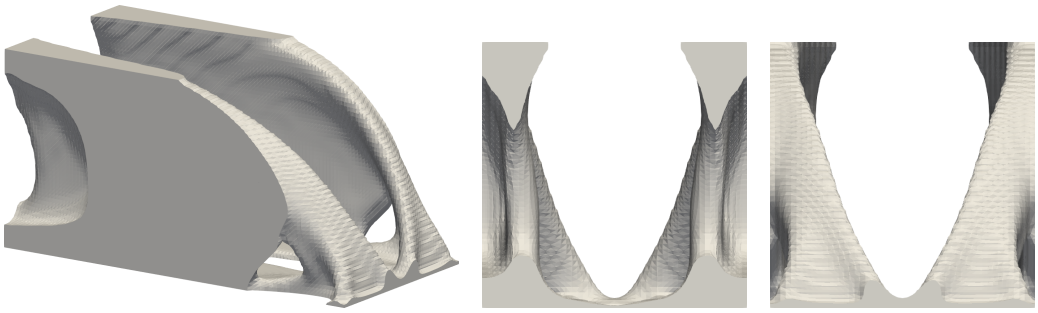

(a) Bird's-eye view (b) Rear view (c) Front view

Fig. 4.18 Optimized 3D cantilever beam with the self-support constraint; $J_v/J_{v\ ref} = 110\%$.

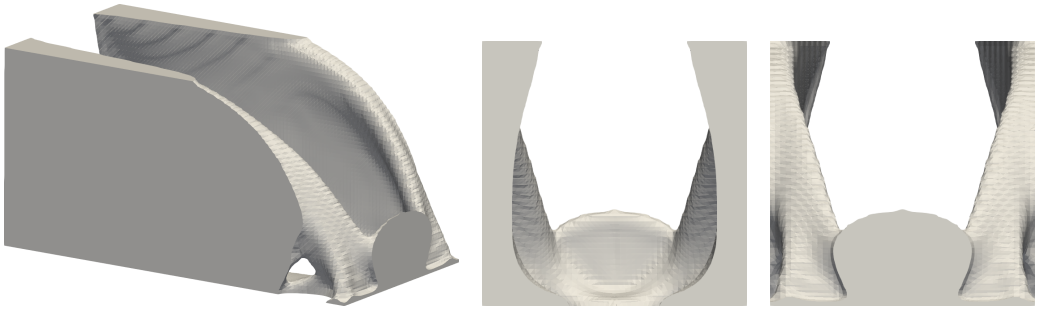

(a) Bird's-eye view (b) Rear view (c) Front view

Fig. 4.19 Optimized 3D cantilever beam with the self-support and distortion constraints; $J_v/J_{v\ ref} = 114\%$.

the self-support and distortion constraint, respectively. Both constraint-imposed shapes suppress the downward convex shapes and satisfy the overhang angle constraint. Furthermore, comparing the compliance of each shape, it can be observed that the effect of the distortion constraint on the structural performance is minimal. Fig. 4.20 shows a comparison of distortion obtained with the self-developed inherent strain method and Simufact Additive (Simufact Engineering Gmbh, Hamburg, Germany). Evidently, the distortion distribution results exhibit an acceptable level of agreement. Fig. 4.21 shows a comparison of the peak temperature for each layer obtained with the proposed thermal model and transient thermal analysis (Simufact Additive). Note that the temperature field in Fig. 4.21 (a) is obtained from the nondimensionalized version of Eq. 4.10. The appearance of overheating in the same region indicates that the proposed thermal model detects overheating. The proposed thermal model is computationally less expensive than a transient thermal analysis; however, if more layers are accumulated, the temperature gradient in the building direction reduces,

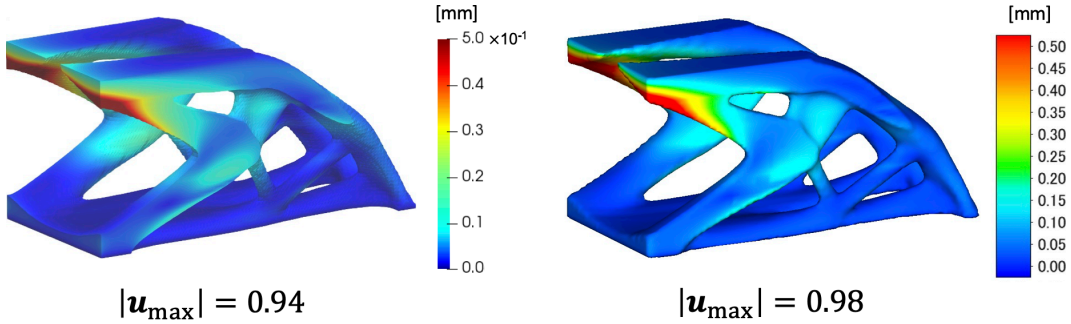

$|\boldsymbol{u}_{\max}| = 0.94$ $|\boldsymbol{u}_{\max}| = 0.98$

(a) Self-developed solver (b) Simufact Additive

Fig. 4.20 Comparison of distortion obtained from the self-developed solver and Simufact Additive.

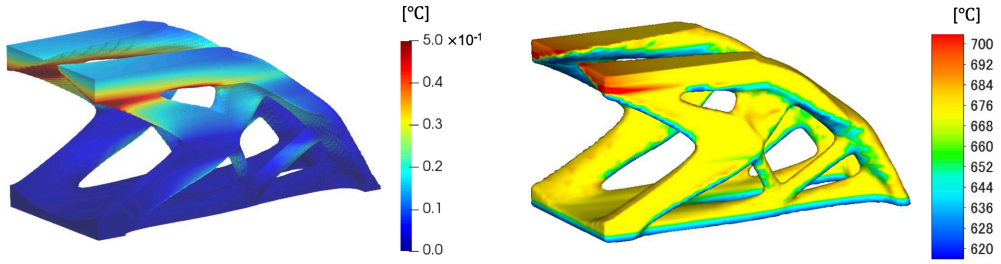

(a) Proposed thermal model (b) Transcient thermal analysis (Simufact Additive)

Fig. 4.21 Comparison of peak temperature from the proposed thermal model and transient thermal analysis (Simufact Additive).

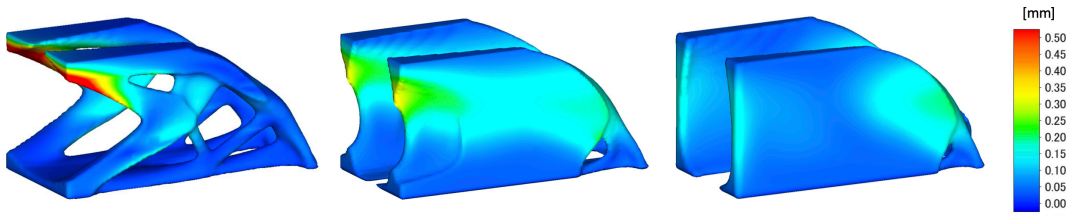

$|\boldsymbol{u}_{\max}| = 0.98$ $|\boldsymbol{u}_{\max}| = 0.36$ $|\boldsymbol{u}_{\max}| = 0.21$

(a) Without constraint (b) Self-support constraint (c) Self-support and distortion constraints

Fig. 4.22 Comparison of distortion induced by the building process for the optimized 3D cantilever beam.

and overheating may not be evaluated accurately. Therefore, validation through comparison with optimization results obtained from transient thermal analysis remains a topic for future research. The following discussion is based on the numerical results obtained from

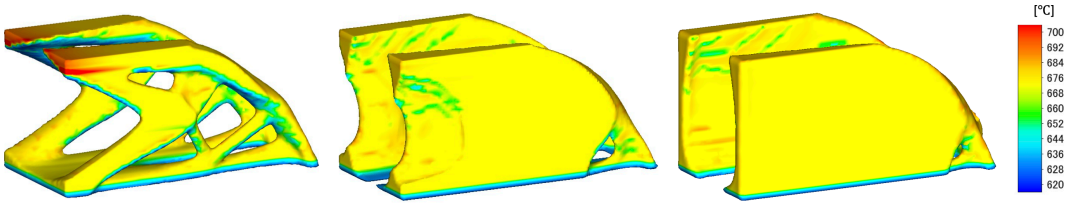

(a) Without constraint (b) Self-support constraint (c) Self-support and distortion constraints

Fig. 4.23 Comparison of the peak temperature for the optimized 3D cantilever beam.

Simufact Additive. Figs. 4.22 and 4.23 show a comparison of distortion and peak temperature for each optimal shape. The optimal shape without a constraint has a large distortion and overheating in the overhanging region. In contrast, the proposed self-support constraint not only suppresses the creation of members below the threshold angle, but also reduces the distortion and overheating. The reduction of distortion and overheating are associated with reduced overhanging regions and improved heat dissipation. In addition, by adding the distortion constraint, the maximum value of distortion $|\boldsymbol{u}_{\max}|$ decreases, and the distortion distribution becomes uniform. However, the constraints including the building process increase the computational cost because they must be calculated for each layers. Therefore, in actual design, the process of adding distortion constraints as needed is more realistic than considering all constraints.

3D heat conduction model

Next, we consider the thermal diffusivity problem for the 3D heat conduction model. The

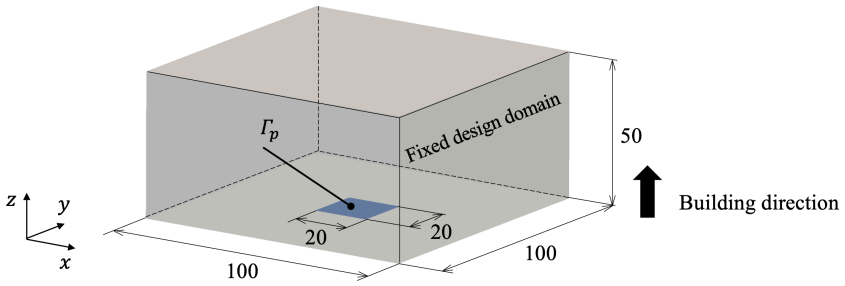

Fig. 4.24 Problem setting for the 3D heat conduction model with the dimensions in mm. The blue surface is the heat sink, and the building direction is the positive z-axis.

fixed design domain and boundary conditions are shown in Fig. 4.24 The applied heat source Q is set to 10 W, and the temperature is set to $p_{amb} = 0°C$ in Eqs. 4.35 and 4.36.

The upper limit of the allowable volume is set to 15% of the fixed design domain. The representative length in Eq. 4.1 is set to L =50 mm. The threshold overhang angle is set to $\theta_0 = 45°$. The fixed design domain is divided in the building direction into $m = 25$ layers for the thermal constraint and $n = 50$ layers for the distortion constraint. Figs. 4.25, 4.26, and

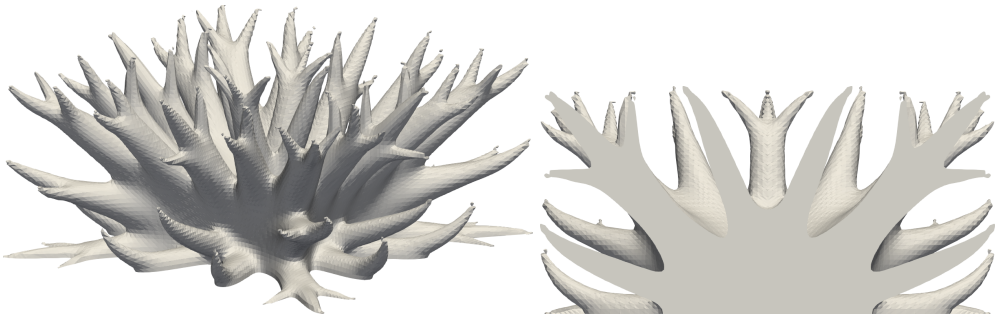

(a) Bird's-eye view (b) Cross-sectional view

Fig. 4.25 Optimized 3D heat conduction without constraints; $J_{p\ ref} = 170495$

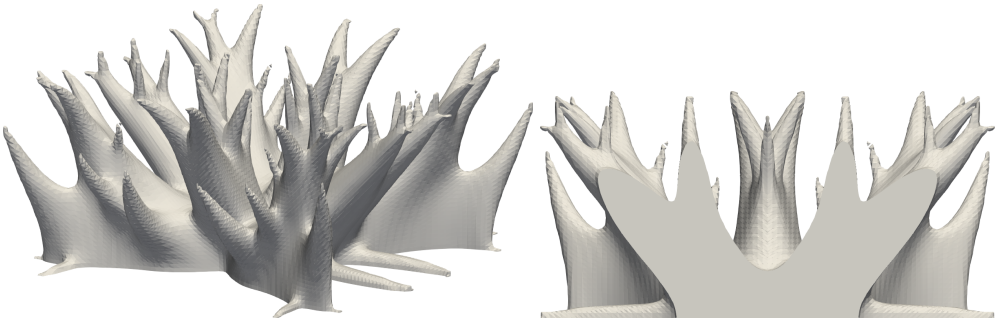

(a) Bird's-eye view (b) Cross-sectional view

Fig. 4.26 Optimized 3D heat conduction with the self-support constraint; $J_p/J_{p\ ref} = 109\%$.

4.27 present the obtained optimization results without a constraint, with the self-support constraint, and with the self-support and distortion constraint, respectively. The effect of each constraint on the thermal compliance is similar to that of the cantilever beam results. Figs. 4.28 and 4.29 show the numerical results of the distortion and overheating for the optimal shape. Similar to the cantilever beam, the self-support constraint-imposed shape has no members that violate the overhang angle constraint, reducing distortion and overheating. This is also true for the distortion constraint. In the 3D numerical examples, each parameter of the self-support constraint determined through 2D verification is set. Therefore, each parameter is independent of the problem setting. These examples demonstrate

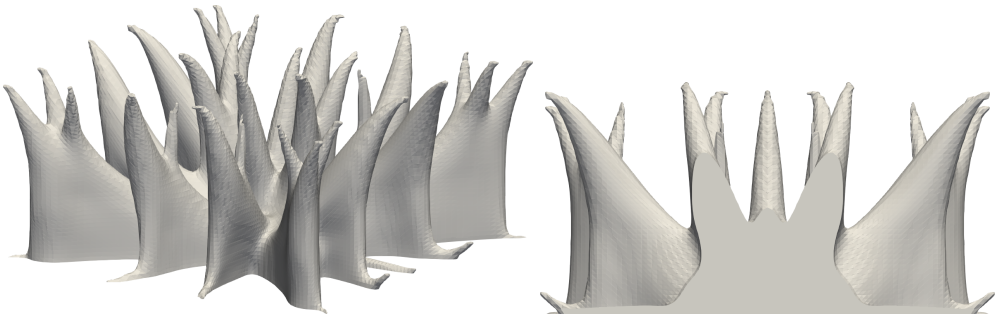

(a) Bird's-eye view (b) Cross-sectional view

Fig. 4.27 Optimized 3D heat conduction with the self-support and distortion constraints $J_p/J_{p\,ref} = 112\%$.

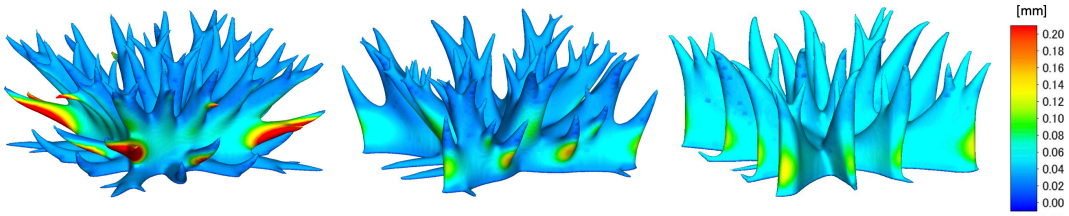

(a) Without constraint (b) Self-support constraint (c) Self-support and distortion constraints

Fig. 4.28 Comparison of the distortion induced by the building process for the optimized 3D heat conduction model.

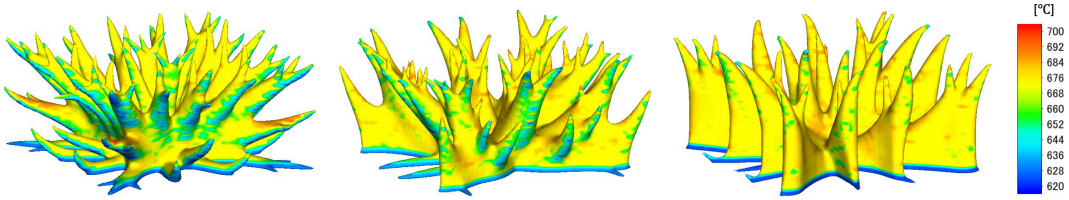

(a) Without constraint (b) Self-support constraint (c) Self-support and distortion constraints

Fig. 4.29 Comparison of peak temperature for the optimized 3D heat conduction model.

that the proposed method produces self-supporting shapes that can be manufactured with high precision using AM. This not only reduces the manufacturing time and costs but also prevents manufacturing failures due to the distortion. This means that no design changes are required for manufacturability, potentially reducing the product development time and costs.

4.7 Summary

In this chapter, we propose a self-support topology optimization method that considers distortion in the LPBF process. We achieved the following:

1. A Helmholtz-type PDE with adjustable degree of downward convex shapes are proposed, and an overhang angle constraint is formulated using angle vectors and validated through numerical examples. Two-dimensional optimization examples show that solely adjusting the penalty parameter β and the diffusion coefficient a cannot yield the self-support shape.

2. A thermal model of the building process is proposed and a thermal constraint that maximizes heat dissipation in each layer is formulated. Two-dimensional optimization examples show that the proposed thermal constraint suppresses the downward convex shapes. The effect of the constraint parameters on the downward convex shapes and structural performance is also investigated. The ability of the proposed thermal model to evaluate overheating is demonstrated through a three-dimensional numerical example.

3. A mechanical model based on the inherent strain method in the building process is presented, and a constraint to suppress the distortion is formulated.

4. An unconstrained optimization problem is formulated by including the constraint function as a penalty term in the objective function, and an optimization algorithm is constructed using FEM. The method of adjusting each penalty parameter is demonstrated through optimization examples.

5. Two-dimensional optimization examples indicate the effectiveness of the proposed self-support constraint, and the effect of design changes on structural performance is minimal.

6. Three-dimensional optimization examples demonstrate that the proposed self-support constraint yields a self-support shape with suppressed distortion and overheating. Furthermore, the addition of distortion constraint results in a more uniform distortion distribution. The proposed method enables supportless and high-precision manufacturing by AM.

Chapter 5

General conclusions

This thesis focused on topology optimization considering manufacturability in AM. The following is a summary of achievements.

In Chapter 2, a topology optimization method that considers the part distortion in AM was proposed. To predict the part-scale residual stress and distortion induced in the building process, the AM analytical model based on the inherent strain method and the identification method of the inherent strain component was proposed. Experimentally identified inherent strain components and building process algorithm in the analytical model have been demonstrated to effectively predict the part-scale residual stress and distortion, without using coupled or nonlinear analysis. The effect of the element size per layer in the analytical model on the accuracy and computational time was investigated, and the element size suitable for incorporation into topology optimization was proposed. An objective function for reducing the part distortion in AM was proposed, then a minimum mean compliance problem considering the part distortion was formulated. In the numerical implementation, an optimization algorithm was constructed and the non-dimensional sensitivity was used to enable simple adjustment of the weighting coefficient α. In the minimum mean compliance problem, the proposed method provided optimal configurations in which the compliance and part distortion can be controlled by adjusting α appropriately.

In Chapter 3, a support structure optimization that maximizes the heat dissipation in AM was proposed. An algorithm that simulates the building process was constructed based on the transient heat conduction problem with volume heat flux. In the numerical example, the difference in heat dissipation in the laser irradiated domain appeared during the cooling process, indicating that the overhang region has poor heat dissipation. An objective function for the support structure that maximizes heat dissipation of the part was proposed, then

the optimization problem was formulated. 2D and 3D design examples were provided. In all optimal configurations, support structures were added in overhang region with poor heat dissipation. Comparison with conventional support structures of the same volume demonstrates the effectiveness of the optimal configurations in heat dissipating.

In Chapter 4, a self-support topology optimization method that considers distortion in AM was proposed. A Helmholtz-type PDE with adjustable degree of downward convex shapes was proposed, and an overhang angle constraint was formulated using angle vectors and validated through numerical examples. 2D optimization examples show that solely adjusting the penalty parameter β and the diffusion coefficient a cannot yield the self-support shape. A thermal model of the building process was proposed and a thermal constraint that maximizes heat dissipation in each layer is formulated. 2D optimization examples demonstrated that the proposed thermal constraint suppresses the downward convex shapes. The effect of the constraint parameters on the downward convex shapes and structural performance was also investigated. The ability of the proposed thermal model to evaluate overheating was demonstrated through a 3D numerical example. A mechanical model based on the inherent strain method in the building process was presented, and a constraint to suppress the distortion was formulated. An unconstrained optimization problem was formulated by including the constraint function as a penalty term in the objective function, and an optimization algorithm was constructed using FEM. The method of adjusting each penalty parameter was demonstrated through optimization examples. 2D optimization examples indicated the effectiveness of the proposed self-support constraint, and the effect of design changes on structural performance is minimal. 3D optimization examples demonstrated that the proposed self-support constraint yields a self-support shape with suppressed distortion and overheating. Furthermore, the addition of distortion constraint results in a more uniform distortion distribution. The proposed method enables supportless and high-precision manufacturing by AM.

Concluding, to address the physical and geometrical challenges that arise in the metal AM building process, this thesis developed a topology optimization method that considers AM manufacturability. The techniques introduced in each chapter can be combined as needed to prevent manufacturing failures. This is expected to reduce costs and shorten the time required for product development. I hope that this thesis will be useful to accelerate the industrial use of AM and contribute to high value-added manufacturing.

References

[1] EOS GmbH, Material Data Sheet: EOS Aluminium AlSi10Mg for EOSINT M 280–290. https://fathommfg.com/wp-content/uploads/2020/11/EOS_Aluminium_AlSi10Mg_en.pdf. (Accessed on 03/30/2021).

[2] Allaire, G. (2002). *Shape optimization by the homogenization method*, volume 146. Springer-Verlag.

[3] Allaire, G. and Bogosel, B. (2018). Optimizing supports for additive manufacturing. *Structural and Multidisciplinary Optimization*, 58(6):2493–2515.

[4] Allaire, G., Dapogny, C., Estevez, R., Faure, A., and Michailidis, G. (2017). Structural optimization under overhang constraints imposed by additive manufacturing technologies. *Journal of Computational Physics*, 351:295–328.

[5] Allaire, G. and Jakabčin, L. (2018). Taking into account thermal residual stresses in topology optimization of structures built by additive manufacturing. *Mathematical Models and Methods in Applied Sciences*, 28(12):2313–2366.

[6] Allaire, G., Jouve, F., and Toader, A.-M. (2004). Structural optimization using sensitivity analysis and a level-set method. *Journal of Computational Physics*, 194(1):363–393.

[7] Amstutz, S. and Andrä, H. (2006). A new algorithm for topology optimization using a level-set method. *Journal of Computational Physics*, 216(2):573–588.

[8] Atzeni, E. and Salmi, A. (2015). Study on unsupported overhangs of alsi10mg parts processed by direct metal laser sintering (dmls). *Journal of Manufacturing Processes*, 20:500–506. Additive Manufacturing.

[9] Bayat, M., Klingaa, C. G., Mohanty, S., De Baere, D., Thorborg, J., Tiedje, N. S., and Hattel, J. H. (2020). Part-scale thermo-mechanical modelling of distortions in laser powder bed fusion–analysis of the sequential flash heating method with experimental validation. *Additive Manufacturing*, 36:101508.

[10] Bendsøe, M. P. (1989). Optimal shape design as a material distribution problem. *Structural Optimization*, 1(4):193–202.

[11] Bendsoe, M. P. and Kikuchi, N. (1988). Generating optimal topologies in structural design using a homogenization method. *Computer Methods in Applied Mechanics and Engineering*, 71(2):197–224.

[12] Bendsøe, M. P. and Sigmund, O. (1999). Material interpolation schemes in topology optimization. *Archive of applied mechanics*, 69(9):635–654.

[13] Bugatti, M. and Semeraro, Q. (2018). Limitations of the inherent strain method in simulating powder bed fusion processes. *Additive Manufacturing*, 23:329–346.

[14] Carpio, A. and Rapún, M. (2008). Solving inhomogeneous inverse problems by topological derivative methods. *Inverse Problems*, 24(4):045014.

[15] Chen, Q., Liang, X., Hayduke, D., Liu, J., Cheng, L., Oskin, J., Whitmore, R., and To, A. C. (2019). An inherent strain based multiscale modeling framework for simulating part-scale residual deformation for direct metal laser sintering. *Additive Manufacturing*, 28:406–418.

[16] Cheng, B. and Chou, K. (2015). Deformation evaluation of part overhang configurations in electron beam additive manufacturing. In *International Manufacturing Science and Engineering Conference*, volume 56826, page V001T02A072. American Society of Mechanical Engineers.

[17] Chiumenti, M., Neiva, E., Salsi, E., Cervera, M., Badia, S., Moya, J., Chen, Z., Lee, C., and Davies, C. (2017). Numerical modelling and experimental validation in selective laser melting. *Additive Manufacturing*, 18:171–185.

[18] Denlinger, E. R., Gouge, M., Irwin, J., and Michaleris, P. (2017). Thermomechanical model development and in situ experimental validation of the laser powder-bed fusion process. *Additive Manufacturing*, 16:73–80.

[19] Emmelmann, C., Sander, P., Kranz, J., and Wycisk, E. (2011). Laser additive manufacturing and bionics: redefining lightweight design. *Physics Procedia*, 12:364–368.

[20] Feijoo, R., Novotny, A., Taroco, E., and Padra, C. (2005). The topological-shape sensitivity method in two-dimensional linear elasticity topology design. *Applications of Computational Mechanics in Structures and Fluids*.

[21] Fergani, O., Berto, F., Welo, T., and Liang, S. (2017). Analytical modelling of residual stress in additive manufacturing. *Fatigue & Fracture of Engineering Materials & Structures*, 40(6):971–978.

[22] Foteinopoulos, P., Papacharalampopoulos, A., and Stavropoulos, P. (2018). On thermal modeling of additive manufacturing processes. *CIRP Journal of Manufacturing Science and Technology*, 20:66–83.

[23] Fox, J. C., Moylan, S. P., and Lane, B. M. (2016). Effect of process parameters on the surface roughness of overhanging structures in laser powder bed fusion additive manufacturing. *Procedia CIRP*, 45:131–134. 3rd CIRP Conference on Surface Integrity.

[24] Ganeriwala, R., Strantza, M., King, W., Clausen, B., Phan, T. Q., Levine, L. E., Brown, D. W., and Hodge, N. (2019). Evaluation of a thermomechanical model for prediction of residual stress during laser powder bed fusion of ti-6al-4v. *Additive Manufacturing*, 27:489–502.

[25] Garaigordobil, A., Ansola, R., Santamaría, J., and Fernández de Bustos, I. (2018). A new overhang constraint for topology optimization of self-supporting structures in additive manufacturing. *Structural and Multidisciplinary Optimization*, 58(5):2003–2017.

[26] Garreau, S., Guillaume, P., and Masmoudi, M. (2001). The topological asymptotic for pde systems: the elasticity case. *SIAM Journal on Control and Optimization*, 39(6):1756–1778.

[27] Gaynor, A. T. and Guest, J. K. (2016). Topology optimization considering overhang constraints: Eliminating sacrificial support material in additive manufacturing through design. *Structural and Multidisciplinary Optimization*, 54(5):1157–1172.

[28] Gersborg-Hansen, A., Bendsøe, M. P., and Sigmund, O. (2006). Topology optimization of heat conduction problems using the finite volume method. *Structural and multidisciplinary optimization*, 31(4):251–259.

[29] Gibson, I., Rosen, D., Stucker, B., and Khorasani, M. (2014). *Additive manufacturing technologies*, volume 17. Springer.

[30] Giusti, S., Novotny, A., and Sokołowski, J. (2010). Topological derivative for steady-state orthotropic heat diffusion problem. *Structural and Multidisciplinary Optimization*, 40(1):53–64.

[31] Giusti, S. M., Mróz, Z., Novotny, A., and Sokołowski, J. (2017). Topology design of thermomechanical actuators. *Structural and Multidisciplinary Optimization*, 55(5):1575–1587.

[32] Gouge, M., Denlinger, E., Irwin, J., Li, C., and Michaleris, P. (2019). Experimental validation of thermo-mechanical part-scale modeling for laser powder bed fusion processes. *Additive Manufacturing*, 29:100771.

[33] Hodge, N., Ferencz, R., and Solberg, J. (2014). Implementation of a thermomechanical model for the simulation of selective laser melting. *Computational Mechanics*, 54(1):33–51.

[34] Hodge, N., Ferencz, R., and Vignes, R. (2016). Experimental comparison of residual stresses for a thermomechanical model for the simulation of selective laser melting. *Additive Manufacturing*, 12:159–168.

[35] Keller, N. and Ploshikhin, V. (2014). New method for fast predictions of residual stress and distortion of am parts. In *Solid Freeform Fabrication Symposium*, volume 25.

[36] Kruth, J.-P., Froyen, L., Van Vaerenbergh, J., Mercelis, P., Rombouts, M., and Lauwers, B. (2004). Selective laser melting of iron-based powder. *Journal of Materials Processing Technology*, 149(1-3):616–622.

[37] Langelaar, M. (2016). Topology optimization of 3d self-supporting structures for additive manufacturing. *Additive Manufacturing*, 12:60–70.

[38] Langelaar, M. (2017). An additive manufacturing filter for topology optimization of print-ready designs. *Structural and multidisciplinary optimization*, 55(3):871–883.

[39] Li, C., Fu, C., Guo, Y., and Fang, F. (2016). A multiscale modeling approach for fast prediction of part distortion in selective laser melting. *Journal of Materials Processing Technology*, 229:703–712.

[40] Li, C., Guo, Y., Fang, X., and Fang, F. (2018a). A scalable predictive model and validation for residual stress and distortion in selective laser melting. *CIRP Annals*, 67(1):249–252.

[41] Li, C., Liu, J., Fang, X., and Guo, Y. (2017). Efficient predictive model of part distortion and residual stress in selective laser melting. *Additive Manufacturing*, 17:157–168.

[42] Li, C., Liu, Z., Fang, X., and Guo, Y. (2018b). Residual stress in metal additive manufacturing. *Procedia Cirp*, 71:348–353.

[43] Liang, X., Chen, Q., Cheng, L., Hayduke, D., and To, A. C. (2019). Modified inherent strain method for efficient prediction of residual deformation in direct metal laser sintered components. *Computational Mechanics*, 64(6):1719–1733.

[44] Mercelis, P. and Kruth, J.-P. (2006). Residual stresses in selective laser sintering and selective laser melting. *Rapid Prototyping Journal*.

[45] Miki, T. and Yamada, T. (2021). Topology optimization considering the distortion in additive manufacturing. *Finite Elements in Analysis and Design*, 193:103558.

[46] Mukherjee, T., Zhang, W., and DebRoy, T. (2017). An improved prediction of residual stresses and distortion in additive manufacturing. *Computational Materials Science*, 126:360–372.

[47] Murakawa, H., Luo, Y., and Ueda, Y. (1996). Prediction of welding deformation and residual stress by elastic fem based on inherent strain. *Journal of the society of Naval Architects of Japan*, 1996(180):739–751.

[48] Novotny, A. A., Feijóo, R. A., Taroco, E., and Padra, C. (2003). Topological sensitivity analysis. *Computer methods in applied mechanics and engineering*, 192(7-8):803–829.

[49] Papadakis, L., Loizou, A., Risse, J., Bremen, S., and Schrage, J. (2014a). A computational reduction model for appraising structural effects in selective laser melting manufacturing: a methodical model reduction proposed for time-efficient finite element analysis of larger components in selective laser melting. *Virtual and Physical Prototyping*, 9(1):17–25.

[50] Papadakis, L., Loizou, A., Risse, J., and Schrage, J. (2014b). Numerical computation of component shape distortion manufactured by selective laser melting. *Procedia Cirp*, 18:90–95.

[51] Peng, H., Ghasri-Khouzani, M., Gong, S., Attardo, R., Ostiguy, P., Rogge, R. B., Gatrell, B. A., Budzinski, J., Tomonto, C., Neidig, J., et al. (2018). Fast prediction of thermal distortion in metal powder bed fusion additive manufacturing: Part 2, a quasi-static thermo-mechanical model. *Additive Manufacturing*, 22:869–882.

[52] Peng, H., Go, D. B., Billo, R., Gong, S., Shankar, M. R., Gatrell, B. A., Budzinski, J., Ostiguy, P., Attardo, R., Tomonto, C., et al. (2016). Part-scale model for fast prediction of thermal distortion in dmls additive manufacturing; part 2: a quasi-static thermomechanical model. In *Proc. 27th Annu. Int. Solid Free. Fabr. Symp*, pages 361–381.

[53] Prabhakar, P., Sames, W. J., Dehoff, R., and Babu, S. S. (2015). Computational modeling of residual stress formation during the electron beam melting process for inconel 718. *Additive Manufacturing*, 7:83–91.

[54] Prabhune, B. C. and Suresh, K. (2020). A fast matrix-free elasto-plastic solver for predicting residual stresses in additive manufacturing. *Computer-Aided Design*, page 102829.

[55] Qian, X. (2017). Undercut and overhang angle control in topology optimization: a density gradient based integral approach. *International Journal for Numerical Methods in Engineering*, 111(3):247–272.

[56] Ranjan, R., Yang, Y., Ayas, C., Langelaar, M., and Van Keulen, F. (2017). Controlling local overheating in topology optimization for additive manufacturing. In *Proceedings of euspen special interest group meeting: additive manufacturing, Leuven, Belgium*.

[57] Roberts, I. A., Wang, C., Esterlein, R., Stanford, M., and Mynors, D. (2009). A three-dimensional finite element analysis of the temperature field during laser melting of metal powders in additive layer manufacturing. *International Journal of Machine Tools and Manufacture*, 49(12-13):916–923.

[58] Setien, I., Chiumenti, M., van der Veen, S., San Sebastian, M., Garciandía, F., and Echeverría, A. (2019). Empirical methodology to determine inherent strains in additive manufacturing. *Computers & Mathematics with Applications*, 78(7):2282–2295.

[59] Soylemez, E., Koç, E., and Coşkun, M. (2019). Thermo-mechanical simulations of selective laser melting for alsi10mg alloy to predict the part-scale deformations. *Progress in Additive Manufacturing*, 4(4):465–478.

[60] Thore, C.-J., Grundström, H. A., Torstenfelt, B., and Klarbring, A. (2019). Penalty regulation of overhang in topology optimization for additive manufacturing. *Structural and Multidisciplinary Optimization*, 60(1):59–67.

[61] Ueda, Y., Fukuda, K., Nakacho, K., and Endo, S. (1975). A new measuring method of residual stresses with the aid of finite element method and reliability of estimated values. *Journal of the Society of Naval Architects of Japan*, 1975(138):499–507.

[62] Ueda, Y., Fukuda, K., and Tanigawa, M. (1979). New measuring method of three dimensional residual stresses based on theory of inherent strain (welding mechanics, strength & design). *Transactions of JWRI*, 8(2):249–256.

[63] Ueda, Y. and Yamakawa, T. (1971). Analysis of thermal elastic-plastic stress and strain during welding by finite element method. *Japan Welding Society Transactions*, 2(2).

[64] Van Belle, L., Vansteenkiste, G., and Boyer, J. C. (2013). Investigation of residual stresses induced during the selective laser melting process. In *Key Engineering Materials*, volume 554, pages 1828–1834. Trans Tech Publ.

[65] van de Ven, E., Maas, R., Ayas, C., Langelaar, M., and van Keulen, F. (2018). Continuous front propagation-based overhang control for topology optimization with additive manufacturing. *Structural and Multidisciplinary Optimization*, 57(5):2075–2091.

[66] Wang, C. and Qian, X. (2020). Optimizing support for heat dissipation in additive manufacturing. In *ASME 2020 International Design Engineering Technical Conferences and Computers and Information in Engineering Conference*. American Society of Mechanical Engineers Digital Collection.

[67] Wang, Y., Gao, J., and Kang, Z. (2018). Level set-based topology optimization with overhang constraint: towards support-free additive manufacturing. *Computer Methods in Applied Mechanics and Engineering*, 339:591–614.

[68] Wildman, R. A. and Gaynor, A. T. (2017). Topology optimization for reducing additive manufacturing processing distortions. Technical report, Weapons and Materials Research Directorate, US Army Research Laboratory ⋯.

[69] Wu, A. S., Brown, D. W., Kumar, M., Gallegos, G. F., and King, W. E. (2014). An experimental investigation into additive manufacturing-induced residual stresses in 316l stainless steel. *Metallurgical and Materials Transactions A*, 45(13):6260–6270.

[70] Yamada, T., Izui, K., Nishiwaki, S., and Takezawa, A. (2010). A topology optimization method based on the level set method incorporating a fictitious interface energy. *Computer Methods in Applied Mechanics and Engineering*, 199(45-48):2876–2891.

[71] Yang, Y., Jamshidinia, M., Boulware, P., and Kelly, S. (2018). Prediction of microstructure, residual stress, and deformation in laser powder bed fusion process. *Computational Mechanics*, 61(5):599–615.

[72] Zaeh, M. F. and Branner, G. (2010). Investigations on residual stresses and deformations in selective laser melting. *Production Engineering*, 4(1):35–45.

[73] Zhang, W., Tong, M., and Harrison, N. M. (2019). Resolution, energy and time dependency on layer scaling in finite element modelling of laser beam powder bed fusion additive manufacturing. *Additive Manufacturing*, 28:610–620.

[74] Zhou, M., Liu, Y., and Lin, Z. (2019). Topology optimization of thermal conductive support structures for laser additive manufacturing. *Computer Methods in Applied Mechanics and Engineering*, 353:24–43.

List of Publications

International Journal Papers

[1] Takao Miki, Takayuki Yamada, Topology optimization considering the distortion in additive manufacturing, *Finite Elements in Analysis and Design*, Vol.193, 2021, p.103558.

[2] Takao Miki, Shinji Nishiwaki, Topology optimization of the support structure for heat dissipation in additive manufacturing, *Finite Elements in Analysis and Design*, Vol.203, 2022, p.103708.

[3] Takao Miki, Self-support topology optimization considering distortion for metal additive manufacturing, *Computer Methods in Applied Mechanics and Engineering*, Vol.404, 2023, p.115821.

Domestic Journal Papers (in Japanese)

[1] 三木隆生，古田歩，佐藤勇気，山田 崇恭，泉井 一浩，西脇 眞二積層造形における幾何学的制約を考慮したトポロジー最適化, 日本機械学会論文集, 85 巻, 874 号, 2019, p.18-00508.